

THE LAS CAMPANAS DISTANT CLUSTER SURVEY - THE CATALOG

ANTHONY H. GONZALEZ¹, DENNIS ZARITSKY², JULIANNE J. DALCANTON³, AND AMY NELSON⁴
Received 2000 December 31; Accepted 2001 May 25

ABSTRACT

We present an optically-selected catalog of 1073 galaxy cluster and group candidates at $0.3 \lesssim z \lesssim 1$. These candidates are drawn from the Las Campanas Distant Clusters Survey (LCDCS), a drift-scan imaging survey of a 130 square degree strip of the southern sky. To construct this catalog we utilize a novel detection process in which clusters are detected as positive surface brightness fluctuations in the background sky. This approach permits us to find clusters with significantly shallower data than other matched-filter methods that are based upon number counts of resolved galaxies. Selection criteria for the survey are fully automated so that this sample constitutes a well-defined, homogeneous sample that can be used to address issues of cluster evolution and cosmology. Estimated redshifts are derived for the entire sample, and an observed correlation between surface brightness and velocity dispersion, σ , is used to estimate the limiting velocity dispersion of the survey as a function of redshift. We find a net surface density of 15.5 candidates per square degree at $z_{est} \geq 0.3$, with a false-detection rate of $\sim 30\%$. At $z \sim 0.3$ we probe down to the level of poor groups while by $z \sim 0.8$ we detect only the most massive systems ($\sigma \gtrsim 1000 \text{ km s}^{-1}$). We also present a supplemental catalog of 112 candidates that fail one or more of the automated selection criteria, but appear from visual inspection to be *bona fide* clusters.

1. INTRODUCTION

In the quest to determine the parameters describing cosmological models and discriminate between the various models, galaxy clusters constitute a uniquely powerful class of objects. In contrast to the galaxy distribution, the cluster distribution remains closely coupled to the initial power spectrum, probing scales where the mass distribution is still governed by linear dynamics. Consequently, it is relatively simple to extract information about cosmological parameters from properties of the cluster population. Properties such as the cluster abundance and spatial correlation length are strongly dependent upon Ω_0 , but are insensitive to Ω_Λ . Cluster-based constraints therefore complement cosmic microwave background (CMB) and high-redshift supernovae constraints, which are sensitive to $\Omega_0 + \Omega_\Lambda$ and $\Omega_0 - \Omega_\Lambda$, respectively.

Unfortunately, the potential for strong, cluster-based constraints remains largely unrealized. A major limitation has been the dearth of known clusters at $z > 0.5$, because it is at these redshifts that model predictions strongly diverge (White, Efstathiou, & Frenk 1993). The two most common techniques for finding distant clusters are optical searches for projected galaxy overdensities and X-ray searches for extended thermal bremsstrahlung, but the effectiveness of both approaches is currently limited at $z > 0.5$. In the optical, detection of projected overdensities requires deep imaging. As a result, only relatively small areas have been thus surveyed, with the largest published survey of this kind being the I-band ESO Imaging Survey (EIS; Scodreggio et al. 1999), which covers 17 square degrees. Further, aggregates of cluster galaxies are dominated by faint field galaxies, and so detection of true overdensities is difficult. Detection efficiency can be improved

by including color information in the search for aggregates, but requires either a reduction in survey area or corresponding increase in telescope time. In the X-ray, the problem is not angular coverage but rather detector sensitivity. The most recent generation of orbital telescopes had insufficient sensitivity to detect all but the most luminous high-redshift clusters. Only six clusters at $z > 0.5$ were discovered in the Einstein Medium Sensitivity Survey (EMSS; Henry et al. 1992; Gioia & Luppino 1994), and the largest published X-ray sample for this redshift regime is a set of 24 clusters detected as part of a cluster survey by Vikhlinin et al. (1998) using archival ROSAT PSPC data.

With the Las Campanas Distant Cluster Survey (LCDCS) we generate a catalog that incorporates some of the most desirable elements of each of the two traditional approaches. By employing a novel technique for identifying clusters, we are able to survey an effective angular area that is a factor of five larger than traditional optical surveys, while probing to higher redshift and lower mass limits than the existing X-ray surveys. Further, we examine a sample of known clusters and utilize the properties of these systems, in conjunction with follow-up imaging of a subset of LCDCS clusters, to calibrate methods of estimating the redshift and velocity dispersion, σ , for all candidates. Estimating σ is critical, as the principal advantage of X-ray surveys over optical surveys has been that X-ray luminosity, L_X , is much more strongly correlated with mass than optical richness. The survey concept is explained in §2, details of the reduction procedure and cluster identification are described in §4-5, and the catalog is presented in §6. The properties of the sample are discussed in §7, and §8 contains a summary and discussion of the desired properties of future surveys utilizing this

¹ Harvard-Smithsonian Center for Astrophysics, 60 Garden Street, Cambridge, MA 02138

² Steward Observatory, University of Arizona, 933 North Cherry Avenue, Tucson, AZ 85721

³ Department of Astronomy, University of Washington, Box 351580, Seattle, WA 98195-1580

⁴ Department of Astronomy and Astrophysics, University of California at Santa Cruz, Santa Cruz, CA 95064

approach.

2. SURVEY CONCEPT

The basic idea driving the Las Campanas Distant Cluster Survey is that clusters can be detected as regions of excess surface brightness relative to the background sky. This hypothesis, first suggested by Davies et al. (1994) and developed in detail by Dalcanton (1996), posits that although few individual cluster galaxies may be detectable, the integrated signal from the undetected galaxies can be sufficiently large for detection of the cluster. Subsequently, consideration of the luminosity budgets of local clusters (Uson, Bough, & Kuhn 1990, 1991; Scheick & Kuhn 1994; Gonzalez et al. 2000) has led to the realization that this signal is further augmented by a significant contribution from the halo of the brightest cluster galaxy. To maximize the contrast between a cluster and the background, the image should be smoothed on a scale comparable to the core size of the cluster, thus reducing the Poisson noise. Pilot work utilizing drift-scan data from the Palomar 5m demonstrated the feasibility of this approach (Dalcanton 1995; Zaritsky et al. 1997; data described in Dalcanton et al. 1997), laying the groundwork for the LCDCS.

Our approach offers several key advantages relative to other recent optical surveys, which all rely upon identification of overdensities in the projected galaxy number density to detect clusters. Most of these surveys, such as the Palomar Distant Cluster Survey (Postman et al. 1996, PDCS;), employ a weighted filter designed to match the expected cluster luminosity function and radial profile at a given redshift.⁵ One key advantage of our approach is that we require much shallower imaging than previous optical surveys because our detection technique does not require that we resolve individual cluster galaxies. For the LCDCS, we are able to detect clusters out to $z \sim 1$ with an effective exposure time of 194s on a 1m telescope. This approach permits a large area to be surveyed, which is necessary for detection of the richest, rarest systems. A second advantage is that, because this method is sensitive only to dense cluster cores, cluster detections have a small cross-section ($\sim 20''$, or $\sim 100 h^{-1}$ kpc at $z=1$). Consequently, detections due to superposition of poor systems or the presence of wall-like structures are rare. Further, this method is less dependent upon the cluster luminosity function than surveys that depend upon number counts (e.g. a cluster can be detected via the BCG halo in the absence of other bright cluster galaxies) and makes no assumption about galaxy colors or the presence of a well-defined red sequence. As a result, comparison of this type of survey with more traditional optical catalogs should be quite productive for better defining the selection biases of both methods. The key disadvantage of this approach is that a variety of astrophysical phenomena are capable of inducing surface brightness excesses (most notably galactic cirrus, low surface brightness galaxies and tidal tails), and techniques must be developed to minimize contamination of the catalog by these sources. The methods employed for minimizing contamination in the LCDCS are discussed in §5.

⁵ Other examples of the use of matched filters with projected number counts can be found in Kawasaki et al. (1998), Olsen et al. (1999), and Kepner et al. (1999). The latter group expands upon previous work by employing an adaptive matched filter capable of incorporating photometric and spectroscopic redshift information.

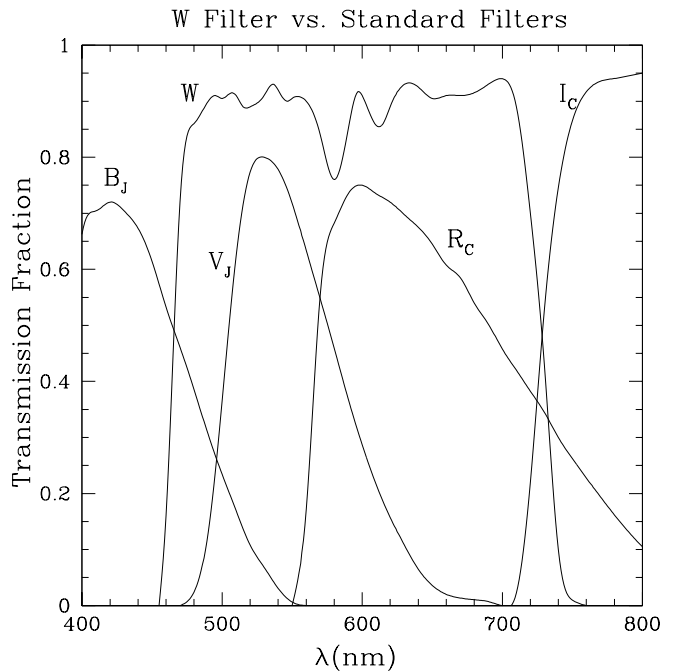


FIG. 1.— Comparison of the broad W filter utilized in this work to standard Johnson (B_V) and Cousins (R_I) filters. The red cutoff is designed to avoid night sky lines, while maximizing incident flux. The blue cutoff is designed to avoid large atmospheric refraction.

3. THE DATA

The survey data were obtained in March 1995 under photometric conditions using the Las Campanas 1m telescope, the Great Circle Camera (Zaritsky, Schectman, & Bredthauer 1996), and the Tek#5 CCD. We employed a custom, wide-band filter (hereafter designated W) designed to maximize the incident flux while avoiding strong atmospheric emission lines in the red and atmospheric refraction in the blue. The wavelength coverage, which roughly extends from B to I , is shown in Figure 1. Individual drift scans are 2048×20000 pixels with a plate scale of $0''.697 \text{ pixel}^{-1}$ and an effective exposure time of 97s. The data consist of 198 contiguous, overlapping scans that collectively cover 160 square degrees of the southern sky. The geometry is such that nine scans are obtained at a given right ascension. Each of these nine scans is shifted in declination by half the width of the CCD from the previous scan. With this approach, we cover a strip extending 85° in right ascension ($10^h < \alpha < 15^h 39^m$) with a width of 1.8° in declination. For the cluster survey, we use the central 1.5° in declination ($-13^\circ < \delta < -11^\circ 30'$), for which every location is imaged twice. The net exposure time of this region is 194 seconds.

Magnitudes are calibrated using standard fields from Landolt (1992). To permit calibration of the W filter, images of the standard stars were obtained in Cousins R - and I - as well as in the W -band. We use this data to define the zeropoint of the W filter on the Vega system (i.e. $W=0$ for Vega). For reference, the galaxy density and galaxy to star ratio are plotted in Figure 2 as a function of W -band magnitude.

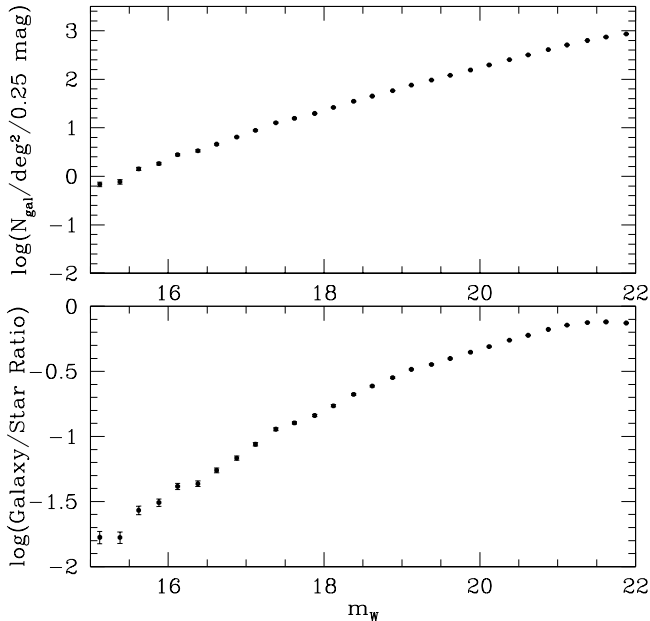


FIG. 2.— Projected galaxy density and ratio of galaxies to stars as a function of m_W .

4. REDUCTIONS

An overview of the reduction procedure employed is as follows. First, individual scans are bias-subtracted and flatfielded. Next, an image registration routine is used that calculates the image center and curvature of each scan relative to a cartesian system defined with axes (α, δ) . We then use FOCAS to detect all objects in the scans and “clean” detected objects down to a limiting aperture magnitude $m_{ap}=22.8$ mag. Bright stars and galaxies are masked at this stage and the image is binned by a factor of two. After masking, we subtract temporal sky fluctuations from the individual scans and perform a second stage of flatfielding. Next, the results of the image registration stage are used to geometrically transform the images into the cartesian coordinate system. Remaining large-scale brightness fluctuations are subtracted via boxcar smoothing, and sets of images with the same right ascension are combined into large mosaics. Finally, we convolve the mosaics with an exponential smoothing kernel with a scale length of $10''$ to enhance cluster-size surface brightness features. SExtractor is used to detect fluctuations in the smoothed mosaics and an automated classification routine is employed to determine which fluctuations are induced by clusters. An illustration of this procedure can be seen in Figure 3, and the various aspects of this procedure are described in detail below.

4.1. Bias Subtraction and Flatfielding

Bias subtraction is performed for the drift-scan data using overscan regions in both dimensions. The overscan region perpendicular to the readout direction is 30 pixels wide; the overscan region parallel to the direction of readout is 98 pixels wide for half of the scans, and 10 pixels wide for the rest. To model the bias, we average across the width of the overscan region, and then apply a symmetric Savitsky-Golay smoothing filter (60 pixels in width) along

the length of the overscan region to reduce pixel-to-pixel noise (Press et al. 1992). Rms variations in the subtracted bias are $\sim 0.1\%$. High precision in this step is important, as residual variations can induce spurious detections. Fortunately, removal of the bias is augmented by subsequent reduction stages. For example, some of the residual variation along the readout direction will be removed during sky subtraction, and in both directions residual variation is damped by $\sqrt{2}$ when the images are combined.

Accurate flatfielding of the data is also critical. The reduced data must have residual flatness variation of less than 0.2% ($\mu_W \sim 28.3$ mag arcsec $^{-2}$), or else these variations will be the dominant source of noise limiting cluster detection. A key property of drift-scan data is its intrinsic uniformity. With drift scans, pixel-to-pixel variation is minimized because data are clocked across the chip, so sensitivity variations are a concern only perpendicular to the readout direction (at a level $\sim 2\%$ in our raw data). Consequently only a one-dimensional flatfield is required, for which the Poisson noise can be reduced significantly relative to a two-dimensional flatfield by averaging along the direction of readout. To reduce the flatness variation to the desired level, we apply two stages of flatfielding. In both stages we use a set of 4 or 5 scans to construct a sigma-clipped, median averaged flatfield. (For a given right ascension, typically four of the scans are taken consecutively one night, and the other five are taken consecutively on a different night.) Each scan is 20,000 pixels in length and the typical sky level in W is ~ 100 counts, so the associated Poisson noise is 0.035% per column. The first stage of flatfielding immediately follows bias subtraction and reduces sensitivity variation from 2% to 0.4% . Subsequent to this stage, we use the IRAF routine *fixpix* to interpolate across the three bad columns in our drift scans (see Figure 4). The second flatfielding stage is designed to remove the 0.4% residual variation. To eliminate contamination from resolved objects, which may lead to correlated variations across columns, this second stage is run after all detected objects have been replaced with local sky pixels (see §4.2), and after temporal fluctuations in the sky level have been subtracted along the direction of readout (see §4.3). Figure 4 shows a typical pair of flatfields resulting from these two stages of flatfielding. Subsequent to this final flatfielding all scans are flat to $\lesssim 0.2\%$, with an rms residual variation of $\sim 0.1\%$.

4.2. Object Removal and Masking

Next, we remove all stars and galaxies that are individually detectable in the images using a modified version of the Faint Object Classification and Analysis System (FOCAS) (Jarvis & Tyson 1981; Valdes 1993; modifications described in Dalcanton et al. 1997). The basic strategy is to use FOCAS to detect all objects in the scans and then clean out objects down to a limiting aperture magnitude. Using an aperture of radius 5 pixels, we choose a limiting aperture magnitude $m_W=22.8$, which roughly corresponds to a $4\text{-}\sigma$ detection in an individual scan.

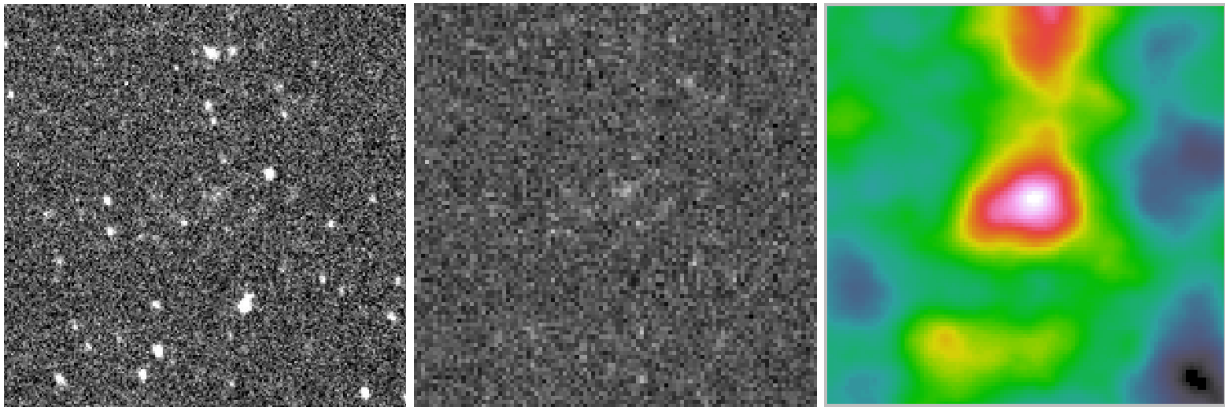


FIG. 3.— Three panel image illustrating the reduction process for a $140' \times 140'$ region, centered on a cluster with a spectroscopic redshift $z=0.80$. The left panel is the bias-subtracted, flatfielded drift-scan data. The middle panel shows an intermediate stage in the reduction process in which detected objects have been replaced with locally drawn, random sky pixels. This image is then convolved with an exponential smoothing kernel of scale length $10''$, resulting in the image shown in the panel on the right. Sextractor is utilized to detect positive fluctuations in the smoothed data.

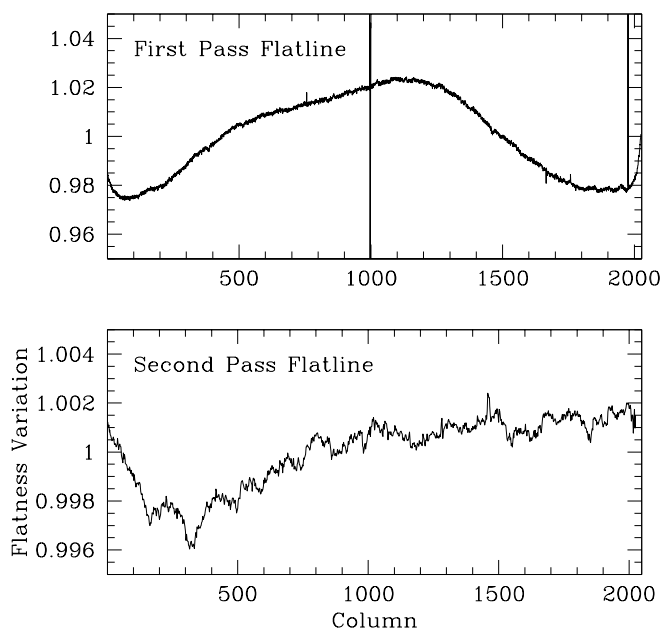


FIG. 4.— Typical flatfields generated in reducing the scans. The upper panel shows the 1-D flatline applied to the raw data, which corrects initial variations of order 2%. The sharp vertical features in this panel correspond to bad columns. The lower panel shows the second pass flatline which is applied to scans after sky subtraction and cleaning. Subsequent to this stage, residual variations are at the level of 0.1%.

One inherent obstacle in using FOCAS for detection is that drift scans have a time-variable component to the sky level. This variability in turn means that the rms of the sky will vary through the image. Because FOCAS uses a fixed sigma threshold throughout the scan, the sky variation results in variable depth for the FOCAS catalog. The solution we employ is to calculate and input to FOCAS the sigma corresponding to the lowest sky level in the scan. The catalog then goes too deep in some locations, but is deep enough everywhere to uniformly implement the desired aperture magnitude limit for cleaning, and yields uniform object removal throughout the image. The actual cleaning is accomplished with a modified version of the FOCAS routine CLEAN, which replaces object

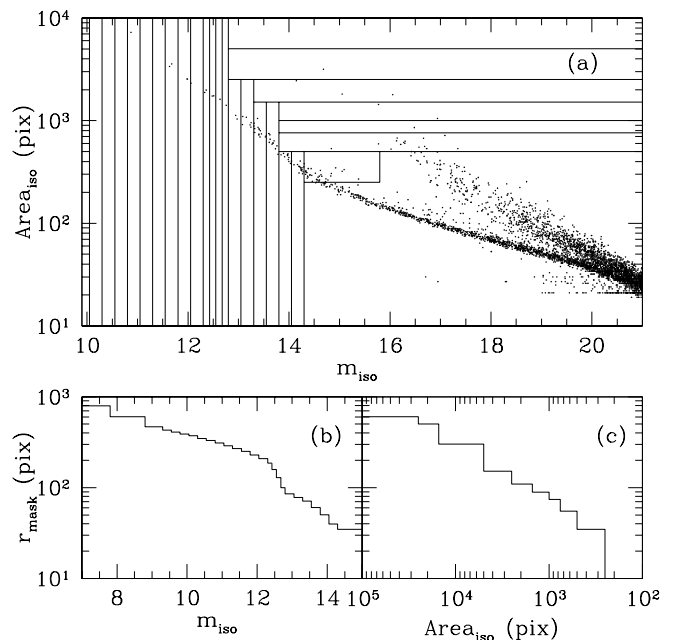


FIG. 5.— (a) Mask size as a function of FOCAS isophotal magnitude and isophotal area. Points indicate a representative subset of objects detected in the survey, with the lower branch containing stars and the upper branch containing galaxies. Solid lines demarcate changes in mask size, with no masking applied to objects in the lower right region of the plot. For stars, isophotal magnitude is the primary factor driving the mask size; for galaxies, isophotal area is the more important factor. An inflection occurs in the stellar branch at $m \sim 15$ and corresponds to the magnitude above which stars are saturated in this data set. (b) Stellar mask size as a function of isophotal magnitude. (c) Galaxy mask size as a function of isophotal area.

pixels with local sky pixels. When cleaning, the replacement region corresponds to the isophotal area of the detection, plus a growth region, the width of which is a function of the $5''$ aperture magnitude of the object. For objects with $m_{ap} < 16.8$, the width of the growth region is 8 pixels; for objects just above the cleaning threshold the width of the growth region is 2 pixels. There are two notable cases in which this cleaning proves insufficient, however. Saturated stars and large galaxies both leave residual flux in

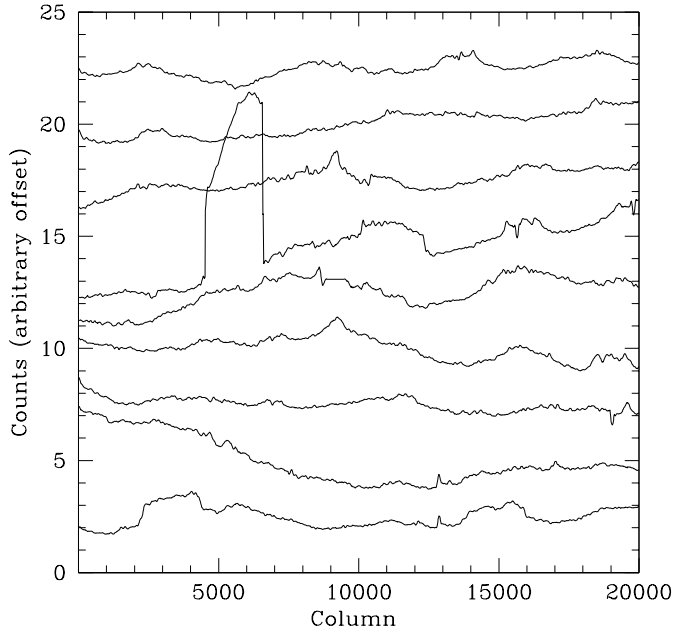


FIG. 6.— Sky fits for a set of nine scans at the same right ascension. The mean level of a given fit is arbitrary as these have been renormalized and plotted in order of decreasing declination, with a mean offset of 2.5 counts between each scan. This figure illustrates the amplitude of the sky fluctuations, and also the need for a discontinuous component to the sky level in some cases.

the image beyond the cleaning radius, and consequently are masked.

To mask, we identify the objects for which cleaning is insufficient. Figure 5a, which shows isophotal area as a function of isophotal magnitude, illustrates how we perform this identification. Objects on the upper branch in this figure are galaxies; those on the lower branch are stars. For large galaxies, we use the isophotal area to determine the size of the mask. For the saturated stars ($m_W \lesssim 15$), we instead use the isophotal magnitude. The radii of the circular masks as a function of isophotal area and magnitude are shown in Figures 5b and 5c. For both stars and galaxies we take a conservative approach and apply large masks, with the typical mask radius for galaxies being ~ 5 times the isophotal radius. In addition to bright stars and galaxies, scan edges and linear features in the data such as bleed trails are also masked. The net effect of all masking is a 28% reduction in the total area of the survey.

4.3. Sky subtraction

After the images have been masked, a large gradient in the sky level persists along the direction of readout of the scans (α). The gradient is the result of temporal variation in the sky brightness during the observations. This component of the sky is generally smoothly varying; however, sharp changes in the sky level do exist. These sharp changes can be due to bleed trails, scattered light from bright stars in the field of view, or internal reflections in the optics. Both the smooth and sharp components can result in sky brightness fluctuations of $\Delta\mu \sim 0.3$ mag arcsec $^{-1}$. In the absence of sharp edges, an effective way of removing the sky is to average the columns in a scan and then

apply Savitsky-Golay filtering. This approach minimizes random small-scale noise while preserving the slowly varying component of the sky that we are trying to model. Unfortunately, if there are any sharp changes in the sky level the Savitsky-Golay filtering also induces large errors in the modelled sky level near the edges. To circumvent this problem, a very simple edge detection algorithm is employed prior to Savitsky-Golay filtering. Once edges have been detected and the magnitude of the change has been determined, a step function representation of this component of the sky level is constructed. This discontinuous component is subtracted from the image, leaving only the smoothly varying component of the sky, which can then be modelled with the approach described above. Figure 6 shows sky fits for a set of scans at the same right ascension, illustrating the procedure described above. The presence of a discontinuous change in sky level can be seen in the fourth fit from the top. As a precaution, we also mask all data within 20 pixels of detected discontinuities. Subsequent to this fitting procedure, all images are normalized to have the same median sky level.

Temporal effects are not the only source of large scale variation in the sky level. In addition, two-dimensional structure is expected to be present due to galactic cirrus, reflection nebulae, scattered light, and saturated bright stars. To correct for these large scale variations we employ boxcar smoothing. Each scan is smoothed on a scale of $140''$, and then the smooth, large-scale component of the sky is subtracted. This scale is sufficiently large that high redshift clusters have a negligible contribution to the smoothing.

4.4. Registration

An important step in this survey is registration of the scans. Registration is required for several reasons, each of which requires a different degree of accuracy. First, the cleaned images must be aligned with an accuracy greater than the scale of the smoothing kernel, or else cluster fluctuations will be diluted by the misalignment. For our smoothing scale of $10''$, the scans must be aligned to $<3''$. Second, we use the registration to generate α, δ coordinates for cluster candidates, which are used for follow-up observations. For this purpose, accuracy of a few arcseconds is generally acceptable. Finally, mosaics are constructed from the images prior to object removal. These mosaics should be aligned well enough that their profiles are not bimodal although the cluster identification criteria are fairly robust to misalignment. Typical seeing during observations was between 1 and $1.5''$, so the alignment should be good to $<1''$. Considering that each scan is 3.8° (20,000 pixels) long and that the curvature of a scan varies with declination, subarcsecond accuracy is a challenging requirement.

To register the images, the IRAF routine DAOFIND is used to locate all bright stars in a scan. Using an initial estimate for the scan center and curvature of the scan (see Appendix A for a discussion of projection effects for Great Circle scans and regular scans), these stars are cross-correlated with the HST Guide Star Catalog.⁶ Actual values for the scan center and the curvature are determined

⁶ The Guide Star Catalog was produced at the Space Telescope Science Institute under U.S. government grant. These data are based on photographic data obtained using the Oschin Schmidt Telescope on Palomar Mountain and the UK Schmidt Telescope.

by maximizing the correlation with the guide stars. This cross-correlation is done for each scan, so that the scans are directly tied to a global coordinate system, which prevents the accumulation of error inherent in using relative offsets. The resulting alignment accuracy between scans is acceptable. Near the centers of scans, the alignment is generally good to $<0''.5$. This quality degrades towards the ends as small errors in curvature are amplified. In the worst regions a maximum error of $1''.5$ is reached; however, generally the error at the ends of scans is $\sim 1''$.

4.5. Mosaicing

The code we use to mosaic the scans is a modified version of the DIMSUM package for IRAF.⁷ Two mosaics are constructed at each right ascension - one of the scans prior to object removal and one after object removal. Our only noteworthy modification to the DIMSUM package is with regard to the way in which masking is handled. Masking was used for:

1. Bright stars and galaxies, for which cleaning is insufficient.
2. Bleed trails and sharp changes in the sky level, near which the sky fit may be poor.
3. Image edges, where FOCAS may fail to detect some objects.

When mosaicing, masking can be handled in two ways: one can either require that a region be unmasked in both overlapping scans for it to remain unmasked, or one can require that it be unmasked in only one of the scans and use the pixel values from the unmasked scan. The first option is preferable for objects intrinsic to the image (e.g. bright stars), and also has the advantage of maintaining uniform survey depth. However, the second option is useful if the region being masked is small or narrow, in which case continuity may be more important than uniform survey depth (particularly for FOCAS object detection). We utilize the first approach for bright objects, bleed trails, and sharp changes in sky level, but use the second approach for scan edges.

4.6. Smoothing and Detection

We next convolve the cleaned images with a smoothing kernel to increase signal-to-noise prior to cluster detection. Optimal signal-to-noise is achieved when both the kernel profile and scale are matched to cluster properties (see Phillipps & Davies 1991, for a thorough discussion of the topic). For an exact match, the surface brightness value in the convolved image will correspond to the central surface brightness of the object, while mismatch will lower the observed central surface brightness. We expect some degree of mismatch in this survey both because we are probing a range in redshift and cluster mass (and hence scale), and also because it is doubtful that high-redshift clusters

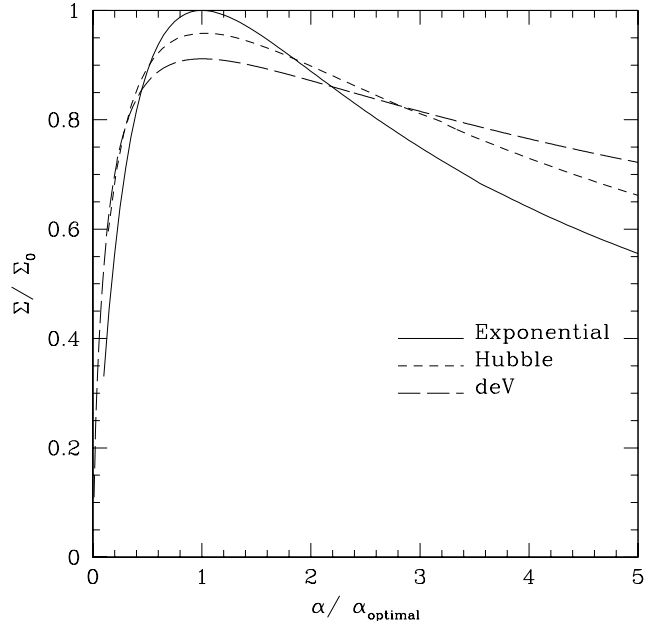


FIG. 7.— Fractional decrease in the observed surface brightness as a function of the relative mismatch between the filter scale length, α , and the optimal scale length, α_{optimal} . The curves shown correspond to an exponential filter convolved with exponential, Hubble, and de Vaucouleurs profiles.

exhibit symmetric, uniform surface brightness profiles. Further, we choose to employ an exponential kernel for the LCDCS - which is probably not the correct profile for high-redshift clusters.⁸ Consequently, it is useful to assess the impact of these factors upon our sample.

To quantify the expected degradation due to our choice of kernel, we compute the maximum cross-correlation for convolution of an exponential kernel with Hubble and de Vaucouleurs profiles. If the scale of the kernel is optimally matched to the scale of the profile (see below), then use of an exponential kernel results in net decreases in the observed peak surface brightness of 4% and 9%, respectively, for these profiles. Thus, we expect that our use of an exponential kernel has minimal impact upon our detection efficiency. Of greater importance is the choice of scale length for the kernel. Figure 7 shows the fractional decrease in the observed surface brightness for various profiles as a function of the ratio of the actual kernel scale length to the optimal kernel scale length. For all profiles, the fractional loss is $<15\%$ when the scale is matched to within a factor of two.

For the LCDCS, we set the scale length of our kernel to optimize our ability to detect clusters at $z = 1$. If we assume a Hubble profile for the cluster, then optimal scale length for our kernel is $\alpha = 0.6r_c$, where r_c is the Hubble core radius. (This is equivalent to setting the scale length such that both the exponential and the Hubble profile fall off to half the central surface brightness at the same radius). For rich clusters typical core radii are

⁷ The DIMSUM package can be obtained from <ftp://iraf.noao.edu/contrib/>

⁸ Our use of an exponential kernel is motivated by several factors. First, it is unclear what may constitute a "typical" profile at high-redshift, where clusters may be far from virial equilibrium. An exponential has the advantage of providing only minimal degradation to do mismatch for a range of profiles including Hubble and de Vaucouleurs, and also gives a bit less weight to large radii (where the signal-to-noise is lower) than a Hubble profile. Second, in absence of a single preferred profile, the exponential is convenient since we also intend to use this data set to construct a catalog of low surface brightness and dwarf galaxies.

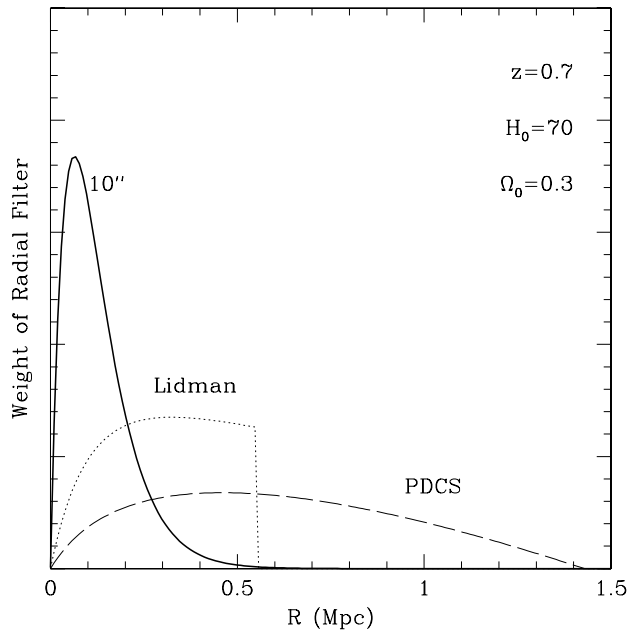


FIG. 8.— Radial filter weights from the LCDCS, PDCS (Postman et al. 1996), and an optical survey by Lidman & Peterson (1996). The filter weight is defined as $rf(r)/\int rf(r)dr$, where $f(r)$ is the filter profile. For the LCDCS most detection power is contained within 300 kpc at $z=0.7$. In contrast, the other surveys shown, which use galaxy counts, have most of their detection power at much larger radii.

$r_c \sim 100 - 150h^{-1}$ kpc, so the kernel size should be $60-90 h^{-1}$ kpc ($12-18''$ at $z = 1$ for an $\Omega_0 = 0.3$ open model, or $11-16''$ for an $\Omega_0 = 0.3$ flat model). Since the core radii for clusters at this redshift may be smaller than local systems, we choose to use a slightly smaller scale length of $10''$. This choice of smoothing kernel does yield a factor of three mismatch at $z = 0.4$, which corresponds to about a 20% fractional loss for Hubble or de Vaucouleurs profiles.

The extent of the kernel used for this survey is significantly smaller than those utilized for other optical surveys, with all the power coming from within $250 h^{-1}$ kpc (see Figure 8). Because other surveys rely on number counts, by necessity their kernels typically have scale lengths of order 1 Mpc in order to include enough galaxies to generate a statistically reliable signal. Unfortunately, use of such a large kernel increases the likelihood of inclusion of poor systems due to projection effects or large scale structure. Our small kernel minimizes projection effects and, because our method can detect cluster cores in the absence of a well-formed envelope, we have a greater probability of detecting clusters at early evolutionary stages. Conversely, it is possible that this technique will produce multiple, distinct detections for clusters with significant substructure. While this effect is a concern, we anticipate that it is a minor issue because we see no enhancement in the angular correlation function at small separations. Another possible concern is whether we detect subclumps of dwarf galaxies in nearby Abell clusters. Again, we see no evidence of correlation between the locations of our candidates and Abell clusters in the survey region (see Figure 13 in §6), and therefore expect that such detections do not

significantly impact the catalog.

Once a smoothed version of a scan region has been generated, SExtractor v2.1.6 (Bertin & Arnouts 1996) is employed to detect positive brightness fluctuations. SExtractor is used instead of FOCAS because of its computational efficiency and a superior ability to deblend overlapping detections. The detection threshold is set such that all fluctuations with peak surface brightness in excess of $\mu_W = 28$ mag arcsec $^{-2}$ ($\sim 5.4 \times 10^{-3}$ counts s $^{-1}$ arcsec $^{-2}$) are identified. For a typical scan set covering 7.6 square degrees this procedure yields ~ 2500 detections. Of these, roughly 65% are in the 5.9 square degree overlap region used for the cluster survey (of which $\sim 30\%$ is typically masked).⁹ About 5% of these detections are galaxy clusters at $z > 0.3$; the rest are contamination. We use an automated classification technique, described in the next section, to identify viable cluster candidates.

5. CLUSTER IDENTIFICATION

A critical element in creating the cluster catalog is identification of viable cluster candidates and rejection of other sources of surface brightness fluctuations. Several techniques were explored for isolating cluster candidates including hierarchical, divisive, and fuzzy clustering algorithms (Gordon 1981; Jain & Dubes 1988) and automated Bayesian classification (Cheeseman et al. 1988; Goebel et al. 1989), with each method using as input a generalized set of statistics characterizing the detection image. A drawback of these algorithms though is that the physical meaning of the resulting classes is not always clear, nor is it straightforward to reproduce these classes for simulated data or new samples (particularly for the fuzzy and Bayesian techniques). Consequently, we instead choose a more intuitive and easily reproducible approach for extracting cluster candidates that yields a success rate comparable to the other approaches. We identify classes of objects that induce fluctuations and separately isolate these classes utilizing specific properties unique to the given type of object.

To do so, we employ information from both the smoothed and original images. From the smoothed maps, we use:

1. The observed peak brightness, Σ_{obs} , of the detected surface brightness fluctuation. It is defined as the maximum surface brightness value in any pixel in the fluctuation, and the units of Σ_{obs} are counts s $^{-1}$ arcsec $^{-2}$.
2. The concentration, C , of the observed surface brightness fluctuation. We define the concentration in terms of the fraction of pixels above a given threshold for two regions - an inner, circular region of radius $15''$ and an outer annulus extending from $15-30''$. C is one minus the ratio of the fraction above the threshold in the outer annulus, f_o , to the fraction above the threshold in the inner region, f_i :

$$C \equiv 1 - \frac{f_o}{f_i}. \quad (1)$$

⁹ The overlap region constitutes 78% of the survey area, but only has 65% of the detections. This difference is a direct result of the lower signal-to-noise ratio outside the overlap region leading to more spurious detections.

The threshold is set such that $\Sigma_{threshold}=4.2\times 10^{-3}$ counts $s^{-1} \text{ arcsec}^{-2} = 2/3 \Sigma_{lim}$, the limiting surface brightness of the final catalog (see §6).

3. The fraction of the detection region that is masked. We measure the fraction of masked pixels within a $1' \times 1'$ square region centered on the surface brightness fluctuation.

From the original images we obtain photometric data about objects located near the fluctuation, which enables us to discern whether the detection was caused by a low surface brightness galaxy, bright star, or nearby galaxy rather than by a cluster. Specifically, we measure:

1. The $5''$ aperture magnitude, m_{ap} , of the brightest object (lowest m_{ap}) located within $15''$ of the peak of the surface brightness fluctuation detected in the smoothed data.
2. The aperture magnitude, total magnitude, central surface brightness, and full-width half maximum of the non-stellar object with the brightest m_{ap} located near the detected fluctuation. In identifying this object we consider all sources located within $15''$ of either the peak or the centroid of the detected fluctuation. An object is designated non-stellar if the stellarity index $S < 0.97$ or $m_{ap} > 20$. The latter constraint reflects a preference at fainter magnitudes to be conservative and potentially include a few stars rather than reject galaxies as stars. As will be described in §7, this aperture magnitude is used to estimate cluster redshifts, and it is preferable to occasionally underestimate a redshift due to stellar contamination rather than overestimating the redshift due to identification of the brightest cluster galaxy as a star. The total magnitude, m_T , is mag_best in SExtractor.
3. The aperture magnitude, total magnitude, central surface brightness and full-width half maximum of the object with the lowest m_T located within $15''$ of either the peak or the centroid of the detected fluctuation.
4. The number of galaxies, n_{gal} , brighter than $m_{ap}=22$ mag within $30''$ of the fluctuation.

The quantities listed above prove sufficient for classification of most detected surface brightness fluctuations. Prior to classification, we eliminate all detections that lie in regions where $E(B-V) > 0.10$ (Schlegel, Finkbeiner, & Davis 1998). This criteria removes all detections at $\alpha > 15h12m$, where the data are at low galactic latitude, and an additional 32 detections at lower right ascension that would otherwise be included in the statistical catalog (see §6). We also eliminate all detections lying in regions that, based on visual inspections of IRAS maps obtained from SkyView (McGlynn, Scollick, & White 1996) and the smoothed optical maps generated in this work, contain galactic cirrus with significant structure. We do so because galactic cirrus both reflects optical light and produces extended red emission from 6000-8000Å (Guhathakurta &

Tyson 1989; Szomoru & Guhathakurta 1998), and nonuniformity in this emission/scattered light generates surface brightness fluctuations that are indistinguishable from cluster-induced fluctuations. An example of this phenomenon is shown in Figure 9. Finally, to preserve a constant threshold for the survey, a target is only considered a cluster candidate if the detection lies in a region that was observed twice during the course of the survey. All other detections are flagged and removed from further consideration. We then proceed by identifying the physical origins of the remaining fluctuations and sequentially isolating classes of objects. The types of objects, and parameters used to isolate them, are described below.

Stars - As described in § 4, all detected objects in the drift-scan data are replaced with local, random sky pixels. This procedure effectively removes most resolved objects; however, for bright stars the ‘sky’ pixels used to replace the star often contain a non-negligible amount of light from the wings of the stellar point spread function. As a result, a surface brightness fluctuation is produced coincident with the star for stars with $14.5 < m_{ap} < 18.5$. For $m_{ap} < 14.5$ the stars are masked; for $m_{ap} \gtrsim 18.5$ the stars are sufficiently faint that they do not induce detectable fluctuations. Fluctuations induced by bright stars are cleanly isolated using the stellarity index and magnitude of the brightest object near the fluctuation. We classify a detection as being induced or strongly influenced by a star if the brightest object within $15''$ of the peak of the detection has a stellarity index $S > 0.9$ and $m_{ap} < 18.5$. Stars are responsible for half of all detections.

Galaxies - Individual galaxies can also cause detectable surface brightness fluctuations if they have significant flux at large radii. As with bright stars, the local ‘sky’ pixels used to replace the core of the galaxy produce a surface brightness feature coincident with the original location of the galaxy. To minimize contamination of the cluster catalog by these detections, we impose two criteria. First, we classify a detection as a galaxy-induced if there is a galaxy with $m_T < 18.75$ within $15''$ of the peak or centroid of the detection (which is about a quarter of a magnitude brighter than a typical BCG at $z=0.30$).

We augment this procedure with a second cut that takes into account the surface brightness of the detection and the number of galaxies within $30''$ of the detection. If the brightest galaxy near the fluctuation is the brightest cluster galaxy (BCG), then the fluctuation should be significantly brighter than one induced by an isolated, local galaxy of the same apparent magnitude. In addition, at $z \sim 0.3$ we should be able to identify projected galaxy overdensities associated with real clusters. To discriminate low-redshift clusters from isolated galaxies, we define the parameter p_{gal} such that

$$p_{gal} = \sqrt{(2.5 * (\Sigma_{obs}/\Sigma_{det} - 1))^2 + (n_{gal} - 1)^2}, \quad (2)$$

where $\Sigma_{det}=5.4\times 10^{-3}$ counts $s^{-1} \text{ arcsec}^{-2}$ is the detection threshold of the survey. Using this parameter, we classify detected fluctuations as galaxies if

$$p_{gal} < 2.5 - 6(m_{ap} - 20). \quad (3)$$

This criteria is empirical, constructed from visual inspection and follow-up imaging of candidates at $10h < \alpha < 10h15m$ ($\sim 5\%$ of the survey). No detections are eliminated when $m_{ap} \gtrsim 20.4$, which means that this cut has

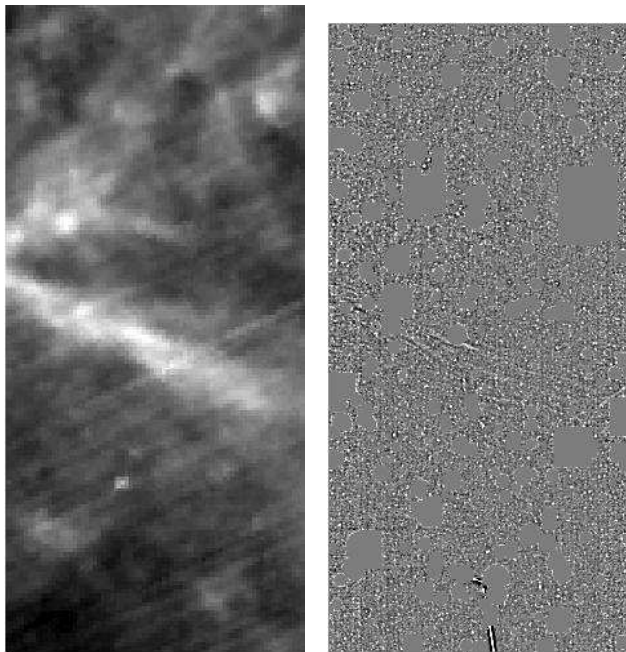


FIG. 9.— Comparison of an IRAS 60μ image (left) and smoothed optical map (right) of a small section of the survey. The images are $1.9^\circ \times 3.9^\circ$ in size. East is up and north is to the right. Note the large cirrus spike evident in the center of the IRAS image. In the optical image the large scale structure of the spike is filtered during sky removal; however, small scale features persist and can be seen in the optical map. Consequently, via inspection of the IRAS and optical maps we catalog these regions and reject all detections in these areas. Note also the satellite trail at the lower edge of the optical image. Satellite detections that survive the automated selection criteria discussed in §5 are manually removed from the final sample.

no impact on the final catalog at $z_{est} \gtrsim 0.35$ (see §7.3). Together the galaxy identification criteria eliminate 14% of all detections.

Low Surface Brightness and Dwarf Galaxies - After elimination of fluctuations caused by stars and galaxies, we identify detections induced by low surface brightness galaxies (LSBs) and dwarf galaxies. To identify these galaxies, we rely on the SExtractor information from the original images for the two galaxies within $15''$ that have the brightest aperture and total magnitudes. Qualitatively, if a galaxy is a nearby LSB or dwarf, we expect that the central surface brightness will by definition be low, the FWHM will be relatively large since the galaxy is nearby, and the total magnitude will be much larger than the aperture magnitude (due to the previous two traits). We employ a two-stage approach to eliminating LSBs. First, we identify detections as potentially induced by LSBs if $m_{ap} - m_T > 1.25$ for either of these two nearby, brightest galaxies. Second, we define the parameter, p_{LSB} ,

$$p_{LSB} = FWHM - 1.2m_T + 11.5, \quad (4)$$

and eliminate detections as likely LSBs if $\mu_0 > 22$ mag arcsec $^{-1}$ and $p_{LSB} > 0$ for either of these two galaxies (see Figure 10). This constraint, which is again empirical, is calibrated via visual inspection. A total of ~ 250 detections in the entire survey are classified as LSB candidates based upon these criteria. By visual inspection of these detections, we estimate that ~ 5 clusters with $\Sigma_{obs} > 6.25 \times 10^{-3}$ counts s $^{-1}$ arcsec $^{-2}$ are lost due to misidentification as LSBs. Conversely, ~ 20 LSBs are mistakenly identified

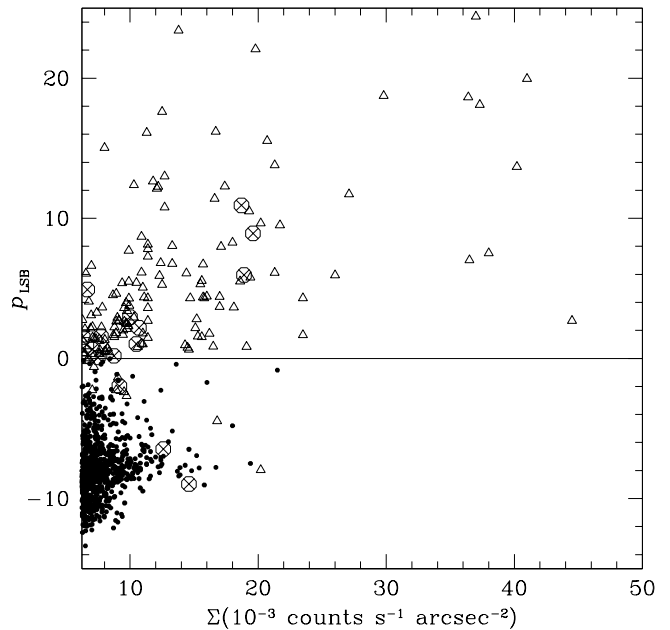


FIG. 10.— Criteria used to isolate LSBs. Filled circles are clusters, triangles are low surface brightness galaxies, and circled crosses are systems that are visually ambiguous when classified by eye from the scans. Detections with $p_{LSB} > 0$ are identified as probable LSBs. The data plotted represent data from the entire survey. Only the first 10% of the survey region was used to calibrate this division, but all sources designated as LSBs or clusters were visually inspected after automated classification to verify the effectiveness of this procedure.

as clusters and included in the final catalog.

Partially masked detections - We next eliminate from the statistical sample all other detections for which greater than 10% of the detection region is masked. Such obscuration of the detection region leads to difficulty in determining the true cause of a detection, and consequently results in increased contamination of the cluster sample.

Scattered light and assorted spurious reduction-induced signals - Subsequent to the removal of all of the sources listed above, $\sim 8\%$ of the total detections remain. Of these, the principal remaining contaminants are sources arising from scattered light and signals related to the reduction process. As a class, these detections are characterized by low peak surface brightness and large spatial extent relative to the clusters. To isolate these, we use the concentration measure, C , as a discriminant. Detections of this type are on average less concentrated (lower C) than clusters of comparable surface brightness. The division between the two classes is shown in Figure 11.

Satellites and Bleed Trails - Satellites and bleed trails from saturated stars, because they are not detected by FOCAS and replaced with sky pixels, also induce fluctuations. These sources are rare and easily identifiable, and so they are identified by visual inspection. This is the only aspect of the classification procedure that is not automated.

Tidal Features - Another source of detections is tidal features in nearby, interacting systems. We do detect fluctuations induced by large tidal features; however, we do not identify these as a distinct class of objects when generating the cluster catalog. Tidal features, because of their varied morphologies, are difficult to identify via

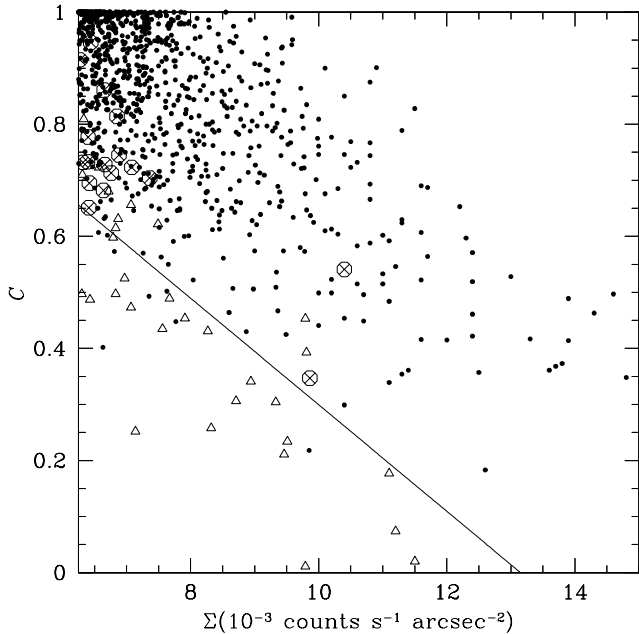


FIG. 11.— Criteria used to eliminate spurious detections. Filled circles are clusters, triangles are spurious detections, and circled crosses are systems that are visually ambiguous. The data plotted are drawn from the entire survey region.

automated criteria. Fortunately, however, the surface density of interacting systems capable of inducing detections is low. From visual inspection, we estimate the fractional contamination by tidal tails is $\sim 1\%$ in the final catalog.

Chance Galaxy Superpositions - Chance superpositions of several field galaxies with magnitudes near the survey limit provide a final source of contamination. Such detections are indistinguishable from true cluster detections, and so can only be eliminated with deeper follow-up imaging. While it is difficult to robustly estimate the magnitude of this contamination directly from the survey data, these superpositions may be the primary source of false detections in the final catalog (see 7.2 for observational constraints on the net contamination rate).

Clusters - All of the remaining 2670 detections are cluster candidates. As will be discussed in §6, not all of these systems are included in the final statistical catalog; however, we consider all these detections to be viable candidates. The properties of the sample are discussed in further detail in §7.

6. THE CATALOG

Having established our selection criteria, we now define the main, statistical catalog for the Las Campanas Distant Cluster Survey. This statistical sample is designed to be an automated, reproducible catalog with which to study properties of the cluster population as a whole. For this catalog, we impose two additional constraints beyond those discussed in §5. First, we restrict the catalog to detections with $\Sigma_{obs} > 6.25 \times 10^{-3} \text{ counts s}^{-1} \text{ arcsec}^{-2}$. This restriction is due to relatively high contamination for fainter systems, as determined by follow-up imaging. Second, we restrict the sample to clusters at $z > 0.30$. Below this redshift incompleteness and confusion with individual galaxies become significant issues.

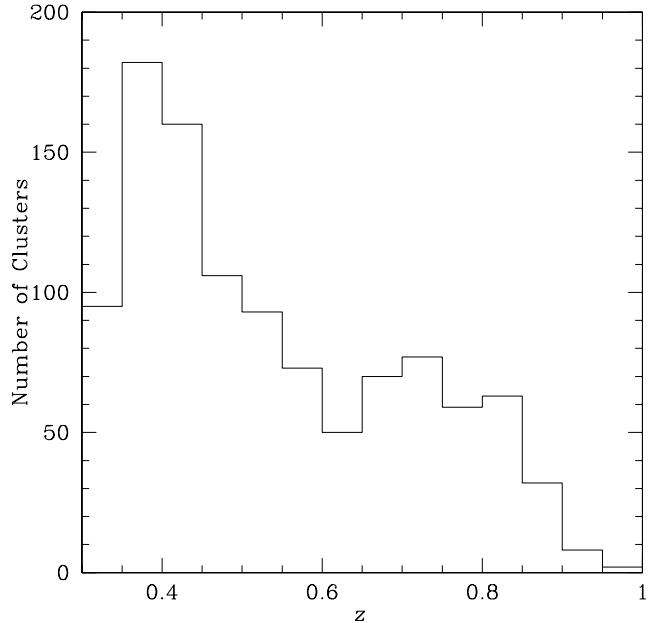


FIG. 12.— Redshift distribution of clusters in the statistical catalog.

There are a total of 1073 cluster candidates in the statistical catalog. These candidates are drawn from a net survey area, after masking, removal of regions of high extinction, and rejection of data in close proximity to bright stars and galaxies, of 69 square degrees. Equivalently, the projected density of cluster candidates is 15.5 per square degree, which is comparable to the PDCS and EIS catalogs (13.4 per square degree for the primary PDCS sample, and 21.1 per square degree for the full EIS sample). As the redshift baselines of these three surveys is slightly different, a more fair comparison is the projected density of clusters at $0.3 \leq z \leq 0.8$. Within this range, the LCDCS, PDCS and EIS find projected densities of 14.2, 10.8, and 10.7 candidates per square degree, respectively. The higher projected density of the LCDCS is likely an indication that we probe to slightly lower mass, but may also be partly due to higher contamination (see §7.2).

Table 1 lists all candidates in the catalog. For each candidate, we provide an identification number in Column 1, right ascension in Column 2, and declination in Column 3. Estimated redshift, the derivation of which is described in §7.3, is given in Column 4. Subsequent columns list observed surface brightness, Σ_{obs} , in $10^{-3} \text{ counts s}^{-1} \text{ arcsec}^{-2}$ (Column 5), extinction corrected surface brightness, Σ_{cor} , in $10^{-3} \text{ counts s}^{-1} \text{ arcsec}^{-2}$ (Column 6), and the $B-V$ extinction from Schlegel, Finkbeiner, & Davis (1998) (Column 8). For the extinction correction, we take $A_W = 3 E(B-V)$, which is the average of the published values for A_V and A_R (see Figure 1 for a comparison of W with these passbands). Finally, Column 9 contains additional information for some candidates, including notes for objects that from inspection are obviously not clusters. All observed surface brightnesses have an associated uncertainty of $1.6 \times 10^{-3} \text{ counts s}^{-1} \text{ arcsec}^{-2}$ (see §7.1); derivation of the uncertainty for the extinction-corrected values is straightforward. Figure 12 gives the redshift distribution of these candidates, and Figure 13 shows the projected dis-

tribution overlaid with the locations of Abell clusters. In Figure 14 we show detection images for seven candidates covering the redshift range of the survey.

The statistical catalog is the primary sample presented in this paper. However, because the interests of researchers who use this catalog may be diverse, we have also constructed a smaller, supplemental catalog that contains additional cluster candidates. These supplemental targets are detections that failed one or more of the automated criteria for inclusion in the statistical sample, but visually appear to be highly probable cluster candidates. For this supplemental catalog, we maintain the restriction $\Sigma_{obs} > 6.25 \times 10^{-3} \text{ counts s}^{-1} \text{ arcsec}^{-2}$, and no attempt was made to recover clusters that were mis-classified as stars, or detection for which more than 50% of the detection region was masked. We do, however, re-evaluate all detections rejected on the basis of extinction, lesser masking, identification as an LSB, or identification as a spurious feature. We also relax the galaxy rejection criteria such that clusters may have $z < 0.30$ and $m_T < 18.75$. From this extended sample we visually identify 112 additional cluster candidates. Table 2 lists the supplemental targets, including the reason for rejection from the statistical sample. We note that the Σ_{obs} values of clusters rejected due to masking should be used with caution, as partial masking can skew this quantity. The redshift distribution of the supplemental catalog is comparable to the statistical catalog for $z \lesssim 0.65$. At higher redshift there are more candidates in the statistical catalog, due both to contamination in the statistical catalog and failure to visually identify high redshift candidates for the supplemental catalog.

7. SAMPLE PROPERTIES

To maximize the utility of this sample, we must constrain four key properties of the catalog. Specifically, we need to determine the completeness of the sample, the contamination rate, the redshift distribution, and the mass limit of the survey as a function of redshift. Further, if possible, we wish to estimate redshifts and masses for individual systems directly from the survey data. We address each of these issues below.

7.1. Completeness

To quantify the completeness of the sample and uncertainties in measured parameters, we run simulations in which a dozen of the detected cluster candidates - including several below the surface brightness threshold of the statistical catalog - are randomly reinserted into the survey data. Information about these clusters, which were selected to span a range of surface brightness and redshift, is given in Table 3. These simulations are specifically aimed at measuring completeness as a function of surface brightness and scatter in the observed values of Σ_{obs} for clusters similar to the ones that we detect in the LCDCS. A corollary concern is whether we systematically miss any subset of the cluster population. If so, then the completeness rate derived from these simulations will overestimate the actual value. Figure 7 implies that our ability to detect clusters is not strongly dependent upon the core radius. In addition, we have obtained survey quality drift-scan imaging of 17 clusters at $z = 0.35 - 0.85$ drawn from published optical and X-ray catalogs to test for any

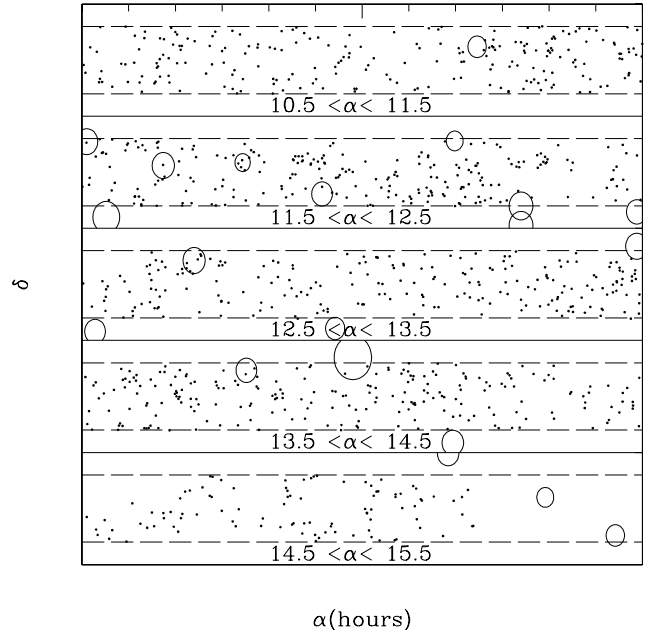


FIG. 13.— The projected distribution of cluster candidates in the LCDCS, subdivided by right ascension. In all panels, the dashed lines correspond to the declination range of the survey ($-13^\circ < \delta < -11.5^\circ$). The overlaid circles correspond to the Abell radii for Abell clusters within the field of view of the survey.

systematic bias in our detection method. For this sample, which spans a wide mass range (see Figure 19 in §7.4), our observations have resulted in successful detection on 16/17 clusters (Gonzalez 2000). The undetected cluster, PDCS 8, has a published $3\text{-}\sigma$ upper limit on the X-ray luminosity, $L_X = 9.8 \times 10^{43} h_{50}^{-2} \text{ erg s}^{-1}$ (0.4-2 keV, $\Omega_0 = 1$) for an estimated redshift $z=0.6$ (Holden et al. 1997). We thus anticipate that we are not systematically missing a significant fraction of the cluster population due to our detection method, but caution that such a bias may exist.

To quantify the completeness and scatter, we insert the clusters throughout the entire survey region. The inserted data consist of $140'' \times 140''$ (200×200 pixel) image sections centered on the clusters. Insertion points are chosen at random, but with the criteria that the position be in the overlap region of the survey and not lie beneath a mask. No pre-selection is made based upon extinction or proximity to prominent cirrus features, and so 16% of the inserted clusters are rejected on these grounds. These rejected clusters are not considered in computing the completeness, as they are already accounted for in the determination of the effective survey area. We use different random locations for each candidate, and each of the 12 candidates is inserted into the survey images 264 times (12 insertions per candidate in each of the 22 mosaics). To avoid crowding effects, only 72 clusters are inserted into a mosaic for each run of the simulations.

We track the detection rate and the rate at which a candidate will be included in the statistical catalog. In addition to determining the completeness, we also use this data to quantify the rms uncertainty in Σ_{obs} . We find that the standard deviation is $\sigma_\Sigma = 1.6 \times 10^{-3} \text{ counts s}^{-1} \text{ arcsec}^{-2}$, independent of Σ_{obs} , which corresponds to roughly 25% uncertainty at the faint limit of the statistical catalog. This scatter defines the limiting precision with which we

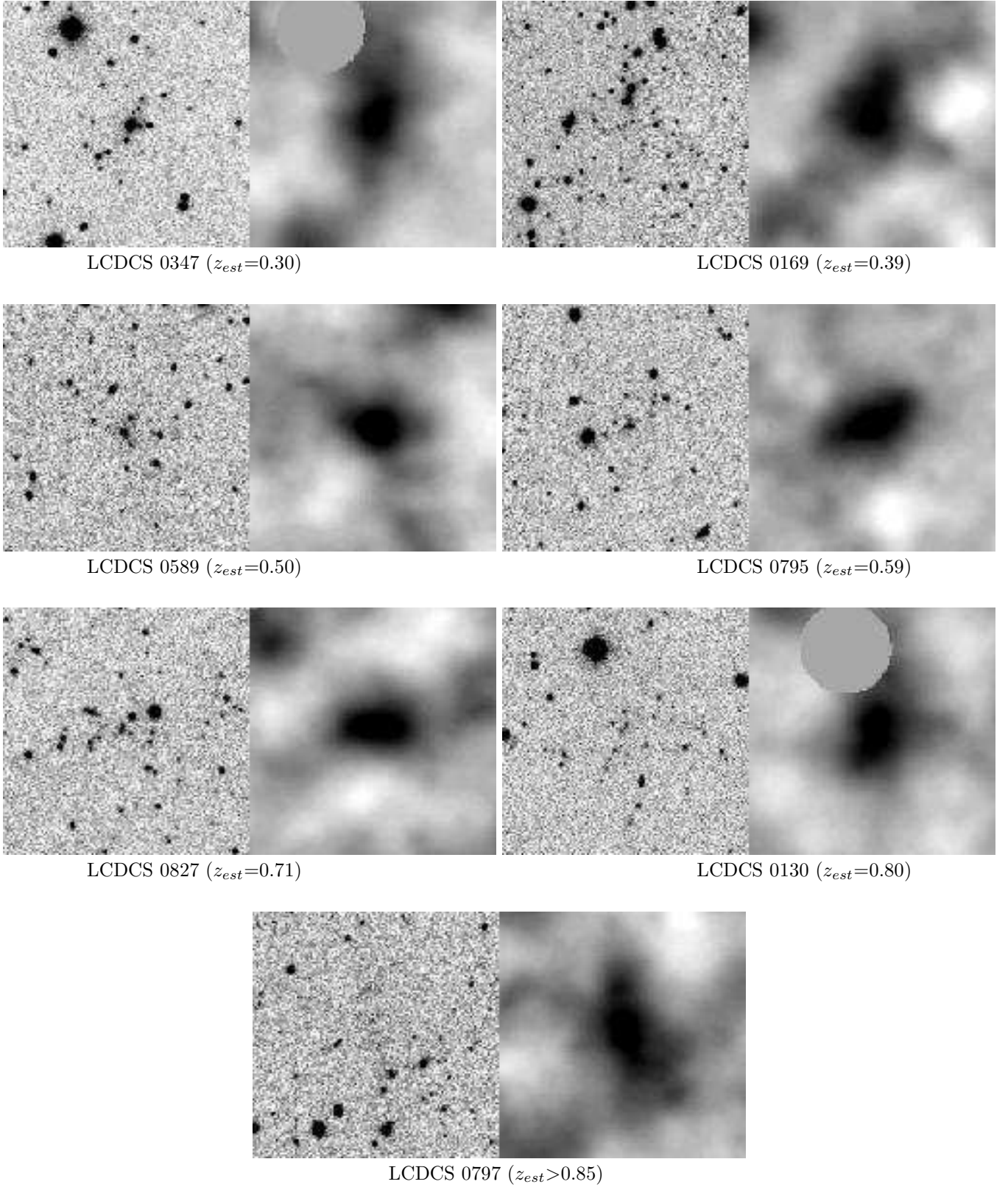


FIG. 14.— Detection images for seven of the candidates in the LCDCS catalog. The candidates shown were chosen to uniformly span the redshift range of the survey. Further, all candidates shown have $\Sigma_{obs}=9.5\times 10^{-3}$ cts s $^{-1}$ arcsec $^{-2}$, except for LCDCS 0797 ($\Sigma_{obs}=7.9\times 10^{-3}$ cts s $^{-1}$ arcsec $^{-2}$).

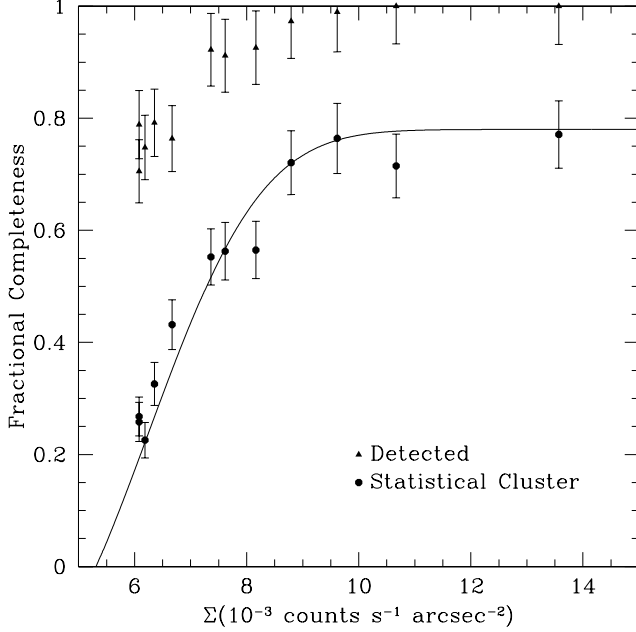


FIG. 15.— Fractional completeness of the catalog as a function of surface brightness. Triangles indicate the probability that a cluster is detected, assuming that it does not lie directly beneath a mask. Circles indicate the probability that a cluster is included in the statistical catalog. The solid curve is an analytic model for the completeness of the statistical catalog (see text).

can estimate velocity dispersions for candidates in the sample (see §7.4).¹⁰

The results of these simulations can be seen in Figure 15 and are listed in Table 3. The detection rate is near 100% for $\Sigma_{obs} > 8.5 \times 10^{-3}$ counts s⁻¹ arcsec⁻². Of these bright candidates, 78% qualify for inclusion in the statistical catalog. The majority of those that fail to be included in the catalog are rejected due to proximity to either a star or a mask, which together eliminate $\sim 20\%$ of candidates. Proximity to bright galaxies eliminates most of the remaining detections. Assuming that the incompleteness at low surface brightness is the result of Gaussian uncertainty in Σ_{obs} , the expected completeness of the statistical catalog can be modelled as

$$F(\Sigma_{obs}) = F_0 \times \frac{\text{erf}((\Sigma_{obs} - \Sigma_{lim})/\sqrt{2}\sigma_{\Sigma}) + \text{erf}(\Sigma_{obs}/\sqrt{2}\sigma_{\Sigma})}{1 + \text{erf}(\Sigma_{obs}/\sqrt{2}\sigma_{\Sigma})}, \quad (5)$$

where F is the fractional completeness, and F_0 is the maximum fractional completeness at high Σ_{obs} . This model is overlaid in Figure 15 with $\Sigma_{lim} = 6.25 \times 10^{-3}$ counts s⁻¹ arcsec⁻², $\sigma_{\Sigma} = 1.6 \times 10^{-3}$ counts s⁻¹ arcsec⁻², and $F_0 = 0.78$.

7.2. Contamination Rate

We utilize follow-up imaging to assess the false detection rate in the LCDCS. While this approach provides the most direct means of quantifying the contamination, care must be taken to insure that the derived result is not biased. The imaging that we have can be divided into two sets, both of which are described in detail in Nelson et

al. (2001a). The first set is deep, multi-color imaging obtained in 1996 and 1997 with the Las Campanas 1m and 2.5m telescopes. From these runs, most targets have in excess of 1 hour of imaging on the 1m (or 20 minutes on the 2.5m) in both V and I . These data are sufficiently deep to determine whether a candidate is a cluster; however, some of the targets observed were included specifically because they looked promising in the drift-scan imaging. As a result, an assessment of the contamination based upon these data may *underestimate* the true contamination rate. The second set of data consists of shallower, I -band imaging obtained with the same telescopes in 1998. For this run care was taken to avoid inducing a similar selection bias, and the candidate clusters that were observed are representative of the sample as a whole. Because this data set is shallow, some true clusters may be incorrectly identified as spurious, and so an assessment based upon this data may *overestimate* the true contamination rate.

For each candidate we compute the number density of galaxies within a $100 h^{-1}$ kpc aperture centered on the surface brightness fluctuation ($\Omega_0=0.3$, $\Omega_{\Lambda}=0.7$; see §7.3 for an explanation of the redshift estimates). We classify targets as clusters if the number density of galaxies in this aperture exceeds the background level by $2\text{-}\sigma$. Furthermore, we test the probability that random number density fluctuations in our fields will exceed this threshold by computing the density contrast for a complementary set of random locations. For the deep, multi-color data set we find that 23/32 (72%) candidates and 3/32 (9%) random fields exceed this threshold. We therefore derive a net contamination rate of $31 \pm 9\%$ (i.e. $n_{cl}/N = (n - n_{random})/(N - n_{random})$, where N is the total number of targets, n is the number of $>2\text{-}\sigma$ detections, and n_{cl} and n_{random} are the number of cluster and random field detections). For the shallower data set we find that 42/57 (74%) of candidates and 4/57 (7%) of random fields exceed this threshold, yielding a net contamination rate of $28 \pm 7\%$. Because we expect that the two data sets provide lower and upper bounds on the contamination rate, the concurrence of these two estimates is encouraging. Combining the data sets, our estimate of the contamination rate is $29 \pm 5\%$, with the quoted error bar reflecting purely Poisson uncertainty. We also intend to use additional deep, multicolor observations for contiguous subfields, including data from the Deep Lens Survey,¹¹ to provide an improved constraint in the near future.

Finally, the fractional contamination increases with estimate redshift, which is a consequence of the method we used to estimate redshifts. As described in §7.3, we estimate redshifts for cluster candidates using the BCG magnitude-redshift relation. For false detections (which by definition lack a BCG), the galaxy identified as the “BCG” will be a random field galaxy along the line of sight. As a result, the distribution of redshifts assigned to false detections is determined by the magnitude distribution of field galaxies. A detailed discussion of the redshift dependence of the contamination is provided in Gonzalez (2000).

¹⁰ Intrinsic scatter in Σ_{cor} is also a concern; however, the scatter in the $\sigma - \Sigma_{cor}$ relation (see Figure 19a) is consistent with arising purely from our observational uncertainty.

¹¹ <http://dls.bell-labs.com/>

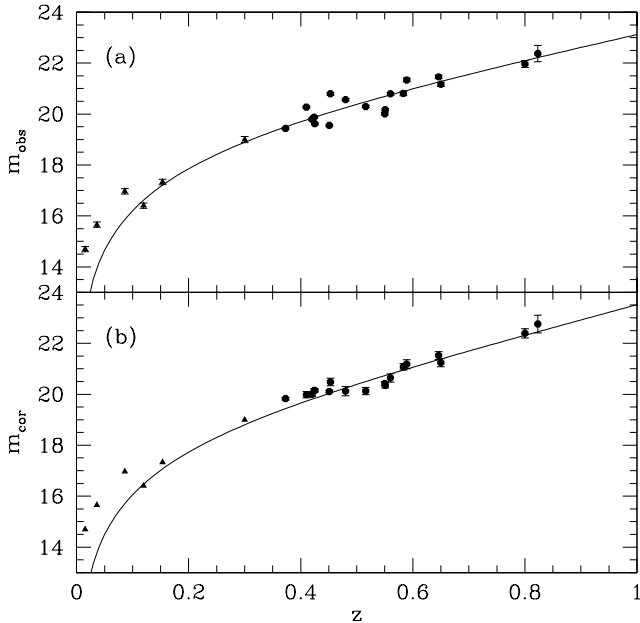


FIG. 16.— (a) BCG magnitude-redshift relation with no correction for Σ_{cor} . The solid line is an unweighted least squares fit to the data of the function given in Equation 8. (b) BCG magnitude-redshift relation including a Σ_{cor} correction. The solid line is an unweighted least squares fit to the data of the function given in equation (2). For both plots, only the data points at $z > 0.35$ (circles) are used to calibrate the relation. The lower redshift clusters (triangles), which are known clusters that lie in our survey region, lack measured values of Σ_{cor} . Further, for clusters at $z \lesssim 0.1$, the photometric aperture is significantly smaller than the BCG, and so is a poor estimate of the total luminosity.

7.3. Redshifts

To calculate an empirical redshift estimate, we obtained LRIS (Oke et al. 1995) spectra at Keck for a subset of 8 LCDCS clusters and 11 clusters from the northern hemisphere pilot survey (Dalcanton 1995; Zaritsky et al. 1997). These data were used in conjunction with data for 11 additional previously known clusters to calibrate several photometric redshift estimators (see Nelson et al. 2000a). We find that the most efficient means of estimating redshifts directly from the survey data is via the brightest cluster galaxy magnitude-redshift relation. Locally, brightest cluster galaxies have long been known to be good standard candles, with dispersions ~ 0.3 magnitudes (Humason, Mayall, & Sandage 1956; Sandage 1972a,b). Subsequent work by a number of authors has found that the scatter remains remarkably small out to at least $z \sim 1$ (Sandage 1988; Aragon-Salamanca et al 1993; Aragon-Salamanca, Baugh, & Kauffmann 1998; Collins & Mann 1998).

For our calibration data we find comparably small scatter. We identify brightest cluster galaxies in an automated fashion – we search for the brightest galaxy within a $15''$ radii of the peak and centroid of the surface brightness fluctuation from which a cluster is detected, and define this galaxy to be the BCG. This automated definition is designed to make the catalog easily reproducible, while minimizing redshift errors due to foreground contamination or failure to identify the BCG within the chosen search radius. Because we are detecting the cores of centrally condensed objects with our technique, there is a high

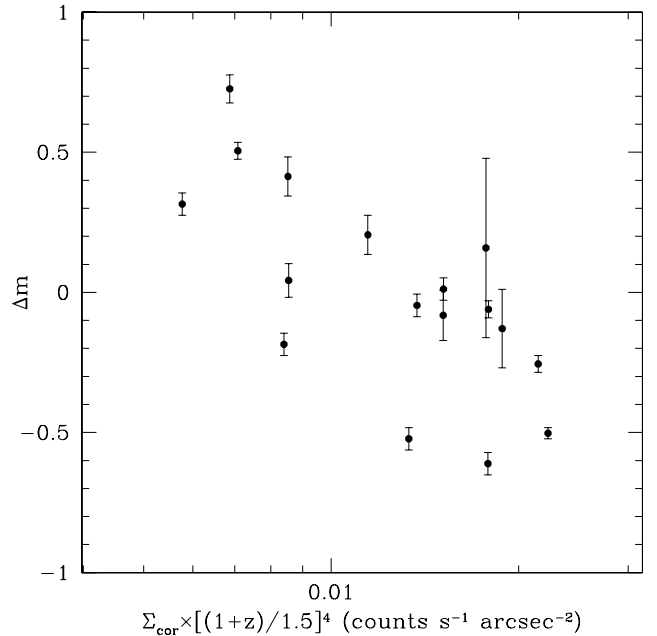


FIG. 17.— BCG magnitude residuals from Figure 16a as a function of Σ_{cor} , with $\Delta m \equiv m_{observed} - m_{fit}$. Error bars correspond to the photometric uncertainty associated with the observed BCG magnitudes.

probability that the BCG will be coincident with the surface brightness fluctuation. Further, if we do miss the BCG, the second ranked galaxy is typically ~ 0.5 mag fainter (Nelson et al. 2001b), which corresponds to a redshift error $\delta z \sim 0.1$. Of the 18 clusters used to calibrate this relation (the northern clusters were not used because they were observed in a different filter), in no instance was the galaxy identified as the BCG more than 0.5 mag fainter than predicted by the final, best-fit model.

We find that the magnitude of the brightest cluster galaxy is an effective redshift indicator. Photometry is performed using SExtractor v2.1.6 (Bertin & Arnouts 1996), and $5''$ aperture magnitudes are used. All magnitudes are extinction corrected using the maps of Schlegel, Finkbeiner, & Davis (1998). Figure 16a shows the BCG magnitude-redshift relation for our sample, with the line being a best fit to the data of the function:

$$m = M + 5 \log D_L + Bz^{7/4}, \quad (6)$$

where M is the absolute magnitude and D_L is the luminosity distance. The last term is an analytic approximation to the W -band $E + k$ correction, which is derived using the 1995 Bruzual & Charlot models (Bruzual & Charlot 1993; Charlot, Worthey, & Bressnan 1996). For the luminosity distance we fix $\Omega_0 = 0.3$ and $\Omega_\Lambda = 0$; however, precise choice of cosmology is unimportant due to degeneracy between this term and the evolution term. The scatter in this relation is $\sigma_m = 0.36$ mag for the calibration data.

To reduce this scatter we test for second-order correlations. Motivated by an observed correlation between L_X and M_{BCG} (Hudson & Ebeling 1997) and our observed correlation between T_X and Σ_{cor} (see §7.4 and Gonzalez (2000)), we test for a correlation between Σ_{cor} and m_{BCG} (Figure 17). We find that

$$m_{BCG} \propto -\log \Sigma_{cor} (1+z)^4. \quad (7)$$

To incorporate this correction, which reduces the scatter to $\sigma_m=0.26$, we replace m with

$$m_{corrected} \equiv m + A \log \frac{\Sigma_{cor} (1+z)^4}{10^{-2}(1+.5)^4}. \quad (8)$$

in Equation 6. Figure 16b shows $m_{corrected}$ as a function of redshift. Overlaid is the unweighted least-squares, which yields

$$m_{corrected} = (-21.3 \pm 0.15) + 5 \log D + (1.7 \pm 0.4)z^{7/4}, \quad (9)$$

and $A=1.5 \pm 0.3$. This is the equation that we use to estimate redshifts for candidate clusters. For the redshift range of the LCDCS, a magnitude dispersion of 0.26 mag corresponds to a redshift uncertainty of 10-11%. This constitutes a lower limit on the scatter in our redshift estimates, as there are several caveats to our method.

A first concern is that estimated redshifts beyond $z \sim 0.85$ are based upon extrapolation beyond the redshift range probed by the calibration sample, and for these clusters the magnitude of the BCG is very near the detection threshold of our survey data. Consequently, in Table 1 we simply list the redshift as $z > 0.85$ for these clusters. In addition, we caution that the size of the calibration sample is small, and so our estimate of σ_m is subject to small number statistics.

Finally, we expect that the redshift dispersion for the catalog as a whole is larger than the dispersion for the calibration data due to foreground contamination and occasional miscentering. We assess the robustness of our redshift estimates using the simulations described in 7.1. These simulations reproduce all sources of uncertainty in the estimated redshifts (e.g. foreground contamination, miscentering, scatter in Σ_{obs}) except for intrinsic BCG magnitude dispersion. Failure to identify the BCG due to miscentering turns out to be a minor issue for the clusters reinserted into the survey data. We find that for these clusters redshifts are underestimated by $\Delta z > 0.1$ less than 2% of the time, and only 1% of the time will a cluster incorrectly be assigned a redshift $z > 0.75$.¹² The largest bias in the estimated redshifts is due to foreground contamination. While negligible at $z < 0.5$, by $z = 0.8$ foreground contamination leads the redshift to be underestimated by $\Delta z > 0.1$ 35% of the time. In addition, dispersion in Σ_{obs} induces a Gaussian uncertainty in the estimated redshift of magnitude $\sigma_z = 0.02$. Combined with the intrinsic dispersion in BCG magnitude, these factors lead us to expect an rms redshift uncertainty of $\sim 13\%$ for low-redshift clusters in the final catalog, rising to $\sim 20\%$ by $z \sim 0.8$. We

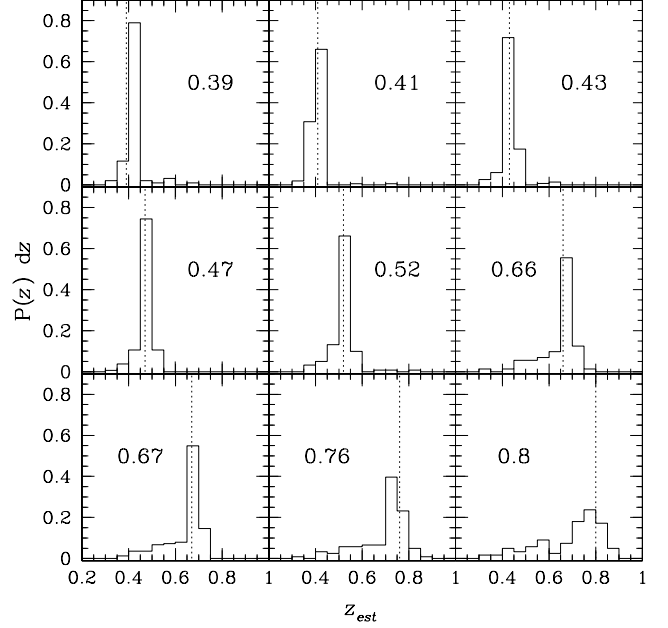


FIG. 18.— Simulated distribution of estimated redshifts for the nine clusters with $\Sigma_{obs} > 6.25 \times 10^{-3}$ counts s^{-1} arcsec $^{-2}$. The vertical dashed line is the original estimated redshift, the value of which is given in each panel, while the histogram shows the distribution of derived z_{est} when a cluster is randomly reinserted into the survey data. The most notable systematic bias is a tendency to underestimate the redshifts of distant systems due to foreground contamination.

emphasize though that this scatter is non-Gaussian due to the impact of foreground contamination (i.e. the scatter at $z=0.8$ is dominated by a small subset of clusters that have their redshift greatly underestimated).

7.4. Velocity Dispersions and X-ray Temperatures

Estimating cluster masses from the survey data is more challenging than estimating redshifts. To develop a proxy for mass that can be measured directly from the survey data, we utilize survey quality drift-scan images of known, X-ray luminous galaxy clusters at $z > 0.35$. As discussed in detail by Gonzalez (2000) and shown in Figure 19, we find Σ_{cor} is strongly correlated with velocity dispersion (linear correlation coefficient $r=0.82$), X-ray temperature, and X-ray luminosity. A fit to the σ - Σ_{cor} data yields

$$\log \sigma = (2.65 \pm 0.06) + (1.35 \pm 0.26) \log \left[\frac{\Sigma_{cor}(1+z)^\eta}{10^{-2}(1+.5)^\eta} \right] \quad (10)$$

with $\eta = 5.1^{+0.39}_{-0.49}$ for $\Omega_0=0.3$ and $\Lambda = 0$.¹³ Use of the functional form $(1+z)^\eta$ for the redshift dependence is based on simulations in which we take detected low-redshift clusters, artificially move them to higher redshifts (including both evolutionary and cosmological effects), and then redetect them. We find that E+k corrections modify η relatively to pure cosmological dimming ($\eta=4$), but that the functional

¹² However, if there are systems in which the BCG is offset from the cluster core by hundreds of kpc, as suggested by Postman & Lauer (1995), we will fail to identify these BCGs. In such cases, we can expect to underestimate the redshift by $\sim 20\%$ if we instead identify a second-ranked galaxy (assuming that it is ~ 0.5 mag fainter).

¹³ To determine the best fit we minimize the absolute deviation because this approach is more robust to outliers than a least-squares fitting procedure (see e.g. Press et al. (1992)).

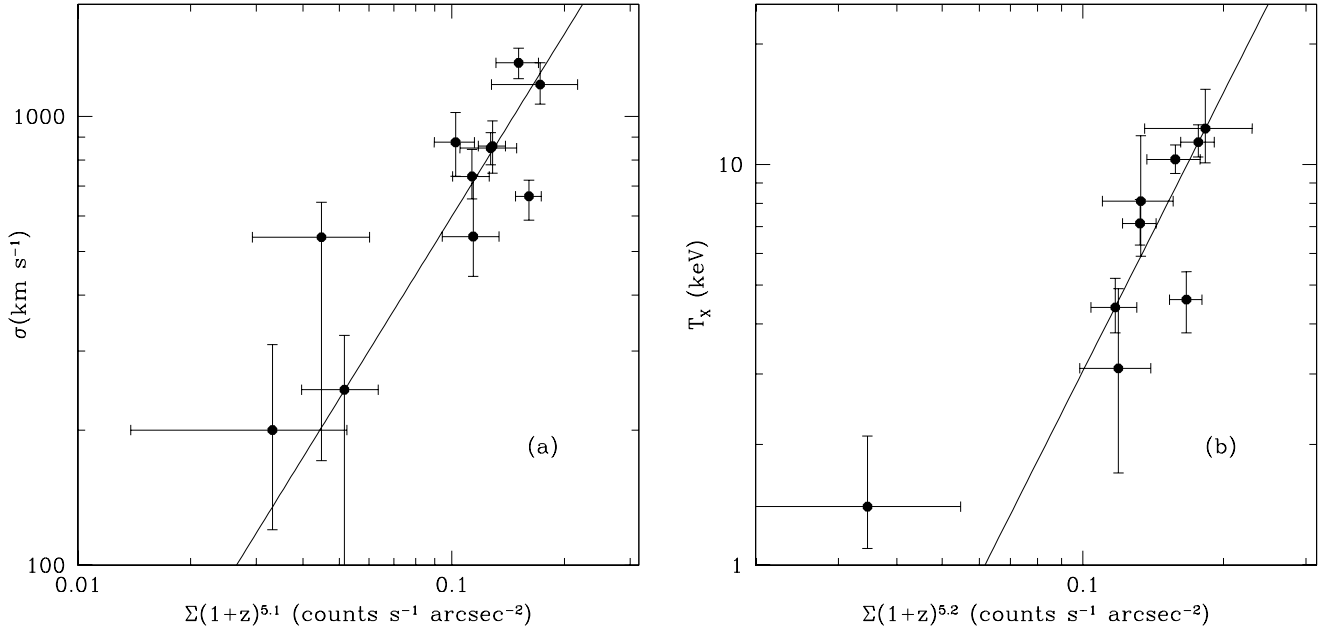


FIG. 19.— (a) Velocity dispersion, σ , as a function of optical surface brightness, Σ_{cor} . The solid line is the weighted fit from Equation 10. For the data points, Σ_{cor} has been multiplied by $(1+z)^\eta$ to eliminate its dependence upon redshift. (b) Cluster temperature, T_X , vs. Σ_{cor} . The solid line is the weighted fit from Equation 11. For both figures we caution that, due to small number statistics, the intrinsic scatter in these relations may be larger the scatter seen in our calibration sample.

form remains a good approximation (Gonzalez 2000). The T_X - Σ_{cor} data yield

$$\log T_X = (0.29^{+0.33}_{-0.20}) + (2.3 \pm 1) \log \left[\frac{\Sigma_{cor}(1+z)^\eta}{10^{-2}(1+.5)^\eta} \right] \quad (11)$$

with $\eta=5.2^{+1.05}_{-0.55}$. The parameter uncertainties for this fit are significantly larger than for the velocity dispersion data because of greater uncertainty in T_X than σ coupled with a lack of data for low-mass systems.

To test for consistency, we derive the corresponding $\sigma - T_X$ relation at $z=0.5$ and compare with the results of Xue & Wu (2000) for a larger, low-redshift sample. We find $\sigma=10^{2.48 \pm 0.19} T^{0.59 \pm 0.28}$, which is consistent with their relation, $\sigma=10^{2.51 \pm 0.01} T^{0.61 \pm 0.01}$. In Figure 20 we plot the σ and T_X corresponding to the surface brightness limit of the statistical catalog as a function of redshift for the mass range probed by our calibration sample. Because Xue & Wu (2000) note that low-mass groups may obey a different scaling relation than more massive systems, we refrain from extrapolating to lower mass. At the lowest redshifts we probe down to the level of poor groups, while by $z=0.8$ we are only able to detect very massive systems.¹⁴

Finally, one concern with this relation is that it is based upon a sample of non-LCDSCS clusters and so may not probe the range of systems seen in the LCDSCS. In particular, concern has been expressed that, due to the small size of the smoothing kernel, some of the high-redshift candidates in the LCDSCS may actually be compact groups rather than massive clusters. The LCDSCS may indeed contain some compact groups; however, it likely does not contain many of these systems. Three factors hinder their detection. First, compact groups tend to lack central,

dominant galaxies, whose halos contribute to the surface brightness signal. For example, Hickson (1982) found that half of the first-ranked galaxies in his sample were spirals. Second, compact groups have small Hubble core radii ($r_c \sim 20 h^{-1}$ kpc, Ribeiro et al. 1998), which means that at $z \gtrsim 0.5$ these groups are a factor of 3.5-4 smaller than the smoothing kernel. This filter mismatch decreases the observed surface brightness by about 25% for a Hubble profile (Figure 7). Third, while compact groups have high surface densities, much of the total luminosity is contained in the few most luminous galaxies. Removal of any of these galaxies during processing thus has a large impact upon the observed surface brightness.

8. DISCUSSION

In this paper we present the Las Campanas Distant Cluster Survey. Our primary result is a statistical catalog of 1073 cluster candidates at $z \gtrsim 0.3$ drawn from an effective area of 69 square degrees. We also include a supplementary catalog of 112 candidates that, although they fail one or more of the automated selection criteria, are strong cluster candidates. These catalogs together comprise the largest existing sample of high-redshift clusters, containing roughly three times more systems than the recently published EIS catalog (302 clusters at $0.2 \lesssim z \lesssim 1.3$). Even after accounting for an estimated contamination rate of 30%, this sample still contains more candidates at $z > 0.3$ than all existing published cluster catalogs combined. Further, we provide redshift estimates for all candidates, and also a means of estimating velocity dispersions, enabling extraction of interesting subsamples for galaxy and cluster evolution studies.

¹⁴ Of course, scatter in Σ_{cor} will lead to the inclusion of some less massive systems.

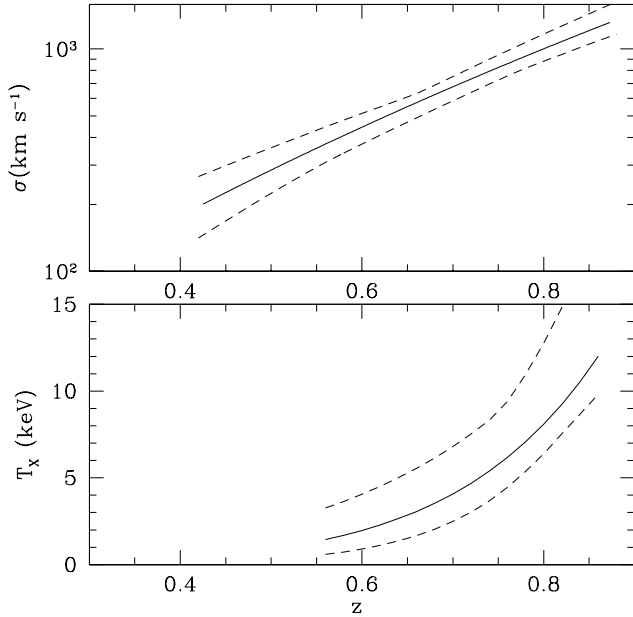


FIG. 20.— Solid lines are the limiting velocity dispersions and temperatures of the LCDCS as a function of redshift, derived from the fits given in Equations 10 and 11 with an assumed mean extinction of $E(B-V)=0.05$ for the survey. The dashed lines correspond to $1\text{-}\sigma$ uncertainties in the best fit relations. Only the σ and T_X regimes covered by the calibration data are plotted.

Finally, to a large degree this survey is an experiment in the feasibility of constructing large catalogs of clusters using surface brightness fluctuations. In the next few years, traditional optical surveys that utilize information about the individual cluster galaxies will provide catalogs of comparable size to the LCDCS (Gladders & Yee 2000), however with the deep imaging required by these surveys it is unlikely that they will provide another order of magnitude improvement beyond the LCDCS in the near future.

In contrast, drift-scan imaging of a much larger fraction of the sky will exist within the next few years. Consequently, the greatest value of this survey is perhaps not the final catalog, but rather the demonstration that this technique will work in an automated fashion with large data sets.

With this in mind, we consider modifications and improvements upon the reduction procedure and data presented in this paper that will enable construction of better, larger catalogs in the future. What are the primary problems and limitations of the LCDCS? What features would significantly improve the usefulness of this sample? The most obvious answers are greater redshift depth, greater angular area, and lower contamination – especially at the highest redshifts. Additionally, to push to higher redshift than the LCDCS, improved redshift estimates are required since at the limit of our survey foreground contamination is beginning to become a serious issue.

To achieve these improvements, several fairly straightforward tactics can be utilized. First, observing in two or more colors, while increasing the required observing time, would significantly reduce the contamination rate. Multi-color information can be used to eliminate system-related signals, and also to discriminate cluster-induced

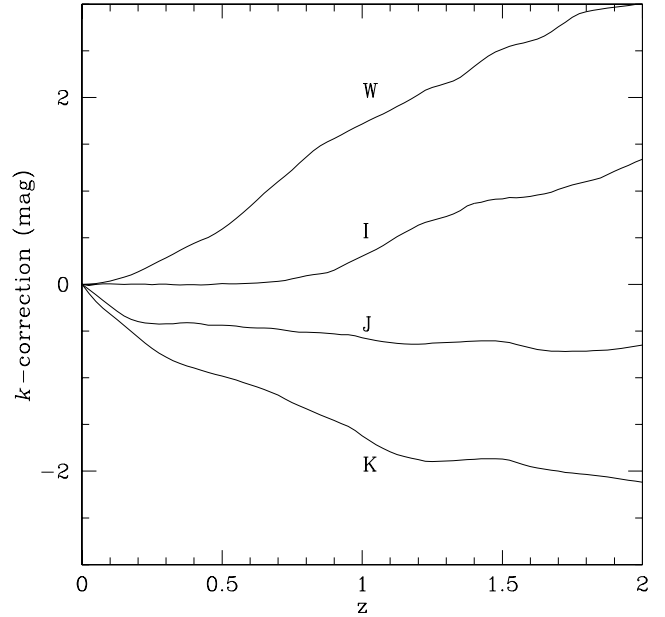


FIG. 21.— The k -correction for a passively evolving elliptical in the LCDCS W -band and several longer wavelength passbands. Curves are based upon the models of Charlot, Worthey, & Bressnan (1996).

fluctuations (which should be relatively red) from other sources such as low surface brightness galaxies and galactic cirrus. Further, color information can be used to generate improved photometric redshift estimates and, by permitting color selection of brightest cluster galaxies, minimize foreground contamination.

Improving survey depth is more challenging. While the W filter utilized in this survey was designed to maximize the incident optical flux, the k -correction for a passively evolving elliptical is large. At $z=1$ the k -correction corresponds to an effective dimming of two magnitudes relative to rest frame, and by a redshift of two the net dimming is roughly three magnitudes. To probe to higher redshift, it is necessary to shift to redder wavelengths. Figure 21 shows k -corrections for a passively evolving elliptical in several passbands. K' is the ideal choice (with J or H as the second color), as the k -correction is actually quite negative out to $z\sim 2$. A challenge with using near IR is that the sky level is very high and rapidly varying, and so additional care must be taken to avoid spurious detections. Further, unlike CCD's, near IR detectors read out individual pixel elements independently, which precludes drift scanning in the fashion employed in the LCDCS. Still, if these observational difficulties can be overcome, near IR surface brightness surveys hold the potential to identify clusters, out to $z\approx 2$.

A more conservative but more immediately feasible option is to use slightly shorter wavelength passbands, such as I and z to conduct wide-area surveys. Here the k -corrections are worse than in K' , but large-area drift-scan data are already in existence. The Sloan data set in particular is ideal for such a survey. The Sloan Survey is currently obtaining u' -, g' -, r' -, i' -, and z' -band imaging data on the Apache Point 2.5m.¹⁵ This data set should be

¹⁵ See Fukugita et al. (1996) for details on the Sloan filters.

sufficient to detect clusters out to $z \approx 1.25$.¹⁶ Using the g' , r' , and i' passbands, a contamination rate of $\lesssim 10\%$ should be possible, and BCG magnitudes can be used to generate redshift estimates with $\sigma_z \lesssim 0.10$ for all candidates (alternatively, the multiwavelength data potentially can be used to derive more precise photometric redshifts). The goal of Sloan is to image π steradians, or roughly 10,000 square degrees centered on the north galactic cap. If this entire area were analyzed using a technique similar to the one used in the LCDCS, of order 10^5 clusters and groups could be detected at $z \gtrsim 0.5$, including 5000-10000 clusters with $T_X > 5$ keV.

Several additional minor improvements should also be considered for implementation in future surveys. An adaptive filter should probably be employed for smoothing, as this will eliminate assumptions regarding the characteristic scale of clusters at high redshift. Alternatively, wavelet analysis could provide a means of eliminating these assumptions, while also improving removal of large scale, background variations. Finally, the fractional area masked can be greatly reduced if PSF models accurate to large radii are used to remove saturated stars. Unfortunately this procedure proved impractical for the LCDCS data set, but would have resulted in recovery of ~ 30 square degrees.

Detection of clusters via surface brightness fluctuations has great potential for dramatically increasing the number of known massive clusters. With this survey we have demonstrated the viability of this approach, in the process generating a catalog of over 1000 cluster candidates at $z > 0.3$. This sample is currently being used to study galaxy evolution (Nelson et al. 2001a), probe large scale structure as traced by clusters, and constrain cosmological

models via evolution in the cluster number density Gonzalez (2000). We are also working to quantify the relative detection efficiency of this and other optical algorithms with the aim of better understanding the selection biases intrinsic in each approach. Finally, it is our hope that this work will serve as the basis for larger, deeper surveys in the future that will further extend the redshift baseline and permit even more detailed study of the cluster population.

We thank Rebecca Bernstein for providing the Savitsky-Golay code employed in bias and sky subtraction and the Carnegie Observatories for their generous allocation of telescope time for this project. We also thank Marc Postman for his thorough analysis and constructive comments in refereeing this paper and Stefano Andreon for identifying a mistake in §3. AHG acknowledges support from the National Science Foundation Graduate Research Fellowship Program, the ARCS Foundation, and the Harvard-Smithsonian Center for Astrophysics. DZ acknowledges financial support from National Science Foundation CAREER grant AST-9733111, and fellowships from the David and Lucile Packard Foundation and Alfred P. Sloan Foundation. JD acknowledges support from NASA grant HF-01057.01-94A and GO-07327.01-96A. AEN acknowledges financial support from a National Science Foundation grant (AST-9733111) and the University of California Graduate Research Mentorship Fellowship program. This research has made use of the NASA/IPAC Extragalactic Database (NED) which is operated by the Jet Propulsion Laboratory, California Institute of Technology, under contract with the National Aeronautics and Space Administration.

REFERENCES

- Aragon-Salamanca, A., Ellis, R. S., Couch, Warrick J., Carter, David 1993, MNRAS, 262, 764
Aragon-Salamanca, A., Baugh, C. M., Kauffmann, G. 1998, MNRAS, 297, 427
Bertin, E., & Arnouts, S. 1996, A&AS, 117, 393
Bruzual, A., Charlot, S. 1993, ApJ, 405, 538
Charlot, S., Worthey, G., & Bressnan, A. 1996, ApJ, 457, 625
Cheeseman et al. 1988, Proceedings of the Fifth International Conference on Machine Learning, (San Francisco: Morgan Kaufmann), 54
Collins, C. A., & Mann, R. G. 1998, MNRAS, 297, 128
Dalcanton, J. J. 1995, Ph.D. thesis
Dalcanton, J. J. 1996, ApJ, 466, 92
Davies, J. I., Disney, M. J., Philipps, S., Boyle, B. J., & Couch, W. J. 1994, MNRAS, 269, 349
David, L. P., Slyz, A., Jones, C., Forman, W., Vrtilik, S. D., & Arnaud, K. A. 1993, ApJ, 412, 479
Fukugita, M., Ichikawa, T., Gunn, J. E., Doi, M., Shimasaku, K., & Schneider, D. P. 1996, AJ, 111, 1748
Gioia, I. & Luppino, G. A. 1994, ApJ, 94, 583
Gladders, M. D., & Yee, H. K. C. 2000, astroph/0004092
Goebel, J., Stutz, J., Volk, K., Walker, H., Gerbault, F., Self, M., Taylor, W., & Cheeseman, P. 1989, A&A, 222, L5
Gonzalez, A. H., Zabludoff, A. I., Zaritsky, D., Dalcanton, J. J. 2000, ApJ, 536, 561
Gonzalez, A. H. 2000, Ph. D. Thesis
Gordon, A. D. 1981, Classification, (New York: Chapman and Hall Ltd)
Guhaathakurta, P., & Tyson, J. A. 1989, ApJ, 346, 773
Henry, J. P., Gioia, I. M., Maccacaro, T., Morris, S. L., Stocke, J. T., & Wolter, A. 1992, ApJ, 386, 408
Hickson, P. 1982, ApJ, 255, 382
Holden, B. P., Romer, A. K., Nichol, R. C., & Ulmer, M. P. 1997, AJ, 114, 1701
Hudson, M. J., & Ebeling, H. 1997, ApJ, 479, 621
Humason, M. L., Mayall, N. U., & Sandage, A. R. 1956, AJ, 61, 97
Jain, A. K., & Dubes, R. C. 1988, Algorithms for Clustering Data, (Englewood Cliffs, NJ: Prentice-Hall, Inc.)
Kawasaki, W., Shimasaku, K., Doi, M., & Okamura, S. 1998, ApJS, 130, 567
Kepner, J., Fan, X., Bahcall, N., Gunn, J., Lupton, R., & Xu, G. 1998, ApJ, 517, 78
Kim, R. S. J. et al. 2000, in Clustering at High Redshift, ed. Mazure, A., Le Fèvre, O., & Le Brun, V., ASP, 200, 422
Landolt, A. U. 1992, AJ, 104, 340
Lidman, C. E., & Peterson, B. A. 1996, AJ, 112, 2454
McGlynn, T., Scollick, K., White, N., SkyView: The Multi-Wavelength Sky on the Internet, McLean, B.J. et al., New Horizons from Multi-Wavelength Sky Surveys, Kluwer Academic Publishers, 1996, IAU Symposium No. 179, 465
McNally, D. 1974, Positional Astronomy, (New York: John Wiley & Sons)
Nelson, A. E., Gonzalez, A. H., Zaritsky, D. Z., & Dalcanton, J. J. 2001, submitted to ApJ
Nelson, A. E., Gonzalez, A. H., Zaritsky, D. Z., & Dalcanton 2001, in preparation
Oke et al. 1995, PASP, 107, 375
Olsen, L. F. et al. 1999, A&A, 345, 681
Philipps, S., & Davies, J. 1991, MNRAS, 251, 105
Postman, M., & Lauer, T. R. 1995, ApJ, 440, 28
Postman, M., Lubin, L. M., Gunn, J. E., Oke, J. B., Hoessel, J. G., Schneider, D. P., & Christensen, J. A. 1996, AJ, 111, 615
Press, W. H., Teukolsky, S. A., Vetterling, W. T., Flannery, B. P. 1992, Numerical Recipes, (2d ed.; New York: Cambridge University Press)
Ribeiro, A. L. B., de Carvalho, R. R., Capelato, H. V., & Zepf, S. E. 1998, ApJ, 497, 72
Sandage, A. 1972a, ApJ, 173, 485
Sandage, A. 1972b, ApJ, 178, 1
Sandage, A. 1988, ARA&A, 26, 561

¹⁶ For expected limiting magnitudes, see http://www.sdss.org/science/tech_summary.html.

- Scheick, X. & Kuhn, J. R. 1994, *ApJ*, 423, 566
 Schindler, S. et al. 1995, *A&A*, 299, L9
 Schlegel, D. J., Finkbeiner, D. P., & Davis, M. 1998, *ApJ*, 500, 525
 Scodreggio et al. 1999, *A&AS*, 137, 83
 Szomoru, A., & Guhathakurta, P. 1998, *ApJ*, 494, 93
 Uson, J. M., Bough, S. P., & Kuhn, J. R. 1990, *Science*, 250, 539
 Uson, J. M., Bough, S. P., & Kuhn, J. R. 1991, *ApJ*, 369, 46
 Vikhlinin, A., McNamara, B. R., Forman, W., Jones, C., Quintana, H., & Hornstrup, A. 1998, *ApJ*, 502, 558
 White, S. D. M., Efstathiou, G., & Frenk, C. S. 1993, *MNRAS*, 262, 1023
 Xue, Y. & Wu, X. 2000, *ApJ*, 538, 65
 Zaritsky, D., Nelson, A. E., Dalcanton, J. J., & Gonzalez, A. H. 1997, *ApJ*, 480, L91
 Zaritsky, D., Schectman, S. A., Bredthauer, G. 1996, *PASP*, 108, 104

APPENDIX

PROJECTION EFFECTS AND ASTROMETRIC ALIGNMENT

To accurately align the drift scans and generate mosaics in which objects are aligned to $\delta\theta \lesssim 1''$ over the entire length of the scans, two issues must be addressed. First, we must account for geometrical projection effects. Failure to correct for projection effects leads to a maximal alignment error of $2''$ in declination. Second, and more importantly, we must transform data taken along arbitrary Great Circles to a common coordinate system before alignment is possible. This is particularly critical because a subset of the data was taken along lines of constant right ascension due to mechanical difficulties with the Great Circle Camera (GCC), and so in some cases it is necessary to align scans of this type with Great Circle scans. In these cases, failure to transform the GCC scans would result in alignment errors of several arcminutes at the ends of the scans. For extensive information on projection effects, astrometric alignment, and related topics, we refer the reader to McNally (1974).

Projection effects are typically a two-dimensional issue; however, the problem is simplified with drift scan data. Let us define an angular coordinate system (τ, β) , where τ represents the longitudinal angle along the Great Circle traced by the GCC, and β is the declination relation to this circle. Further, define the projected cartesian coordinate system (x, y) , with x being the direction perpendicular to the direction of the scan. For a pointed observation, the standard gnomonic formulae are

$$x = \beta_0 + \frac{\tan \beta \cos \beta_0 - \sin \beta_0 \cos(\tau - \tau_0)}{\tan \beta \sin \beta_0 + \cos \beta_0 \cos(\tau - \tau_0)}, \quad (\text{A1})$$

and,

$$y = \tau_0 + \frac{\sin(\tau - \tau_0)}{\tan \beta \sin \beta_0 + \cos \beta_0 \cos(\tau - \tau_0)}, \quad (\text{A2})$$

where (τ_0, β_0) are the coordinates of the center of the image. With a drift scan the situation is slightly different. Along the direction of the scan, projection effects are washed out because a given position on the sky is observed over the full range of the detector. To see this mathematically, consider equation A2. Since we are now averaging over a range of τ , we should integrate over the second term. Further, since all values of τ are equivalent there is no longer a central τ_0 and so the appropriate equation for y is

$$y = \tau + \int_{\tau-\Delta\tau}^{\tau+\Delta\tau} \frac{\sin(\tau' - \tau)}{\tan \beta \sin \beta_0 + \cos \beta_0 \cos(\tau' - \tau)} d\tau'. \quad (\text{A3})$$

(see Figure A22). Since the centerline of the scan lies along the Great Circle traced by the scan, $\beta_0 = 0$, which simplifies this last equation to

$$y = \tau + \int_{\tau-\Delta\tau}^{\tau+\Delta\tau} \tan(\tau' - \tau) d\tau' = \tau, \quad (\text{A4})$$

with the second term disappearing because we are integrating over an odd function. For x , there is no such averaging effect. Still, we can simplify the projection equation. We have already stated that $\beta_0 = 0$. We now also note that for a drift scan the gnomonic projection in x is independent of τ , and so set $\tau_0 = \tau$ in equation A1. Thus, the equation for x simplifies to

$$x = 0 + \frac{\tan \beta \cos 0 - \sin 0 \cos 0}{\tan \beta \sin 0 + \cos 0 \cos 0} = \tan \beta, \quad (\text{A5})$$

and so the equations of projection for a drift scan along a Great Circle are

$$y = \tau, \quad (\text{A6})$$

$$x = \tan \beta. \quad (\text{A7})$$

The above equations adequately describe the gnomonic distortion of the images, but we are still in a coordinate system based upon the Great Circle along which the scan was taken. Next, it is necessary to transform these coordinates to equatorial right ascension and declination (α, δ) . We once again refer the reader to McNally (1974) for a more thorough treatment of spherical coordinate transformations. Define (α_G, δ_G) to be the coordinates of the northern pole of the GCC system in equatorial coordinates, (α_0, δ_0) to be the equatorial coordinates of the center of the scan, and (τ_P, β_P) to be

the Great Circle coordinates of the northern pole of the equatorial system. The coordinates of the pole and scan center are related as

$$(\alpha_G, \beta_G) = \begin{cases} (\alpha_0 + 180, 90 - \delta_0) & \text{if } \alpha_0 < 180, \\ (\alpha_0 - 180, 90 - \delta_0) & \text{if } \alpha_0 > 180. \end{cases} \quad (\text{A8})$$

With these definitions, application of spherical trigonometry leads to the relations

$$\sin \delta = \sin \delta_G \sin \beta + \cos \delta_G \cos \beta \cos(\tau_P - \tau), \quad \textbf{Cosine Law} \quad (\text{A9})$$

$$\cos \delta \sin(\alpha - \alpha_G) = \cos \beta \sin(\tau_P - \tau), \quad \textbf{Sine Law} \quad (\text{A10})$$

and

$$\cos \delta \cos(\alpha - \alpha_G) = \sin \beta \cos \delta_G - \cos \beta \sin \delta_G \cos(\tau_P - \tau). \quad \textbf{Analog Formula} \quad (\text{A11})$$

It is these three equations that we use to transform the survey data. Note that although we have three equations relating the coordinates, these do not over-constrain the problem. The third equation is required to remove sign ambiguities. Subsequent to these transformations, the cartesian coordinates of the survey correspond to a 1-to-1 linear map of right ascension and declination, with a plate scale of $0''.7 \text{ pixel}^{-1}$.

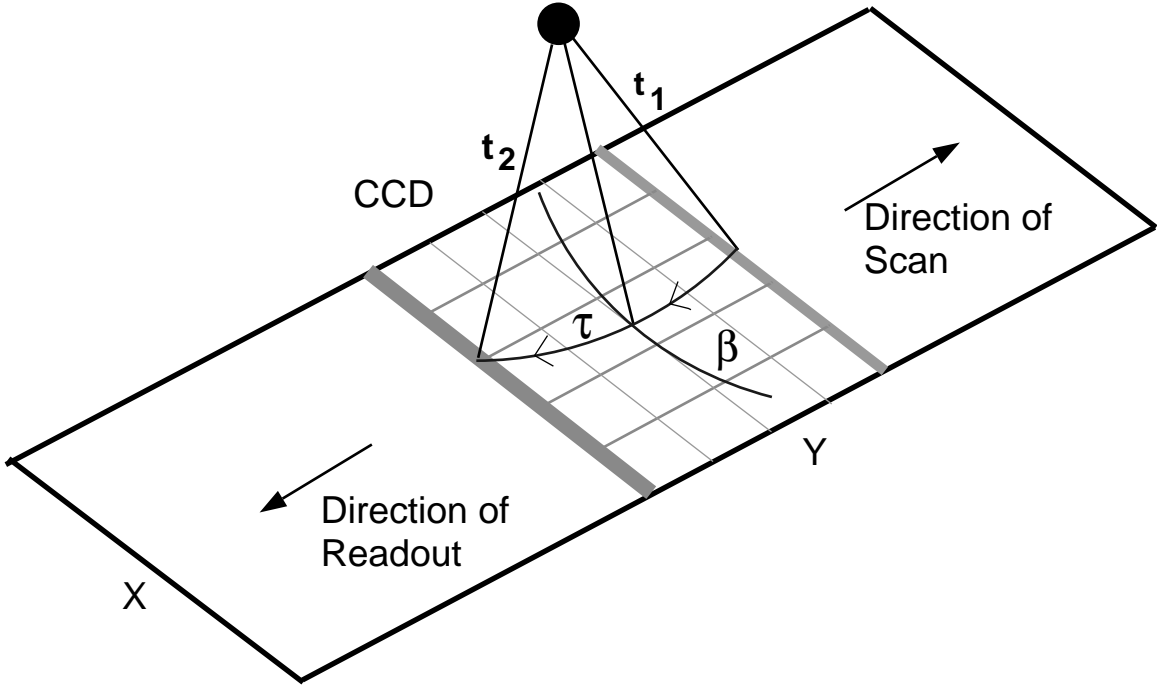


FIG. A22.— Illustration of projection effects for drift scanning. Projection effects are washed out along the direction of readout as the signal is averaged across the entire ccd (with time increasing from t_1 to t_2). Perpendicular to the readout, projection of β onto x must be corrected.

TABLE 1
STATISTICAL CATALOG

ID	α (J2000)			δ (J2000)			z_{est}	Σ_{obs}	Σ_{cor}	E($B-V$)	Notes
	h	m	s	°	'	''					
0001	10	01	07.4	-12	26	24	0.80	6.46	7.84	0.070	
0002	10	02	01.5	-12	45	35	0.43	6.79	8.05	0.062	$z_{K_{eck}}=0.52$
0003	10	02	17.8	-12	23	15	0.37	6.38	7.82	0.074	
0004	10	02	17.9	-12	50	10	0.59	7.25	8.62	0.062	
0005	10	02	27.1	-12	47	13	0.57	7.62	9.17	0.067	
0006	10	02	39.3	-11	39	32	0.41	6.41	7.81	0.071	
0007	10	02	43.6	-11	35	16	0.50	7.06	8.66	0.074	
0008	10	02	46.6	-12	38	42	>0.85	6.57	8.00	0.071	
0009	10	02	50.1	-12	36	08	0.67	6.67	8.16	0.073	
0010	10	03	16.1	-12	02	43	0.33	7.97	9.45	0.062	
0011	10	03	28.5	-11	31	34	0.49	6.94	8.74	0.084	
0012	10	03	58.6	-12	18	48	0.76	6.71	8.01	0.064	
0013	10	04	31.1	-11	37	23	0.56	7.26	9.03	0.079	
0014	10	04	49.1	-11	39	30	>0.85	6.60	8.21	0.079	
0015	10	05	24.2	-12	23	04	0.49	6.35	7.34	0.053	
0016	10	05	28.0	-11	51	50	0.72	6.63	7.83	0.060	
0017	10	05	43.6	-11	47	43	0.53	8.49	10.10	0.063	
0018	10	05	58.2	-11	47	43	0.62	7.19	8.56	0.063	
0019	10	06	00.2	-12	50	03	0.50	6.92	8.08	0.056	
0020	10	06	20.3	-12	50	35	0.57	7.85	9.22	0.058	
0021	10	06	22.9	-11	39	18	0.52	7.80	9.15	0.058	
0022	10	06	24.4	-12	40	51	0.75	7.51	8.75	0.055	
0023	10	06	36.2	-12	40	29	0.36	7.26	8.50	0.057	
0024	10	06	39.5	-11	53	47	0.36	6.34	7.46	0.059	
0025	10	07	07.2	-11	58	26	0.35	7.28	8.49	0.056	
0026	10	07	42.6	-12	08	36	0.41	7.28	8.43	0.053	
0027	10	07	54.7	-12	21	19	0.52	9.00	10.50	0.056	
0028	10	10	15.1	-11	36	27	0.48	6.90	7.95	0.051	
0029	10	10	59.4	-11	40	03	0.39	10.10	11.90	0.058	
0030	10	11	01.3	-11	40	54	0.40	7.79	9.15	0.058	
0031	10	12	43.3	-12	48	43	0.62	7.28	8.88	0.071	
0032	10	12	53.5	-11	30	02	0.34	9.35	11.00	0.060	
0033	10	12	58.5	-12	35	15	0.40	6.91	8.33	0.068	
0034	10	13	17.0	-11	39	21	0.36	6.25	7.43	0.062	
0035	10	14	43.7	-12	09	28	0.44	8.87	10.80	0.070	
0036	10	14	49.2	-11	40	59	0.59	7.83	9.45	0.068	
0037	10	14	50.4	-12	22	19	0.58	6.80	8.21	0.068	
0038	10	15	17.4	-12	07	11	0.46	7.47	9.11	0.072	
0039	10	15	24.6	-12	39	00	0.73	7.28	8.89	0.072	
0040	10	15	26.8	-12	42	26	0.75	6.48	7.94	0.073	
0041	10	15	37.6	-11	43	19	0.34	7.55	9.18	0.071	
0042	10	16	09.7	-12	49	42	0.82	6.43	7.99	0.079	
0043	10	16	16.2	-12	38	03	>0.85	9.33	11.50	0.075	
0044	10	16	19.2	-12	45	17	0.62	7.03	8.70	0.078	
0045	10	16	31.2	-12	46	16	0.61	6.41	7.96	0.078	
0046	10	16	32.4	-12	51	06	0.73	7.44	9.28	0.080	
0047	10	16	51.0	-12	47	29	0.59	7.03	8.76	0.079	
0048	10	16	58.0	-12	41	01	0.34	6.98	8.64	0.077	
0049	10	17	07.7	-12	50	09	0.34	9.04	11.30	0.081	
0050	10	17	08.9	-12	41	35	0.48	6.73	8.35	0.078	
0051	10	17	20.7	-12	32	19	0.34	10.50	13.00	0.078	
0052	10	18	16.4	-12	30	06	0.50	7.03	8.82	0.082	

TABLE 1—*Continued*

ID	α (J2000)			δ (J2000)			z_{est}	Σ_{obs}	Σ_{cor}	E(B-V)	Notes
	h	m	s	°	'	"					
0053	10	18	22.6	-12	53	50	0.34	9.56	12.10	0.086	
0054	10	18	27.5	-12	53	43	0.33	10.20	13.00	0.086	
0055	10	18	28.9	-12	17	48	0.46	8.04	10.10	0.081	
0056	10	18	38.3	-11	32	56	0.74	6.96	8.42	0.069	
0057	10	18	46.4	-12	11	53	0.47	8.80	11.00	0.079	
0058	10	20	19.1	-12	47	12	0.75	7.39	9.40	0.087	
0059	10	20	27.9	-12	38	02	>0.85	6.67	8.38	0.082	
0060	10	22	07.8	-12	24	36	0.46	9.32	11.40	0.072	
0061	10	22	16.8	-11	38	43	0.41	6.89	8.03	0.056	
0062	10	22	48.4	-12	16	09	0.47	6.58	7.83	0.063	
0063	10	22	53.0	-12	50	35	0.62	6.54	8.30	0.086	
0064	10	23	22.1	-12	21	52	0.33	6.54	7.83	0.065	
0065	10	23	59.3	-11	45	24	0.39	6.97	8.02	0.051	
0066	10	24	17.4	-11	49	12	0.32	8.66	9.97	0.051	
0067	10	24	23.8	-11	56	55	0.73	6.26	7.24	0.053	
0068	10	24	42.9	-12	45	53	>0.85	6.39	8.06	0.084	
0069	10	24	45.4	-12	46	05	0.51	6.32	7.97	0.084	
0070	10	25	00.2	-12	26	39	0.41	11.60	14.10	0.071	
0071	10	25	08.8	-12	36	20	0.34	13.80	17.10	0.077	
0072	10	25	31.8	-12	01	47	0.41	7.52	8.73	0.054	
0073	10	25	56.8	-11	49	01	0.47	7.33	8.38	0.048	
0074	10	26	04.7	-12	45	53	0.39	7.66	9.50	0.078	
0075	10	26	50.9	-11	39	59	0.48	10.00	11.40	0.048	
0076	10	27	26.3	-11	59	34	0.37	10.80	12.60	0.055	
0077	10	28	21.6	-12	46	23	0.40	7.87	9.75	0.078	
0078	10	28	23.6	-12	03	40	0.33	8.04	9.45	0.058	
0079	10	28	26.2	-12	54	53	0.52	6.27	7.76	0.077	
0080	10	28	27.0	-12	01	51	0.42	10.80	12.70	0.058	
0081	10	28	39.7	-12	41	15	0.34	7.26	9.05	0.080	
0082	10	29	15.1	-12	53	44	>0.85	6.29	7.66	0.071	
0083	10	29	22.8	-12	39	37	0.40	6.30	7.83	0.079	
0084	10	29	39.1	-12	31	08	0.49	6.43	7.81	0.070	
0085	10	29	40.7	-11	48	51	0.68	6.56	7.64	0.055	
0086	10	29	50.2	-11	49	11	0.49	6.44	7.49	0.054	
0087	10	30	10.7	-12	21	27	0.40	7.76	9.22	0.063	
0088	10	30	22.8	-12	31	47	0.82	7.26	8.67	0.064	
0089	10	30	53.4	-11	57	46	0.42	6.72	7.76	0.052	
0090	10	31	35.0	-12	03	43	0.75	7.03	8.06	0.049	
0091	10	31	50.3	-12	44	27	0.69	8.44	10.10	0.064	
0092	10	31	55.5	-12	39	51	0.70	6.59	7.78	0.060	
0093	10	31	57.8	-11	30	43	0.55	8.01	9.05	0.044	
0094	10	32	04.9	-12	29	44	0.45	8.08	9.44	0.056	
0095	10	32	09.8	-12	43	59	0.68	7.25	8.50	0.058	
0096	10	33	14.0	-12	50	40	0.67	6.40	7.46	0.055	
0097	10	34	12.4	-12	19	43	0.43	6.54	7.68	0.058	
0098	10	34	38.8	-12	20	37	>0.85	6.26	7.38	0.059	Tidal Tail
0099	10	34	40.1	-11	30	03	>0.85	6.47	7.27	0.042	Tidal Tail
0100	10	34	54.6	-12	44	05	0.55	7.35	8.53	0.054	
0101	10	35	35.2	-12	18	18	0.37	7.39	8.63	0.056	
0102	10	35	39.8	-11	42	15	0.31	9.70	10.90	0.041	
0103	10	36	06.5	-12	00	34	0.30	7.46	8.64	0.053	
0104	10	36	10.4	-12	44	43	0.55	7.82	9.03	0.052	

TABLE 1—*Continued*

ID	α (J2000)			δ (J2000)			z_{est}	Σ_{obs}	Σ_{cor}	E(B-V)	Notes
	h	m	s	°	'	''					
0105	10	36	24.7	-12	57	17	0.77	6.87	7.90	0.051	
0106	10	36	25.5	-12	36	30	0.75	6.56	7.58	0.052	
0107	10	36	40.7	-11	45	24	0.52	6.90	7.71	0.040	
0108	10	36	44.9	-11	36	47	0.43	9.61	10.80	0.041	
0109	10	37	44.9	-12	45	57	0.44	7.40	8.45	0.048	
0110	10	37	52.6	-12	43	44	0.78	9.39	10.70	0.048	
0111	10	38	00.0	-12	18	54	0.66	7.95	9.45	0.063	
0112	10	38	00.7	-12	25	08	0.37	12.60	14.90	0.060	
0113	10	38	08.3	-12	23	22	0.31	7.70	9.11	0.061	
0114	10	38	19.8	-12	13	34	0.35	8.47	9.97	0.059	
0115	10	38	21.1	-11	45	42	0.40	6.39	7.31	0.049	
0116	10	38	21.6	-12	36	52	0.40	6.59	7.61	0.052	
0117	10	38	41.7	-12	07	44	0.41	7.16	8.20	0.049	
0118	10	38	47.1	-11	46	58	0.31	8.26	9.43	0.048	
0119	10	39	16.3	-12	35	52	0.51	6.75	7.70	0.047	
0120	10	39	16.8	-12	12	21	0.53	7.39	8.54	0.052	
0121	10	39	21.7	-12	44	48	0.75	6.58	7.49	0.047	
0122	10	39	32.7	-11	31	37	0.57	7.06	8.37	0.062	
0123	10	39	44.9	-11	54	12	0.31	11.20	12.70	0.046	
0124	10	39	59.2	-11	37	21	0.44	7.78	9.18	0.060	
0125	10	40	10.2	-11	40	29	0.68	7.21	8.49	0.059	
0126	10	40	11.3	-12	18	60	0.47	8.33	9.64	0.053	
0127	10	40	27.3	-11	55	46	0.38	8.20	9.54	0.055	
0128	10	40	28.3	-12	56	09	0.52	6.98	7.89	0.044	
0129	10	40	33.5	-12	01	01	0.71	6.32	7.27	0.051	
0130	10	40	41.6	-11	55	51	0.80	9.49	11.10	0.057	
0131	10	41	04.7	-12	18	28	0.52	7.27	8.34	0.050	
0132	10	41	18.6	-11	46	02	0.51	7.10	8.41	0.061	
0133	10	42	03.3	-11	49	28	0.76	6.46	7.60	0.059	
0134	10	43	17.7	-12	32	54	0.40	7.26	8.31	0.049	
0135	10	43	40.1	-11	55	60	0.53	6.86	7.95	0.053	
0136	10	43	55.0	-12	20	38	>0.85	6.65	7.73	0.055	
0137	10	43	58.3	-11	42	50	0.34	6.72	7.45	0.037	
0138	10	44	15.8	-11	36	56	0.84	6.91	7.56	0.032	
0139	10	45	00.1	-12	02	50	0.68	6.77	7.62	0.043	
0140	10	45	11.2	-12	18	15	0.75	7.02	8.00	0.048	
0141	10	45	15.3	-12	50	24	0.71	6.95	8.18	0.059	
0142	10	45	18.6	-11	58	43	0.35	11.60	12.80	0.035	
0143	10	46	05.8	-11	35	36	0.57	6.60	7.25	0.034	
0144	10	46	06.6	-12	34	24	0.31	9.36	10.80	0.052	
0145	10	46	08.5	-12	53	28	0.33	8.59	10.20	0.063	
0146	10	46	19.5	-12	28	24	0.44	6.74	7.65	0.046	
0147	10	46	35.9	-12	59	22	0.36	9.28	11.20	0.068	
0148	10	46	55.4	-11	40	36	0.45	6.69	7.35	0.034	
0149	10	47	00.6	-12	56	31	0.32	9.81	11.60	0.061	
0150	10	47	13.4	-12	40	14	0.73	6.77	7.94	0.058	
0151	10	47	28.8	-12	06	00	0.44	6.76	7.37	0.031	
0152	10	47	51.9	-11	56	15	0.47	7.07	7.77	0.034	
0153	10	48	47.2	-11	58	03	0.38	6.96	7.71	0.037	
0154	10	48	50.6	-11	53	48	0.38	6.76	7.53	0.039	
0155	10	48	52.4	-12	23	09	0.35	9.81	11.00	0.040	
0156	10	50	07.0	-11	57	54	0.35	7.99	9.04	0.045	

TABLE 1—*Continued*

ID	$\alpha(\text{J2000})$			$\delta(\text{J2000})$			z_{est}	Σ_{obs}	Σ_{cor}	$E(B-V)$	Notes
	h	m	s	°	'	''					
0157	10	50	25.7	-12	59	40	0.57	6.42	7.54	0.059	LSB
0158	10	50	28.0	-12	40	01	0.35	6.68	7.57	0.046	
0159	10	50	31.6	-12	46	47	0.67	7.17	8.20	0.048	
0160	10	50	39.7	-11	59	35	0.69	6.38	7.25	0.046	
0161	10	50	49.8	-12	41	34	0.37	7.53	8.59	0.048	
0162	10	51	22.6	-11	36	11	0.71	6.78	7.68	0.045	
0163	10	51	22.7	-12	01	27	0.67	10.80	12.30	0.045	
0164	10	51	31.2	-12	55	29	0.67	6.43	7.36	0.049	Merged galaxy detections
0165	10	52	08.4	-12	40	42	0.48	6.29	7.21	0.050	
0166	10	52	31.8	-12	33	36	0.62	7.70	8.77	0.047	
0167	10	52	33.7	-11	34	12	0.37	10.80	12.00	0.039	
0168	10	52	56.1	-11	51	31	0.83	6.65	7.47	0.042	
0169	10	52	56.7	-11	31	20	0.39	9.45	10.50	0.038	
0170	10	53	22.6	-12	52	26	0.76	7.82	8.88	0.046	
0171	10	53	46.8	-11	38	38	0.44	6.72	7.37	0.033	
0172	10	54	24.2	-11	46	18	0.76	7.61	8.31	0.032	
0173	10	54	43.5	-12	45	50	0.83	8.34	9.36	0.042	
0174	10	54	56.4	-12	25	23	0.36	8.62	9.73	0.044	
0175	10	55	04.0	-12	40	14	0.80	6.29	7.07	0.042	
0176	10	55	17.4	-11	44	45	0.43	6.58	7.20	0.032	
0177	10	55	47.4	-12	52	36	0.76	7.70	8.69	0.044	
0178	10	56	23.4	-11	55	13	0.46	6.48	7.18	0.037	
0179	10	57	07.2	-12	24	02	0.73	6.52	7.24	0.038	
0180	10	57	11.3	-12	33	03	0.41	6.44	7.14	0.037	
0181	10	57	28.1	-12	18	19	0.55	6.71	7.44	0.038	
0182	10	57	44.7	-12	15	49	0.30	6.46	7.09	0.034	
0183	10	58	00.4	-12	10	44	0.32	8.75	9.53	0.031	
0184	10	58	12.6	-11	56	34	0.81	6.71	7.25	0.028	
0185	10	58	34.9	-12	11	09	0.37	7.18	7.73	0.027	
0186	10	58	37.9	-12	05	35	0.83	6.53	7.05	0.028	
0187	10	58	38.9	-11	41	27	0.63	7.47	8.10	0.029	
0188	10	59	09.5	-12	53	15	0.52	8.44	9.20	0.031	
0189	10	59	12.8	-12	56	51	0.41	7.61	8.31	0.032	
0190	10	59	23.4	-12	53	19	0.60	6.29	6.85	0.031	
0191	10	59	50.5	-11	57	09	0.48	7.85	8.55	0.031	
0192	11	00	23.9	-12	27	46	0.41	7.10	7.71	0.030	
0193	11	00	39.0	-12	21	49	0.36	7.55	8.19	0.029	
0194	11	01	13.9	-12	12	17	0.45	7.95	8.66	0.031	
0195	11	02	37.2	-12	34	14	0.32	8.67	9.66	0.039	
0196	11	03	00.3	-12	40	36	0.48	9.10	10.20	0.041	
0197	11	03	24.4	-11	37	31	0.43	7.20	8.08	0.042	
0198	11	03	42.9	-12	45	18	0.83	7.98	8.79	0.035	
0199	11	04	33.0	-12	18	42	0.31	12.00	13.50	0.042	
0200	11	05	37.5	-12	54	34	0.43	8.25	9.36	0.045	
0201	11	05	49.8	-11	53	16	0.41	8.20	9.33	0.047	
0202	11	05	55.7	-12	52	48	>0.85	6.70	7.64	0.048	
0203	11	06	08.3	-11	58	58	0.31	6.82	7.67	0.042	
0204	11	07	05.5	-12	50	57	0.46	6.59	7.76	0.059	
0205	11	07	08.5	-11	32	18	0.58	7.00	8.05	0.051	
0206	11	07	59.3	-12	16	31	0.66	8.42	9.68	0.050	
0207	11	08	09.2	-11	33	59	0.37	7.73	8.93	0.052	

TABLE 1—*Continued*

ID	α (J2000)			δ (J2000)			z_{est}	Σ_{obs}	Σ_{cor}	E(B-V)	Notes
	h	m	s	°	'	"					
0208	11	08	23.4	-11	52	53	0.44	6.52	7.56	0.053	
0209	11	08	29.6	-11	30	23	0.33	14.30	16.60	0.055	
0210	11	09	50.1	-12	39	51	0.46	6.59	7.58	0.051	
0211	11	10	19.8	-11	59	04	0.46	9.19	11.10	0.068	
0212	11	10	26.0	-12	05	41	0.76	6.26	7.57	0.068	
0213	11	10	34.8	-12	38	38	0.33	8.06	9.27	0.051	
0214	11	10	38.3	-12	17	13	0.43	7.67	9.10	0.062	
0215	11	10	46.7	-12	04	16	0.77	7.95	9.90	0.080	
0216	11	10	53.2	-12	16	50	0.41	8.78	10.70	0.071	
0217	11	13	00.6	-12	01	35	0.47	8.50	9.78	0.051	
0218	11	13	09.4	-11	48	15	0.76	6.34	7.26	0.049	
0219	11	13	18.2	-12	09	29	0.40	8.66	9.93	0.050	
0220	11	13	36.2	-11	58	17	0.42	7.49	8.59	0.050	
0221	11	13	40.7	-12	48	16	0.53	6.83	8.06	0.060	
0222	11	13	44.0	-12	27	16	0.76	6.72	7.81	0.055	
0223	11	13	54.2	-11	56	17	0.40	6.25	7.16	0.049	
0224	11	13	56.9	-12	20	58	0.42	8.27	9.66	0.056	
0225	11	14	01.9	-11	47	32	0.32	8.24	9.44	0.049	
0226	11	14	02.2	-11	57	44	0.54	7.39	8.49	0.050	
0227	11	14	08.8	-11	35	52	0.38	8.20	9.54	0.055	
0228	11	14	13.5	-12	01	15	0.39	9.20	10.70	0.054	
0229	11	14	43.1	-11	56	06	0.36	7.74	8.93	0.051	
0230	11	14	50.5	-12	52	10	0.69	7.64	9.81	0.091	
0231	11	15	40.1	-12	57	50	0.67	6.38	7.96	0.080	
0232	11	15	40.2	-12	56	33	>0.85	6.56	8.17	0.080	
0233	11	15	47.1	-12	23	43	0.46	9.73	11.50	0.062	Possible LSB
0234	11	16	03.3	-12	16	59	0.44	6.84	8.06	0.059	
0235	11	16	25.2	-11	50	44	0.40	6.97	8.31	0.063	
0236	11	16	37.6	-12	22	08	0.41	9.09	10.90	0.067	
0237	11	16	59.8	-11	51	02	0.78	7.50	8.99	0.066	
0238	11	17	15.6	-12	53	27	0.39	9.18	10.80	0.059	
0239	11	17	20.1	-12	02	27	0.79	6.42	7.53	0.058	
0240	11	17	22.0	-11	55	46	0.79	9.05	10.90	0.066	
0241	11	17	24.5	-12	05	09	0.72	6.59	7.70	0.057	
0242	11	17	35.7	-12	42	49	0.34	6.60	7.86	0.063	
0243	11	17	37.4	-11	53	11	0.32	11.30	13.70	0.069	
0244	11	17	43.2	-11	31	44	0.53	6.26	7.74	0.077	
0245	11	18	04.0	-12	44	28	0.40	6.84	7.97	0.055	
0246	11	18	20.0	-12	25	16	0.39	10.60	12.50	0.060	
0247	11	18	24.0	-12	40	51	0.71	7.61	8.85	0.054	
0248	11	18	36.2	-12	02	03	0.60	8.53	10.20	0.066	
0249	11	18	51.9	-12	45	39	0.60	6.67	7.74	0.054	
0250	11	18	57.6	-11	31	22	0.39	9.11	10.90	0.064	
0251	11	19	07.5	-12	54	57	0.64	6.55	7.72	0.060	
0252	11	19	16.5	-11	29	33	0.63	7.62	9.01	0.061	
0253	11	19	27.5	-12	29	43	0.35	12.20	14.20	0.056	
0254	11	19	39.3	-12	41	37	0.79	6.33	7.36	0.054	
0255	11	19	44.3	-11	52	32	0.35	10.60	12.80	0.066	
0256	11	19	46.5	-12	09	35	0.55	7.53	8.85	0.058	
0257	11	19	54.6	-12	02	24	0.40	9.60	11.40	0.063	
0258	11	19	55.2	-12	02	26	0.47	12.40	14.80	0.063	
0259	11	20	07.2	-12	05	04	0.49	13.90	16.40	0.061	

TABLE 1—*Continued*

ID	α (J2000)			δ (J2000)			z_{est}	Σ_{obs}	Σ_{cor}	E(B-V)	Notes
	h	m	s	°	'	''					
0260	11	20	13.3	-11	58	52	0.38	13.90	16.60	0.065	
0261	11	20	17.5	-12	51	30	0.77	6.74	7.83	0.054	
0262	11	20	19.8	-11	46	06	0.60	6.56	7.88	0.067	
0263	11	20	21.1	-12	31	51	>0.85	7.02	8.28	0.060	
0264	11	20	21.7	-12	01	45	0.42	19.40	23.00	0.063	
0265	11	20	29.8	-11	43	25	0.52	7.53	8.97	0.063	
0266	11	20	30.4	-12	48	01	0.77	7.01	8.18	0.056	
0267	11	20	38.3	-11	46	00	0.51	7.28	8.70	0.065	
0268	11	21	11.7	-12	10	46	0.68	6.41	7.42	0.053	
0269	11	21	30.5	-11	35	55	0.73	6.40	7.73	0.068	
0270	11	22	05.8	-12	01	12	0.48	6.39	7.34	0.050	
0271	11	22	09.0	-11	39	46	0.37	6.35	7.82	0.076	
0272	11	22	35.8	-12	17	48	0.35	7.88	8.87	0.043	
0273	11	22	48.1	-12	14	37	0.53	7.16	8.05	0.042	
0274	11	22	51.0	-12	23	48	0.37	12.90	14.50	0.042	
0275	11	22	51.7	-11	36	30	0.77	8.93	11.30	0.086	
0276	11	23	15.8	-11	32	31	0.48	8.49	10.90	0.090	
0277	11	23	18.7	-12	57	59	0.56	6.39	7.03	0.035	
0278	11	23	39.1	-12	36	03	0.35	9.21	10.10	0.033	
0279	11	23	46.6	-12	20	01	0.51	8.80	10.00	0.048	
0280	11	23	59.4	-11	50	07	0.54	8.96	10.10	0.043	
0281	11	24	18.0	-11	32	59	0.37	6.64	8.05	0.070	
0282	11	24	23.5	-12	57	31	0.51	6.48	7.15	0.035	
0283	11	24	24.7	-12	40	32	0.68	7.58	8.29	0.033	
0284	11	25	03.9	-11	35	19	0.51	7.52	8.52	0.045	
0285	11	25	31.8	-12	50	33	0.35	7.49	8.19	0.032	
0286	11	25	47.2	-11	47	56	0.48	7.70	8.60	0.040	
0287	11	26	14.4	-12	49	18	>0.85	6.76	7.40	0.033	
0288	11	26	57.5	-11	51	49	0.43	9.41	10.20	0.030	
0289	11	27	01.5	-11	53	55	0.42	6.33	6.88	0.030	
0290	11	27	32.5	-12	06	14	0.60	6.45	6.98	0.028	
0291	11	27	33.6	-12	12	52	0.77	7.49	8.16	0.031	
0292	11	27	42.1	-12	06	24	0.67	6.33	6.85	0.028	
0293	11	27	49.7	-12	13	36	0.71	6.25	6.79	0.030	
0294	11	28	07.0	-12	39	02	0.75	10.10	11.00	0.032	
0295	11	28	24.7	-11	31	00	0.42	6.38	7.15	0.041	
0296	11	28	31.1	-11	59	52	0.65	6.76	7.36	0.031	
0297	11	28	31.3	-12	35	16	0.34	9.87	10.80	0.031	
0298	11	28	33.6	-12	32	43	0.34	8.26	8.99	0.031	
0299	11	28	33.9	-12	04	18	0.43	6.74	7.31	0.029	
0300	11	28	35.5	-12	32	15	0.32	6.69	7.28	0.030	
0301	11	29	03.3	-11	59	24	0.49	6.59	7.12	0.028	
0302	11	29	19.1	-12	07	42	0.39	10.10	10.90	0.027	
0303	11	29	26.2	-11	34	33	0.36	6.70	7.32	0.032	
0304	11	29	48.1	-12	43	23	0.37	12.40	13.70	0.036	
0305	11	29	56.0	-12	09	57	0.35	8.93	9.59	0.026	
0306	11	29	59.6	-11	53	06	0.40	11.00	11.90	0.026	
0307	11	30	02.7	-12	34	18	0.35	6.46	7.09	0.034	
0308	11	30	28.6	-11	35	26	0.39	9.15	9.96	0.031	
0309	11	30	45.8	-12	31	43	0.55	7.34	8.04	0.033	
0310	11	30	49.7	-12	22	28	0.48	7.47	8.19	0.033	
0311	11	31	28.0	-11	53	56	0.74	8.07	8.71	0.028	

TABLE 1—*Continued*

ID	α (J2000)			δ (J2000)			z_{est}	Σ_{obs}	Σ_{cor}	E(B-V)	Notes
	h	m	s	°	'	''					
0312	11	31	54.0	-11	30	36	0.40	6.84	7.48	0.032	
0313	11	32	07.6	-11	49	01	0.71	6.97	7.53	0.028	
0314	11	32	15.7	-11	48	20	0.35	7.31	7.90	0.028	
0315	11	32	34.7	-11	50	22	0.43	6.55	7.08	0.028	
0316	11	32	53.3	-12	52	23	0.74	6.54	7.36	0.042	
0317	11	32	58.8	-12	07	51	0.56	6.36	6.87	0.028	
0318	11	33	11.2	-12	39	23	0.79	6.58	7.26	0.036	
0319	11	33	13.7	-11	31	20	0.81	9.59	10.40	0.029	
0320	11	33	30.5	-12	29	03	0.66	6.35	6.95	0.033	
0321	11	34	39.3	-11	45	38	0.40	8.61	9.30	0.028	
0322	11	34	50.0	-11	38	06	0.56	6.51	7.05	0.029	
0323	11	34	54.2	-11	36	28	0.55	6.38	6.91	0.029	
0324	11	35	35.0	-12	56	58	0.38	6.68	7.48	0.041	
0325	11	35	39.9	-12	47	30	0.42	6.56	7.32	0.040	
0326	11	35	45.6	-11	33	34	0.38	7.28	7.90	0.030	
0327	11	35	56.9	-12	37	16	0.62	7.74	8.60	0.038	
0328	11	36	01.7	-11	41	39	0.39	8.55	9.25	0.028	
0329	11	36	05.7	-12	47	32	0.59	6.28	7.04	0.041	
0330	11	36	20.7	-12	58	00	0.65	6.70	7.51	0.041	
0331	11	36	21.5	-12	59	23	0.37	11.60	13.00	0.042	
0332	11	36	28.7	-11	38	46	0.33	10.30	11.10	0.029	
0333	11	36	33.5	-12	52	03	0.37	11.00	12.30	0.043	
0334	11	36	47.1	-11	45	33	0.67	7.34	7.90	0.027	$z_{Keck}=0.64$
0335	11	37	50.2	-12	31	26	0.36	6.35	7.05	0.038	
0336	11	38	00.4	-12	59	51	0.33	6.85	7.50	0.033	
0337	11	38	01.0	-11	35	30	0.47	8.34	8.85	0.021	
0338	11	38	06.6	-11	42	10	0.52	7.36	7.81	0.021	$z_{Keck}=0.45$
0339	11	38	09.3	-12	26	16	0.41	8.27	9.17	0.037	
0340	11	38	10.3	-11	33	59	0.85	8.76	9.27	0.021	
0341	11	38	38.2	-12	24	35	0.81	6.56	7.21	0.034	
0342	11	38	41.0	-12	05	04	0.43	7.17	7.85	0.033	
0343	11	38	50.5	-12	20	56	0.30	7.07	7.79	0.035	
0344	11	40	19.2	-12	18	33	0.52	6.68	7.29	0.031	
0345	11	40	23.9	-12	00	17	0.79	6.83	7.44	0.031	
0346	11	40	42.6	-11	43	30	0.80	6.27	6.75	0.027	
0347	11	40	43.8	-12	59	34	0.30	9.38	10.60	0.043	
0348	11	40	46.2	-12	56	15	0.51	7.15	8.07	0.044	
0349	11	41	07.9	-12	40	08	0.37	6.53	7.26	0.038	
0350	11	41	37.6	-12	22	29	0.37	6.43	7.00	0.031	
0351	11	41	44.4	-12	56	19	0.31	8.45	9.55	0.044	
0352	11	41	51.5	-11	44	25	0.56	6.42	7.00	0.031	
0353	11	41	55.9	-12	27	21	0.39	6.68	7.28	0.031	
0354	11	41	58.7	-11	39	36	0.65	9.83	10.70	0.031	Tidal Tail
0355	11	42	12.5	-11	54	41	0.76	6.27	6.77	0.028	
0356	11	43	54.1	-12	57	45	0.61	6.26	6.97	0.039	
0357	11	44	16.6	-12	37	41	0.52	6.77	7.38	0.031	
0358	11	44	19.8	-12	59	28	0.37	7.07	7.82	0.037	
0359	11	44	28.3	-11	52	32	0.56	7.05	7.59	0.027	LSB
0360	11	45	01.7	-12	33	36	0.39	9.17	9.96	0.030	
0361	11	45	07.0	-12	24	59	0.37	7.60	8.19	0.027	
0362	11	45	19.0	-12	58	38	0.44	8.41	9.22	0.033	
0363	11	45	22.4	-11	55	52	0.44	7.20	7.72	0.025	

TABLE 1—*Continued*

ID	α (J2000)			δ (J2000)			z_{est}	Σ_{obs}	Σ_{cor}	E(B-V)	Notes
	h	m	s	°	'	''					
0364	11	46	12.4	-11	52	16	0.71	6.63	7.07	0.023	
0365	11	46	13.4	-12	48	12	0.69	6.45	7.03	0.031	
0366	11	46	14.4	-12	38	19	0.38	7.64	8.36	0.033	
0367	11	46	44.4	-12	03	13	0.50	8.15	8.75	0.026	
0368	11	47	02.3	-12	08	10	0.55	6.44	6.95	0.027	
0369	11	47	08.9	-11	58	48	0.58	6.83	7.36	0.027	
0370	11	47	24.5	-11	37	05	0.66	6.84	7.27	0.022	
0371	11	47	25.9	-12	12	13	0.80	8.89	9.67	0.031	
0372	11	47	32.7	-12	52	38	0.67	7.36	8.09	0.034	
0373	11	47	53.3	-11	55	31	0.30	9.84	10.60	0.026	
0374	11	48	06.0	-11	45	33	0.53	8.76	9.38	0.025	
0375	11	48	23.4	-11	48	04	0.32	8.45	9.03	0.024	
0376	11	48	53.8	-12	57	52	0.46	6.58	7.27	0.036	
0377	11	48	56.9	-11	52	32	0.42	6.52	7.00	0.025	
0378	11	49	01.2	-12	14	36	0.37	6.50	7.09	0.032	
0379	11	49	25.1	-12	43	01	>0.85	6.54	7.24	0.037	
0380	11	49	30.1	-12	01	35	>0.85	6.34	7.00	0.036	
0381	11	51	22.4	-12	33	33	>0.85	7.08	8.22	0.054	
0382	11	51	23.3	-12	37	11	0.71	6.80	7.86	0.053	
0383	11	51	51.2	-12	48	35	0.38	9.39	10.60	0.043	
0384	11	52	18.0	-12	22	49	0.73	6.61	7.77	0.058	
0385	11	52	31.9	-12	17	42	0.37	9.23	10.80	0.058	
0386	11	52	32.2	-12	44	17	0.43	6.83	7.80	0.048	
0387	11	52	35.3	-11	57	50	0.52	7.68	8.98	0.057	
0388	11	52	38.9	-11	58	43	0.82	7.48	8.81	0.059	
0389	11	52	49.5	-11	53	35	0.84	6.88	8.13	0.060	
0390	11	52	51.1	-12	17	45	0.50	6.25	7.41	0.061	
0391	11	53	06.4	-12	02	34	0.31	7.96	9.38	0.059	
0392	11	53	12.0	-11	53	40	0.42	7.19	8.52	0.062	
0393	11	53	33.7	-12	00	28	0.37	9.76	11.50	0.059	
0394	11	53	35.4	-11	53	33	>0.85	8.15	9.60	0.059	
0395	11	53	38.4	-11	59	05	0.62	6.31	7.42	0.059	
0396	11	53	56.4	-12	36	52	0.44	7.39	8.34	0.044	
0397	11	54	09.9	-11	49	52	0.38	6.88	7.90	0.050	
0398	11	54	29.4	-12	04	45	0.84	7.36	8.60	0.056	
0399	11	54	31.1	-12	03	09	0.85	9.79	11.50	0.058	
0400	11	54	48.0	-11	57	51	>0.85	6.30	7.51	0.064	
0401	11	55	16.1	-12	00	45	0.75	6.28	7.58	0.068	
0402	11	55	24.5	-12	10	19	>0.85	6.85	8.07	0.060	
0403	11	55	39.0	-12	23	00	0.35	6.48	7.36	0.046	
0404	11	55	42.3	-11	56	09	>0.85	8.63	10.60	0.073	
0405	11	55	42.5	-12	34	32	0.38	7.04	7.89	0.041	
0406	11	55	53.4	-11	52	28	0.71	9.53	11.50	0.069	
0407	11	55	56.8	-12	02	02	0.76	6.52	8.00	0.074	
0408	11	56	00.0	-12	03	26	0.74	7.07	8.55	0.069	
0409	11	56	35.0	-11	39	38	0.61	6.76	8.01	0.061	
0410	11	56	46.7	-12	42	14	0.40	14.80	16.80	0.046	
0411	11	56	53.1	-11	36	06	0.72	8.34	9.90	0.062	
0412	11	57	11.7	-12	22	24	0.54	6.92	8.16	0.060	
0413	11	57	15.8	-12	43	53	0.34	9.13	10.50	0.049	
0414	11	57	26.9	-12	21	33	0.72	6.77	8.04	0.062	
0415	11	57	34.7	-12	18	48	0.60	8.87	10.70	0.069	

TABLE 1—*Continued*

ID	α (J2000)			δ (J2000)			z_{est}	Σ_{obs}	Σ_{cor}	E(B-V)	Notes
	h	m	s	°	'	''					
0416	11	57	53.1	-12	10	27	0.68	7.55	9.08	0.067	
0417	11	57	54.3	-11	51	22	0.82	9.81	11.60	0.061	
0418	11	58	14.6	-12	14	11	0.65	8.94	10.30	0.052	
0419	11	58	19.9	-12	48	47	0.83	6.44	7.60	0.060	
0420	11	58	37.1	-12	11	29	0.37	8.70	10.10	0.054	
0421	11	58	59.0	-12	14	31	0.65	6.54	7.64	0.056	
0422	11	59	18.3	-12	33	32	0.79	7.04	8.31	0.060	
0423	12	00	20.9	-12	00	35	0.38	6.52	7.49	0.050	
0424	12	00	25.8	-12	46	22	0.76	7.34	8.42	0.049	
0425	12	00	34.3	-12	59	54	0.81	6.33	7.36	0.055	
0426	12	00	53.0	-12	58	45	0.52	6.60	7.64	0.053	
0427	12	01	08.1	-12	59	47	0.84	8.77	10.10	0.052	
0428	12	01	28.3	-12	24	09	0.80	7.74	8.99	0.054	
0429	12	02	02.3	-12	35	29	0.38	6.52	7.49	0.050	
0430	12	02	43.1	-12	24	31	0.49	8.23	9.57	0.055	
0431	12	02	48.2	-12	48	23	0.35	8.52	9.70	0.047	
0432	12	02	50.0	-12	22	06	0.42	9.08	10.50	0.052	
0433	12	02	50.8	-12	40	25	0.59	6.94	7.95	0.049	
0434	12	02	57.0	-12	33	18	0.40	8.91	10.20	0.050	LSB
0435	12	03	27.4	-12	18	20	0.40	7.55	8.58	0.046	
0436	12	03	35.1	-12	14	35	0.46	7.29	8.29	0.047	
0437	12	03	38.1	-12	45	24	0.38	6.32	7.39	0.057	
0438	12	03	44.9	-11	59	01	0.80	6.74	7.79	0.053	
0439	12	03	45.6	-12	20	12	0.36	9.43	10.70	0.046	
0440	12	04	23.7	-12	53	50	0.39	11.30	13.40	0.061	
0441	12	05	05.5	-12	47	27	0.44	6.47	7.72	0.064	
0442	12	05	14.5	-12	56	28	0.31	8.08	9.89	0.073	
0443	12	05	15.1	-12	50	31	0.83	6.48	7.81	0.067	
0444	12	06	01.7	-12	38	16	0.74	6.79	8.32	0.073	
0445	12	06	04.3	-12	42	32	0.41	6.70	8.23	0.075	
0446	12	06	05.0	-11	53	57	0.37	9.03	11.10	0.074	
0447	12	06	07.1	-12	03	38	0.34	8.29	10.10	0.071	
0448	12	06	20.8	-11	48	17	0.38	15.80	19.20	0.069	
0449	12	06	54.2	-12	35	38	0.35	6.32	7.71	0.072	
0450	12	07	01.3	-12	54	39	0.50	6.87	8.79	0.089	
0451	12	07	03.0	-11	54	42	0.38	6.38	7.78	0.072	
0452	12	07	04.1	-11	52	35	0.83	7.24	8.77	0.069	
0453	12	07	06.7	-12	46	41	0.81	6.49	8.20	0.085	
0454	12	07	18.7	-12	08	26	0.36	6.30	7.86	0.080	
0455	12	07	20.2	-12	40	10	0.37	9.79	12.20	0.079	
0456	12	07	23.1	-12	21	13	0.36	7.85	9.57	0.072	
0457	12	07	25.7	-12	42	18	0.74	7.34	9.27	0.085	
0458	12	07	28.7	-12	45	47	0.79	7.07	9.05	0.089	
0459	12	07	41.7	-12	05	18	0.38	9.92	12.60	0.086	
0460	12	08	00.4	-12	22	00	0.54	6.58	7.96	0.069	
0461	12	08	39.3	-12	44	19	0.39	7.34	9.38	0.089	
0462	12	08	47.9	-12	46	35	0.35	10.70	13.90	0.092	
0463	12	08	51.3	-11	33	38	0.37	6.42	7.65	0.063	
0464	12	08	54.1	-12	28	03	0.74	6.43	7.79	0.069	
0465	12	09	08.1	-12	35	16	0.71	7.81	9.49	0.071	
0466	12	09	55.8	-13	00	09	0.45	7.25	9.13	0.083	
0467	12	10	04.8	-12	05	03	0.32	7.85	9.33	0.063	

TABLE 1—*Continued*

ID	α (J2000)			δ (J2000)			z_{est}	Σ_{obs}	Σ_{cor}	E(B-V)	Notes
	h	m	s	°	'	''					
0468	12	10	12.7	-12	19	07	0.74	7.63	9.42	0.076	
0469	12	10	21.8	-12	56	20	0.60	9.86	12.40	0.084	
0470	12	10	22.4	-12	08	56	0.78	6.56	7.95	0.069	
0471	12	10	29.6	-12	57	27	0.78	6.72	8.43	0.082	
0472	12	10	33.8	-12	37	08	0.84	7.85	10.20	0.094	
0473	12	10	40.3	-12	34	34	0.51	9.17	12.00	0.096	Possible LSB
0474	12	10	51.1	-12	35	09	>0.85	7.15	9.36	0.098	
0475	12	11	01.5	-12	48	04	0.48	7.90	9.57	0.069	
0476	12	11	08.9	-11	58	04	0.55	6.68	8.22	0.075	
0477	12	11	24.6	-12	11	58	0.74	6.25	7.74	0.077	
0478	12	11	24.6	-12	30	58	0.63	6.64	8.39	0.085	
0479	12	11	38.8	-11	37	05	0.39	9.34	11.20	0.067	
0480	12	11	40.1	-12	14	59	>0.85	6.52	8.10	0.079	
0481	12	12	08.1	-12	06	18	0.46	6.30	7.95	0.084	
0482	12	12	09.7	-12	56	06	>0.85	6.86	7.99	0.056	
0483	12	12	13.7	-12	06	11	0.70	7.22	9.08	0.083	
0484	12	12	21.9	-12	02	48	0.83	6.40	8.02	0.082	
0485	12	12	28.2	-12	47	45	0.42	7.24	8.32	0.050	
0486	12	12	29.9	-12	16	19	0.61	9.07	11.10	0.072	
0487	12	12	38.5	-12	54	59	0.31	8.26	9.47	0.049	
0488	12	12	39.2	-12	25	57	0.66	6.85	8.14	0.062	
0489	12	12	49.3	-12	22	10	0.31	6.42	7.59	0.061	
0490	12	12	54.2	-12	32	12	0.80	7.11	8.31	0.056	
0491	12	13	02.4	-11	35	43	0.39	6.66	8.09	0.070	
0492	12	13	09.5	-12	52	32	0.34	8.03	9.15	0.047	
0493	12	13	46.1	-12	49	37	0.71	6.96	7.94	0.048	
0494	12	13	48.1	-12	32	05	0.36	7.82	9.00	0.051	
0495	12	14	25.0	-11	37	54	0.77	6.42	7.41	0.052	
0496	12	14	38.5	-12	31	40	0.50	8.10	9.09	0.042	
0497	12	14	46.8	-11	41	19	0.41	10.70	12.20	0.048	
0498	12	14	47.3	-12	54	49	0.42	6.34	7.17	0.044	
0499	12	15	28.6	-12	52	36	0.85	7.97	9.12	0.049	
0500	12	15	40.5	-11	56	48	0.69	6.47	7.20	0.039	
0501	12	15	59.3	-12	04	12	0.46	7.29	8.09	0.037	Possible LSB
0502	12	16	30.8	-12	07	32	0.63	6.46	7.22	0.040	
0503	12	16	41.4	-12	39	51	0.43	10.00	11.50	0.049	
0504	12	16	45.1	-12	01	17	0.80	8.15	9.07	0.039	$z_{Keck}=0.80$
0505	12	16	48.8	-12	08	19	0.48	6.26	7.02	0.042	
0506	12	17	18.1	-12	00	53	0.33	7.85	8.75	0.039	
0507	12	18	09.1	-12	48	49	0.47	6.47	7.92	0.073	
0508	12	18	44.4	-11	52	06	0.40	9.42	10.70	0.046	
0509	12	18	47.9	-12	09	02	0.43	6.40	7.31	0.048	
0510	12	19	06.0	-12	04	49	0.38	6.31	7.16	0.046	
0511	12	19	08.1	-11	49	44	0.34	6.31	7.07	0.041	
0512	12	19	23.5	-12	01	10	0.63	6.42	7.24	0.043	
0513	12	19	34.9	-11	54	23	0.68	6.56	7.41	0.044	
0514	12	19	37.6	-12	03	04	0.58	7.51	8.44	0.042	
0515	12	19	44.5	-12	01	35	0.55	6.96	7.82	0.042	
0516	12	19	50.9	-11	57	33	0.63	7.26	8.17	0.043	
0517	12	20	59.3	-11	38	49	0.43	9.37	10.40	0.038	
0518	12	21	57.8	-11	58	19	0.32	11.10	12.50	0.041	
0519	12	22	01.1	-12	48	03	0.77	6.38	7.43	0.055	

TABLE 1—*Continued*

ID	α (J2000)			δ (J2000)			z_{est}	Σ_{obs}	Σ_{cor}	E(B-V)	Notes
	h	m	s	°	'	''					
0520	12	22	22.4	-12	12	08	0.45	6.97	7.83	0.042	Possible LSB
0521	12	22	32.4	-12	02	05	0.31	6.80	7.64	0.042	
0522	12	24	43.0	-12	48	41	0.34	9.77	11.10	0.048	
0523	12	26	10.8	-12	35	51	0.69	6.26	7.07	0.044	
0524	12	26	20.5	-11	41	27	0.42	6.51	7.34	0.043	
0525	12	26	40.1	-12	25	10	0.64	6.48	7.35	0.046	
0526	12	26	51.1	-12	24	22	0.84	6.73	7.66	0.047	
0527	12	26	54.8	-12	12	11	0.51	6.34	7.16	0.044	
0528	12	27	07.8	-12	52	46	0.36	6.84	7.85	0.050	LSB
0529	12	27	13.8	-12	07	24	0.76	6.49	7.33	0.044	
0530	12	27	16.0	-12	33	31	0.50	8.21	9.32	0.046	
0531	12	27	53.9	-11	38	20	0.79	8.37	9.53	0.047	
0532	12	27	56.5	-12	24	56	0.44	7.34	8.47	0.052	
0533	12	28	16.2	-11	49	35	0.44	6.51	7.35	0.044	
0534	12	28	22.0	-12	37	57	0.46	10.50	12.10	0.050	
0535	12	29	25.5	-11	52	24	0.52	6.31	7.16	0.046	LSB
0536	12	29	48.3	-12	51	48	0.45	7.15	8.25	0.052	
0537	12	30	07.2	-12	13	41	0.66	6.36	7.29	0.050	
0538	12	31	03.9	-12	44	51	0.80	6.85	7.94	0.054	
0539	12	32	10.9	-12	10	40	0.43	6.63	7.68	0.053	
0540	12	32	22.3	-12	37	06	0.33	7.72	9.02	0.056	
0541	12	32	30.5	-12	50	33	0.48	8.83	10.40	0.061	
0542	12	32	32.4	-12	31	44	0.41	8.66	10.10	0.057	
0543	12	32	34.4	-12	21	31	0.69	6.26	7.31	0.056	
0544	12	32	45.2	-12	17	40	0.41	7.85	9.12	0.054	
0545	12	34	05.0	-12	03	44	0.35	7.09	8.20	0.053	
0546	12	34	25.8	-12	59	28	0.58	6.46	7.65	0.061	
0547	12	34	32.9	-12	11	08	0.43	7.00	8.31	0.062	
0548	12	35	05.1	-12	24	57	0.50	7.14	8.62	0.068	
0549	12	35	25.0	-12	50	47	0.40	8.67	10.30	0.061	
0550	12	35	27.7	-12	57	01	0.57	7.72	9.12	0.060	
0551	12	35	40.0	-12	45	57	0.46	6.43	7.61	0.061	
0552	12	36	23.6	-12	41	14	0.56	6.90	8.17	0.061	
0553	12	36	56.1	-11	50	46	0.54	6.39	7.31	0.049	
0554	12	37	13.9	-12	00	59	0.55	6.55	7.60	0.054	
0555	12	37	16.9	-11	48	57	0.77	6.63	7.57	0.048	
0556	12	37	17.4	-12	38	44	0.33	10.80	12.60	0.053	
0557	12	37	23.6	-12	20	48	0.59	7.62	8.72	0.049	
0558	12	37	26.1	-12	09	12	0.38	7.91	9.10	0.051	
0559	12	37	27.1	-11	32	24	0.47	6.54	7.32	0.041	
0560	12	37	46.2	-12	46	50	0.46	9.53	11.00	0.050	LSB
0561	12	37	54.1	-11	42	49	0.47	6.65	7.49	0.043	LSB
0562	12	37	55.2	-12	22	12	>0.85	6.32	7.18	0.046	
0563	12	38	05.2	-12	47	08	0.39	15.40	17.60	0.048	
0564	12	38	09.9	-11	55	55	0.33	8.90	10.30	0.053	
0565	12	38	12.5	-12	45	37	0.47	7.12	8.11	0.047	
0566	12	38	19.8	-12	31	29	0.34	6.76	7.77	0.050	
0567	12	38	33.5	-11	44	28	0.47	8.28	9.43	0.047	
0568	12	38	42.6	-12	58	16	0.74	6.45	7.38	0.049	
0569	12	38	54.7	-12	23	03	0.34	9.74	11.10	0.048	
0570	12	38	55.9	-11	52	03	0.51	7.21	8.26	0.049	
0571	12	40	15.0	-12	01	27	0.48	7.19	8.20	0.048	

TABLE 1—*Continued*

ID	α (J2000)			δ (J2000)			z_{est}	Σ_{obs}	Σ_{cor}	E(B-V)	Notes
	h	m	s	°	'	''					
0572	12	40	43.1	-11	54	27	0.43	7.01	8.02	0.049	
0573	12	40	47.4	-12	00	08	0.41	6.65	7.59	0.048	
0574	12	41	11.9	-12	20	46	0.42	6.47	7.51	0.054	
0575	12	41	14.3	-11	46	36	0.42	7.42	8.56	0.052	
0576	12	41	35.0	-11	57	26	0.61	7.29	8.53	0.057	
0577	12	41	52.7	-12	00	39	0.74	6.59	7.63	0.053	
0578	12	42	34.1	-12	52	19	0.53	6.30	7.12	0.044	
0579	12	42	41.5	-11	34	42	0.55	6.72	7.78	0.053	
0580	12	42	45.3	-11	36	44	0.48	7.49	8.63	0.051	
0581	12	43	44.5	-11	40	46	0.44	9.58	11.00	0.051	
0582	12	44	23.9	-12	10	34	0.47	7.07	8.21	0.054	
0583	12	44	36.8	-12	29	48	0.81	6.44	7.49	0.054	
0584	12	44	39.5	-11	49	54	0.43	7.20	8.25	0.049	
0585	12	44	49.5	-11	44	12	0.39	8.12	9.21	0.046	
0586	12	44	51.7	-12	56	56	0.58	8.13	9.36	0.051	
0587	12	44	54.4	-12	38	08	0.74	12.60	14.30	0.047	Possible Dwarf
0588	12	44	56.4	-12	37	21	0.32	8.29	9.43	0.047	
0589	12	45	02.0	-11	49	19	0.50	9.20	10.50	0.047	
0590	12	45	20.2	-11	45	43	0.44	6.49	7.32	0.043	
0591	12	45	40.7	-12	39	40	0.34	8.01	9.05	0.044	
0592	12	47	15.7	-12	25	23	0.40	7.20	8.21	0.048	
0593	12	48	21.1	-12	56	42	0.46	11.60	13.40	0.053	
0594	12	48	53.1	-12	05	28	0.65	6.35	7.17	0.044	
0595	12	49	04.8	-12	49	59	0.56	6.29	7.29	0.053	
0596	12	49	11.7	-12	39	26	0.34	10.00	11.60	0.053	
0597	12	49	27.9	-11	50	33	0.41	8.49	9.60	0.045	
0598	12	50	17.8	-12	12	57	0.68	6.51	7.29	0.041	
0599	12	50	20.0	-12	45	38	0.53	9.58	11.00	0.051	
0600	12	50	28.2	-11	43	36	0.69	6.37	7.23	0.046	
0601	12	50	59.2	-12	05	04	0.44	7.08	7.96	0.042	
0602	12	51	00.3	-11	45	47	0.35	7.32	8.32	0.046	
0603	12	51	41.6	-12	29	42	0.70	8.55	9.47	0.037	
0604	12	52	12.1	-12	09	13	0.77	6.41	7.25	0.044	
0605	12	52	26.0	-12	20	17	0.50	8.92	9.91	0.038	LSB
0606	12	52	33.2	-11	49	34	0.37	6.60	7.57	0.049	
0607	12	52	34.7	-11	53	56	0.47	6.92	7.92	0.049	
0608	12	52	49.7	-12	57	52	0.75	6.48	7.32	0.044	
0609	12	52	59.1	-12	31	01	0.50	6.54	7.31	0.041	
0610	12	53	05.6	-13	01	02	0.38	9.06	10.30	0.047	LSB
0611	12	53	27.5	-12	25	12	0.37	6.86	7.75	0.044	
0612	12	54	07.3	-12	28	55	0.79	6.47	7.41	0.049	
0613	12	54	29.9	-12	20	02	0.31	11.30	13.00	0.050	
0614	12	55	02.3	-12	12	22	>0.85	9.38	10.60	0.045	Dwarf
0615	12	55	11.3	-12	53	33	0.73	6.81	7.91	0.054	
0616	12	55	31.5	-12	16	55	0.54	9.77	11.00	0.044	
0617	12	55	33.8	-12	41	44	0.43	7.18	8.23	0.049	LSB
0618	12	55	51.7	-12	50	09	0.46	6.26	7.30	0.056	
0619	12	56	17.8	-12	47	55	0.39	14.60	16.90	0.052	
0620	12	56	18.7	-12	51	44	0.55	7.00	8.17	0.056	
0621	12	57	19.0	-11	51	17	0.40	7.17	8.08	0.043	
0622	12	58	24.2	-11	34	22	0.85	6.39	7.34	0.051	
0623	12	58	45.6	-11	59	38	0.42	6.27	7.06	0.043	

TABLE 1—*Continued*

ID	α (J2000)			δ (J2000)			z_{est}	Σ_{obs}	Σ_{cor}	E(<i>B-V</i>)	Notes
	h	m	s	°	'	''					
0624	12	58	55.9	-12	15	05	0.65	7.23	8.10	0.041	
0625	12	59	33.4	-12	40	49	0.48	6.66	7.54	0.045	
0626	12	59	43.2	-11	46	51	0.65	6.53	7.42	0.046	
0627	13	00	01.4	-12	41	48	0.33	7.51	8.47	0.044	
0628	13	00	09.8	-12	41	46	0.42	6.28	7.09	0.044	
0629	13	00	10.5	-11	38	00	0.37	6.80	7.75	0.048	
0630	13	00	21.5	-11	45	11	0.60	6.59	7.57	0.050	
0631	13	00	34.1	-12	01	50	0.85	6.66	7.51	0.043	
0632	13	01	30.0	-11	38	31	0.57	7.90	9.02	0.048	
0633	13	01	34.8	-11	38	32	0.43	10.50	12.00	0.048	
0634	13	01	40.1	-11	39	24	0.48	8.35	9.50	0.047	
0635	13	01	44.9	-12	13	24	0.50	8.65	9.86	0.047	
0636	13	01	49.9	-12	28	10	0.66	7.03	7.88	0.041	
0637	13	02	09.4	-12	14	28	0.53	7.47	8.53	0.048	
0638	13	02	25.5	-12	27	48	0.36	9.52	10.70	0.042	
0639	13	02	55.6	-11	37	22	>0.85	16.80	19.60	0.057	Dwarf
0640	13	02	59.5	-12	34	34	0.62	6.39	7.22	0.044	
0641	13	03	16.9	-11	49	25	0.66	8.03	9.28	0.052	
0642	13	03	23.1	-11	53	12	0.54	8.24	9.49	0.051	
0643	13	04	07.0	-12	09	60	0.51	7.00	7.96	0.046	
0644	13	04	25.3	-11	47	26	0.71	6.76	7.84	0.054	
0645	13	04	26.1	-11	49	21	0.66	7.02	8.10	0.052	
0646	13	04	46.3	-12	27	35	0.67	6.75	7.60	0.043	
0647	13	05	32.7	-12	55	09	0.44	6.83	7.62	0.040	
0648	13	05	33.6	-12	12	55	0.34	8.04	9.04	0.043	
0649	13	06	20.4	-11	53	55	0.58	6.39	7.38	0.052	
0650	13	06	24.5	-12	29	06	0.43	7.69	8.65	0.043	
0651	13	06	31.4	-12	31	44	0.78	7.92	8.89	0.042	
0652	13	06	32.5	-12	42	51	0.54	7.72	8.78	0.047	
0653	13	06	41.1	-11	34	44	0.48	6.89	8.42	0.073	
0654	13	07	29.9	-11	52	10	0.38	6.96	8.53	0.074	
0655	13	07	37.4	-12	07	55	0.40	7.44	8.56	0.051	
0656	13	07	43.2	-12	45	26	0.55	6.90	7.99	0.053	
0657	13	07	45.1	-12	05	06	0.42	7.96	9.34	0.058	
0658	13	08	09.9	-12	45	30	0.52	7.05	8.07	0.049	
0659	13	08	49.9	-12	14	48	0.54	7.80	8.75	0.042	
0660	13	09	27.1	-11	36	47	0.43	6.47	7.56	0.056	
0661	13	10	10.7	-12	31	23	0.57	9.71	11.20	0.051	
0662	13	10	31.4	-11	39	41	0.36	15.20	17.60	0.053	
0663	13	10	47.7	-11	59	46	0.79	6.58	7.65	0.055	
0664	13	10	56.9	-12	27	11	0.37	8.96	10.20	0.046	
0665	13	11	01.0	-12	01	30	0.78	8.57	9.96	0.055	
0666	13	11	29.6	-12	12	28	0.55	6.45	7.55	0.057	
0667	13	11	31.7	-12	32	25	0.61	6.85	7.92	0.052	
0668	13	11	41.8	-11	53	56	0.38	6.63	7.63	0.051	
0669	13	12	09.9	-11	33	44	0.40	6.83	7.78	0.047	
0670	13	12	26.8	-12	11	53	0.81	6.89	8.27	0.066	
0671	13	12	27.4	-12	36	13	0.65	7.23	8.31	0.050	
0672	13	12	33.4	-12	15	39	0.85	6.58	7.87	0.065	
0673	13	12	47.9	-12	55	12	>0.85	6.63	7.70	0.054	
0674	13	12	53.5	-12	33	40	0.78	7.96	9.11	0.049	
0675	13	13	40.6	-11	53	07	0.34	8.51	9.85	0.053	

TABLE 1—*Continued*

ID	α (J2000)			δ (J2000)			z_{est}	Σ_{obs}	Σ_{cor}	E(B-V)	Notes
	h	m	s	°	'	''					
0676	13	13	41.3	-12	40	46	0.81	6.30	7.12	0.044	
0677	13	13	57.0	-11	55	27	0.42	6.35	7.30	0.050	
0678	13	14	48.0	-12	25	19	0.66	7.27	8.32	0.049	
0679	13	15	09.2	-11	43	51	0.71	7.35	8.39	0.048	
0680	13	15	15.8	-11	37	22	0.35	6.71	7.66	0.048	
0681	13	15	19.4	-11	54	11	0.50	6.26	7.09	0.045	
0682	13	15	21.2	-12	12	14	0.66	7.11	8.11	0.047	
0683	13	15	34.1	-12	27	53	0.34	6.56	7.52	0.050	
0684	13	15	47.5	-11	37	26	0.53	9.28	10.50	0.045	
0685	13	16	02.1	-11	50	19	0.55	6.47	7.27	0.042	
0686	13	16	27.0	-11	31	03	0.53	6.80	7.64	0.042	
0687	13	16	35.5	-12	10	19	0.40	7.14	8.19	0.050	
0688	13	16	59.7	-12	35	35	0.37	6.97	8.00	0.050	
0689	13	17	02.9	-12	49	45	0.38	6.36	7.35	0.052	
0690	13	17	32.9	-12	43	14	>0.85	6.37	7.33	0.051	
0691	13	17	46.1	-12	18	33	0.36	7.29	8.46	0.054	
0692	13	18	29.2	-12	21	29	0.50	6.75	7.75	0.050	
0693	13	18	46.5	-12	08	51	0.48	8.14	9.35	0.050	
0694	13	19	01.8	-12	44	30	0.57	8.19	9.35	0.048	
0695	13	19	34.0	-11	52	03	0.68	6.67	7.55	0.045	
0696	13	19	44.0	-12	04	18	0.80	6.39	7.19	0.043	
0697	13	19	44.1	-12	02	26	>0.85	6.73	7.57	0.043	
0698	13	19	50.3	-12	06	35	0.55	16.00	18.10	0.043	
0699	13	19	56.9	-12	42	11	0.38	6.49	7.48	0.052	
0700	13	20	19.2	-12	36	39	>0.85	7.54	8.73	0.053	Tidal Tail
0701	13	20	26.7	-12	09	24	0.44	6.51	7.29	0.041	
0702	13	20	49.4	-12	50	16	0.41	11.70	13.40	0.048	
0703	13	20	53.7	-12	34	36	0.83	6.62	7.71	0.055	
0704	13	20	56.7	-12	31	58	0.50	8.43	9.79	0.054	
0705	13	21	07.9	-11	43	12	0.41	6.30	7.09	0.043	
0706	13	21	16.5	-11	51	18	0.69	6.73	7.49	0.039	
0707	13	21	23.3	-12	57	13	0.52	6.32	7.18	0.046	
0708	13	21	24.7	-12	25	57	0.31	6.90	8.01	0.054	
0709	13	21	38.3	-12	17	22	0.37	8.69	9.77	0.042	
0710	13	21	59.9	-11	44	44	0.73	6.66	7.38	0.037	
0711	13	22	05.7	-12	50	39	0.45	6.81	7.71	0.045	
0712	13	22	19.8	-12	45	12	0.35	6.60	7.53	0.047	
0713	13	22	25.8	-12	20	59	0.53	7.93	8.90	0.042	
0714	13	22	32.8	-12	44	16	0.42	6.32	7.24	0.049	
0715	13	22	34.5	-12	51	54	>0.85	6.29	7.15	0.047	
0716	13	22	53.3	-11	33	11	0.79	6.78	7.93	0.057	
0717	13	22	56.9	-11	44	43	0.72	8.51	9.50	0.040	
0718	13	23	29.8	-12	32	41	0.43	9.46	10.90	0.050	
0719	13	23	50.2	-12	52	51	0.59	8.03	9.17	0.048	
0720	13	24	06.2	-12	16	48	0.42	9.98	11.20	0.041	
0721	13	24	25.3	-12	45	05	0.46	7.19	8.29	0.051	
0722	13	24	37.7	-12	22	18	0.35	6.30	7.13	0.045	
0723	13	24	48.3	-12	02	42	0.47	7.37	8.16	0.037	
0724	13	25	03.1	-12	05	16	0.49	8.60	9.50	0.036	
0725	13	25	32.2	-12	57	04	0.46	6.64	7.67	0.052	
0726	13	25	39.4	-12	47	50	>0.85	6.85	7.89	0.051	
0727	13	25	44.1	-12	20	08	0.38	9.32	10.40	0.041	

TABLE 1—*Continued*

ID	α (J2000)			δ (J2000)			z_{est}	Σ_{obs}	Σ_{cor}	E(B-V)	Notes
	h	m	s	°	'	"					
0728	13	25	45.0	-12	49	07	0.32	6.25	7.21	0.052	
0729	13	26	13.7	-12	28	35	0.76	6.33	7.18	0.045	
0730	13	26	28.3	-11	51	45	0.85	6.83	7.60	0.039	
0731	13	26	37.2	-11	46	07	0.70	7.02	7.85	0.040	
0732	13	26	50.3	-12	25	44	0.47	7.83	8.86	0.045	
0733	13	26	51.4	-12	15	22	0.33	6.76	7.58	0.042	Tidal Tail
0734	13	27	12.7	-12	23	35	0.78	6.62	7.53	0.047	
0735	13	27	14.1	-11	45	16	0.59	6.80	7.75	0.047	
0736	13	27	14.6	-12	10	49	0.45	7.18	8.04	0.041	
0737	13	27	16.4	-12	12	09	0.68	7.62	8.54	0.041	
0738	13	27	32.8	-11	52	39	0.54	6.43	7.31	0.046	
0739	13	27	34.5	-11	56	25	0.45	6.45	7.28	0.044	
0740	13	27	46.8	-12	15	47	0.38	12.50	14.30	0.049	
0741	13	27	51.4	-12	07	39	0.63	6.39	7.22	0.044	
0742	13	27	54.2	-11	57	55	0.80	6.29	7.09	0.043	
0743	13	28	05.6	-12	52	16	0.64	6.30	7.42	0.059	
0744	13	28	18.0	-12	29	12	0.71	7.31	8.56	0.057	
0745	13	28	45.9	-13	00	51	0.70	7.30	8.66	0.062	
0746	13	28	48.5	-11	40	60	0.82	7.29	8.33	0.048	
0747	13	28	52.9	-12	10	18	0.50	7.11	8.04	0.045	
0748	13	28	53.0	-12	04	21	0.67	6.66	7.46	0.041	
0749	13	29	11.3	-12	01	05	0.48	7.31	8.19	0.041	
0750	13	29	13.4	-11	56	11	0.68	7.16	8.03	0.041	
0751	13	29	17.8	-12	07	56	0.45	6.46	7.31	0.045	
0752	13	29	37.7	-12	54	02	0.79	6.28	7.44	0.061	
0753	13	29	39.1	-12	40	10	0.36	7.61	9.01	0.061	
0754	13	29	40.8	-12	28	32	0.34	6.36	7.46	0.058	
0755	13	30	22.3	-11	48	59	0.78	6.91	7.99	0.052	
0756	13	30	33.9	-12	51	56	0.56	7.51	8.88	0.060	
0757	13	30	45.1	-12	34	30	0.35	8.64	10.20	0.060	
0758	13	31	04.4	-12	59	27	0.47	8.13	9.54	0.058	
0759	13	31	14.1	-12	00	18	0.34	8.41	9.96	0.061	LSB
0760	13	31	28.3	-11	56	07	0.41	7.19	8.54	0.062	
0761	13	31	48.1	-12	17	34	0.35	8.71	10.30	0.060	
0762	13	32	20.0	-12	10	53	0.44	7.16	8.50	0.062	
0763	13	32	53.3	-12	34	04	0.51	6.92	8.16	0.060	
0764	13	33	25.7	-12	06	15	0.61	6.68	7.90	0.061	
0765	13	33	52.8	-12	59	41	0.41	7.99	9.36	0.057	
0766	13	33	57.2	-12	53	55	0.48	7.15	8.35	0.056	
0767	13	34	04.4	-12	50	57	0.41	9.43	11.00	0.057	
0768	13	34	12.3	-11	38	08	>0.85	6.33	7.52	0.063	
0769	13	34	20.5	-12	54	30	0.38	6.47	7.62	0.059	
0770	13	34	22.4	-11	52	48	0.33	10.00	11.70	0.058	
0771	13	34	35.8	-12	02	53	0.42	6.53	7.61	0.056	
0772	13	34	39.2	-11	51	15	0.40	8.94	10.40	0.055	
0773	13	35	04.8	-12	31	39	0.47	6.48	7.56	0.056	
0774	13	35	06.3	-11	41	07	>0.85	6.55	8.01	0.073	
0775	13	35	06.4	-11	55	32	0.48	13.70	15.90	0.055	
0776	13	35	32.1	-11	49	49	0.80	6.94	8.20	0.060	
0777	13	35	47.1	-11	53	46	0.63	7.12	8.36	0.058	
0778	13	35	50.4	-11	46	16	0.58	8.71	10.40	0.064	
0779	13	35	53.7	-12	11	09	0.60	6.92	8.07	0.056	

TABLE 1—*Continued*

ID	α (J2000)			δ (J2000)			z_{est}	Σ_{obs}	Σ_{cor}	E(B-V)	Notes
	h	m	s	°	'	''					
0780	13	36	13.5	-12	00	58	0.32	12.40	14.50	0.056	
0781	13	36	40.8	-12	57	25	0.35	8.20	10.00	0.073	
0782	13	36	53.4	-12	27	02	0.41	8.41	10.30	0.075	
0783	13	36	55.1	-12	57	43	0.39	6.49	7.97	0.074	
0784	13	36	58.9	-12	24	13	0.42	13.00	16.20	0.078	
0785	13	37	08.7	-12	57	14	0.62	11.50	14.10	0.074	
0786	13	37	19.6	-12	54	06	0.50	8.41	10.40	0.075	Tidal Tail
0787	13	37	21.5	-11	52	20	0.39	8.71	10.70	0.075	
0788	13	37	50.5	-12	01	04	0.82	6.28	7.92	0.084	
0789	13	37	54.7	-12	40	36	0.34	11.70	14.50	0.079	
0790	13	38	10.8	-12	57	17	0.32	7.75	9.62	0.078	
0791	13	38	21.8	-11	42	18	0.52	6.27	7.49	0.065	
0792	13	38	31.6	-12	23	50	0.49	6.61	8.30	0.082	
0793	13	38	50.7	-11	42	11	0.72	7.73	9.38	0.070	
0794	13	38	55.1	-11	34	41	0.68	6.29	7.61	0.069	
0795	13	39	22.1	-13	00	14	0.59	9.08	11.30	0.080	
0796	13	39	31.1	-11	59	40	0.46	7.05	8.85	0.082	
0797	13	39	57.0	-12	11	31	>0.85	7.90	10.30	0.095	
0798	13	39	59.4	-11	48	38	0.44	10.00	12.50	0.079	
0799	13	40	04.5	-12	07	51	0.74	10.30	13.00	0.085	
0800	13	40	06.3	-12	14	57	0.79	6.37	8.19	0.091	
0801	13	40	09.6	-12	10	09	0.67	10.40	13.20	0.088	
0802	13	40	19.2	-12	18	14	0.58	6.67	8.49	0.087	
0803	13	40	25.9	-12	15	22	0.50	6.60	8.33	0.084	
0804	13	40	28.4	-11	39	35	0.49	6.52	8.09	0.078	
0805	13	40	37.8	-12	23	07	0.58	7.50	9.44	0.083	
0806	13	40	41.9	-12	06	19	0.54	7.07	8.70	0.075	
0807	13	41	07.6	-11	47	56	>0.85	8.23	10.10	0.073	
0808	13	41	12.6	-11	45	23	0.65	6.40	7.84	0.073	
0809	13	41	38.5	-12	18	16	0.41	7.44	8.99	0.069	
0810	13	41	39.5	-11	57	28	0.63	6.69	7.99	0.064	
0811	13	41	39.7	-12	28	50	0.47	10.20	12.60	0.077	
0812	13	42	01.1	-12	34	41	0.48	6.32	7.82	0.077	
0813	13	42	04.3	-11	55	25	0.58	8.00	9.51	0.062	
0814	13	42	12.8	-12	59	28	0.54	7.64	9.35	0.073	
0815	13	42	15.1	-12	18	37	0.79	6.37	7.73	0.070	
0816	13	42	28.4	-12	25	46	0.39	6.87	8.45	0.075	
0817	13	43	22.6	-12	48	08	0.55	8.22	10.40	0.086	
0818	13	44	19.5	-12	25	41	0.81	6.72	8.43	0.082	
0819	13	44	20.4	-11	55	18	0.65	7.37	8.79	0.064	
0820	13	44	26.2	-12	00	22	0.53	6.90	8.28	0.066	
0821	13	44	37.0	-12	03	48	0.40	6.66	8.02	0.067	
0822	13	44	47.5	-12	53	41	0.80	7.28	9.34	0.090	
0823	13	45	09.5	-11	40	15	0.35	6.67	7.99	0.065	
0824	13	45	09.7	-12	03	56	0.71	7.52	8.97	0.064	
0825	13	46	24.7	-11	54	18	0.39	9.78	11.60	0.063	
0826	13	46	41.9	-12	53	35	0.54	6.79	8.43	0.079	
0827	13	46	42.4	-11	59	24	0.71	9.42	11.30	0.066	
0828	13	46	59.3	-12	28	60	0.35	6.65	8.45	0.087	
0829	13	47	31.5	-11	45	06	0.43	21.50	25.50	0.062	(1)
0830	13	47	59.7	-12	27	24	0.82	7.54	9.63	0.088	
0831	13	48	02.6	-12	46	44	0.85	6.98	8.59	0.075	

TABLE 1—*Continued*

ID	α (J2000)			δ (J2000)			z_{est}	Σ_{obs}	Σ_{cor}	E(B-V)	Notes
	h	m	s	°	'	''					
0832	13	48	05.6	-12	24	39	0.48	6.61	8.56	0.094	
0833	13	48	28.4	-11	37	33	0.55	7.17	8.59	0.065	
0834	13	48	41.5	-12	01	49	0.40	10.80	13.20	0.072	
0835	13	48	46.2	-11	48	45	0.34	9.73	11.70	0.068	
0836	13	48	52.0	-12	04	18	0.59	10.40	12.80	0.075	
0837	13	48	56.9	-12	59	39	0.65	7.33	8.98	0.073	
0838	13	50	22.6	-12	36	25	0.64	7.52	9.12	0.070	
0839	13	50	23.3	-12	14	12	0.40	6.83	8.42	0.076	
0840	13	50	40.5	-12	18	34	0.34	8.53	10.40	0.071	
0841	13	50	41.6	-12	12	13	0.39	7.04	8.62	0.073	
0842	13	50	47.6	-11	54	54	0.49	6.37	7.75	0.071	
0843	13	50	51.7	-12	17	03	0.36	8.78	10.70	0.071	
0844	13	51	14.4	-12	05	56	0.56	6.52	7.95	0.072	
0845	13	51	28.4	-12	17	03	0.39	6.52	7.81	0.065	
0846	13	51	29.6	-12	11	03	0.41	6.65	7.96	0.065	
0847	13	51	42.7	-12	32	39	>0.85	7.78	9.35	0.066	
0848	13	52	29.7	-12	45	39	0.77	7.05	8.79	0.080	
0849	13	53	01.0	-11	37	31	0.50	7.09	8.52	0.066	
0850	13	53	29.0	-12	18	46	0.77	7.65	9.36	0.073	
0851	13	53	50.2	-11	51	21	0.71	6.69	7.94	0.062	
0852	13	53	52.4	-12	44	49	0.83	6.88	8.41	0.073	
0853	13	54	09.5	-12	30	59	0.84	8.11	9.92	0.073	
0854	13	54	22.7	-11	35	39	0.43	18.00	21.20	0.061	
0855	13	54	30.1	-11	33	28	0.51	8.45	9.98	0.060	
0856	13	54	32.8	-12	23	29	0.36	6.60	8.04	0.071	
0857	13	54	50.9	-12	09	11	0.72	7.82	9.55	0.072	
0858	13	56	17.9	-12	53	56	0.79	8.15	10.30	0.083	
0859	13	56	48.4	-12	07	47	0.40	11.10	13.50	0.072	
0860	13	56	48.6	-12	30	11	0.43	6.54	8.00	0.073	
0861	13	57	09.0	-12	08	29	0.48	6.35	7.79	0.074	
0862	13	57	43.5	-13	00	04	0.37	6.67	8.40	0.084	
0863	13	57	46.9	-12	53	09	0.47	6.74	8.49	0.084	
0864	13	57	57.5	-12	14	28	0.39	7.12	8.82	0.078	
0865	13	58	10.2	-11	44	28	0.56	7.26	8.67	0.064	
0866	13	58	15.6	-12	13	50	0.47	7.92	9.90	0.081	
0867	13	58	36.7	-12	27	10	0.37	7.32	9.19	0.082	
0868	13	59	19.9	-12	32	49	0.46	7.60	9.57	0.083	
0869	13	59	24.8	-12	54	35	0.36	7.76	9.90	0.088	
0870	13	59	31.6	-12	56	30	0.35	7.29	9.25	0.086	
0871	13	59	36.9	-12	48	00	0.36	6.78	8.59	0.086	
0872	14	00	25.5	-12	31	55	0.36	16.70	20.80	0.079	
0873	14	00	33.9	-11	34	50	0.47	7.23	8.92	0.076	
0874	14	00	37.4	-12	00	03	0.82	6.43	7.97	0.078	
0875	14	00	46.5	-12	10	02	0.39	8.62	10.80	0.083	
0876	14	00	53.1	-12	01	21	0.40	10.60	13.20	0.079	
0877	14	01	25.2	-12	22	45	0.44	8.59	10.80	0.083	
0878	14	01	26.3	-12	03	32	0.68	6.67	8.38	0.083	
0879	14	01	30.8	-11	44	46	0.57	7.98	9.72	0.071	
0880	14	01	32.5	-12	16	33	0.43	6.28	7.78	0.077	
0881	14	02	48.4	-11	36	32	0.36	6.94	8.30	0.065	
0882	14	02	48.9	-11	39	16	0.44	6.93	8.32	0.066	
0883	14	03	15.8	-12	14	18	0.65	8.34	10.10	0.071	

TABLE 1—*Continued*

ID	α (J2000)			δ (J2000)			z_{est}	Σ_{obs}	Σ_{cor}	E(B-V)	Notes
	h	m	s	°	'	''					
0884	14	03	52.1	-12	54	53	0.37	6.94	8.74	0.083	
0885	14	03	56.8	-12	35	45	0.54	6.66	8.06	0.069	
0886	14	04	11.8	-11	44	22	0.52	6.95	8.43	0.070	
0887	14	04	20.5	-12	22	28	0.55	7.66	9.16	0.064	
0888	14	04	25.5	-11	39	21	0.42	7.47	9.07	0.070	
0889	14	04	33.0	-12	09	31	0.40	7.41	8.84	0.064	
0890	14	04	54.3	-11	55	38	0.39	6.28	7.46	0.063	
0891	14	04	54.6	-11	41	36	0.84	6.35	7.50	0.060	
0892	14	04	58.0	-12	32	15	0.65	6.32	7.71	0.072	
0893	14	05	00.8	-11	30	45	0.81	7.24	8.97	0.078	
0894	14	05	11.4	-11	47	09	0.64	6.52	7.68	0.059	
0895	14	05	16.1	-12	22	44	0.41	7.36	8.82	0.065	
0896	14	05	25.4	-11	52	27	0.52	6.90	8.06	0.056	
0897	14	05	28.8	-11	47	47	0.39	7.16	8.39	0.057	
0898	14	05	29.3	-12	24	45	0.49	6.59	8.04	0.072	
0899	14	05	37.0	-12	23	38	0.79	7.53	9.22	0.073	
0900	14	05	37.9	-12	46	43	0.40	6.64	7.99	0.067	LSB
0901	14	05	39.9	-12	26	07	0.71	6.77	8.31	0.074	
0902	14	05	59.8	-12	58	02	0.40	7.51	9.29	0.077	
0903	14	06	35.4	-12	21	49	0.63	6.45	7.80	0.069	
0904	14	06	37.0	-12	07	03	0.75	6.28	7.68	0.073	
0905	14	06	39.6	-11	47	59	0.45	7.30	8.52	0.056	
0906	14	06	60.0	-12	10	13	0.38	6.76	8.22	0.071	
0907	14	07	01.0	-11	58	18	0.39	6.27	7.55	0.068	
0908	14	07	34.8	-11	41	26	0.36	10.20	12.00	0.059	
0909	14	07	36.2	-12	17	11	0.34	7.42	8.82	0.063	
0910	14	07	54.2	-11	46	09	0.62	6.40	7.66	0.065	
0911	14	08	05.8	-11	31	11	0.35	9.29	11.00	0.061	
0912	14	08	17.8	-12	09	31	0.49	6.78	8.16	0.067	
0913	14	08	32.0	-12	14	15	0.34	6.30	7.60	0.068	
0914	14	08	46.2	-12	15	58	0.71	6.57	7.90	0.067	
0915	14	08	46.6	-12	33	57	0.74	7.22	8.51	0.060	
0916	14	09	08.7	-12	58	36	0.47	7.23	8.79	0.071	
0917	14	09	43.8	-12	42	02	0.35	6.54	7.83	0.065	
0918	14	10	01.1	-12	18	30	0.67	8.98	10.80	0.065	
0919	14	10	02.7	-11	33	02	0.49	7.41	9.21	0.079	
0920	14	10	26.2	-12	00	07	0.82	7.96	9.33	0.058	
0921	14	10	28.2	-12	40	35	0.69	6.67	8.08	0.069	
0922	14	10	33.3	-12	06	00	0.81	6.44	7.64	0.062	
0923	14	10	35.6	-12	25	05	0.69	8.51	10.20	0.066	
0924	14	10	50.2	-11	44	04	0.40	6.49	7.62	0.058	
0925	14	11	03.9	-11	48	22	0.47	11.10	13.00	0.056	
0926	14	11	06.6	-11	50	46	0.68	7.74	9.01	0.055	
0927	14	11	23.9	-12	46	53	0.75	6.45	7.88	0.073	
0928	14	11	58.9	-12	40	53	0.31	9.96	12.20	0.074	
0929	14	12	32.6	-11	50	15	0.69	6.58	7.67	0.055	
0930	14	13	06.1	-12	07	02	0.82	11.00	13.00	0.062	
0931	14	13	17.6	-11	55	59	0.82	6.75	8.02	0.062	
0932	14	13	35.8	-12	29	56	0.38	6.31	7.61	0.068	
0933	14	13	40.0	-12	01	04	0.58	7.80	9.26	0.062	
0934	14	14	05.9	-12	39	33	0.59	6.47	7.80	0.068	
0935	14	14	13.9	-12	54	04	0.64	6.34	7.92	0.081	

TABLE 1—*Continued*

ID	α (J2000)			δ (J2000)			z_{est}	Σ_{obs}	Σ_{cor}	E(B-V)	Notes
	h	m	s	°	'	''					
0936	14	14	37.0	-12	57	32	0.37	6.26	7.76	0.078	
0937	14	14	55.6	-11	58	08	0.47	7.27	8.59	0.060	
0938	14	15	18.0	-12	01	53	0.42	7.15	8.48	0.062	
0939	14	15	34.4	-11	44	11	0.31	6.25	7.49	0.066	
0940	14	15	45.8	-11	46	36	0.43	7.22	8.63	0.065	
0941	14	15	57.2	-11	50	47	0.51	6.42	7.62	0.062	
0942	14	16	03.0	-12	57	11	0.61	6.65	8.16	0.074	
0943	14	16	15.2	-12	01	35	0.38	6.56	7.88	0.066	
0944	14	16	30.6	-12	35	59	0.62	8.24	10.00	0.070	
0945	14	16	51.7	-12	56	46	0.76	6.38	7.94	0.079	
0946	14	17	03.8	-12	21	48	0.38	9.00	10.80	0.067	
0947	14	17	08.9	-11	34	17	0.39	6.28	7.48	0.063	
0948	14	17	32.7	-12	45	02	0.83	6.35	7.83	0.076	
0949	14	18	20.2	-11	44	51	0.37	9.42	11.30	0.066	
0950	14	19	31.3	-11	53	28	0.77	11.80	14.50	0.073	Tidal Tail
0951	14	19	57.0	-11	46	16	0.83	7.18	9.00	0.082	
0952	14	20	19.4	-12	36	36	0.49	9.36	12.20	0.096	
0953	14	20	29.4	-11	51	24	0.53	6.57	8.34	0.087	
0954	14	20	29.7	-11	34	04	0.67	13.60	17.30	0.089	
0955	14	20	32.2	-12	44	46	0.60	6.58	8.52	0.094	
0956	14	22	15.8	-12	11	15	>0.85	7.29	9.52	0.097	
0957	14	22	22.4	-12	09	01	0.54	7.71	10.10	0.099	
0958	14	23	40.4	-12	14	42	0.74	6.29	8.05	0.089	
0959	14	23	49.1	-12	30	29	0.51	6.56	8.46	0.092	
0960	14	23	52.3	-12	23	12	0.35	12.90	16.60	0.090	Tidal Tail
0961	14	24	16.7	-12	09	51	0.74	8.71	11.10	0.087	
0962	14	24	24.4	-12	01	48	0.52	7.95	10.10	0.087	
0963	14	24	41.3	-12	57	20	0.45	10.90	13.70	0.082	
0964	14	26	14.5	-12	50	13	0.37	9.81	12.50	0.089	
0965	14	26	20.6	-12	00	33	0.54	6.96	8.81	0.086	
0966	14	26	24.9	-12	46	28	0.35	9.72	12.40	0.088	
0967	14	26	42.0	-12	29	08	0.40	6.85	8.81	0.091	
0968	14	27	31.8	-12	36	20	0.76	6.66	8.62	0.094	
0969	14	27	52.5	-12	21	56	0.41	9.56	12.20	0.087	
0970	14	27	54.2	-12	10	15	0.59	6.34	8.07	0.087	
0971	14	28	22.7	-12	03	30	0.76	6.63	8.59	0.094	
0972	14	28	57.2	-12	31	12	0.36	10.40	13.60	0.096	
0973	14	28	58.4	-12	22	15	0.32	7.68	10.00	0.097	
0974	14	28	59.7	-12	27	07	0.63	8.34	10.90	0.096	
0975	14	29	37.3	-12	54	42	0.78	7.35	9.49	0.093	
0976	14	29	40.1	-11	50	01	0.35	11.60	15.10	0.096	
0977	14	30	30.2	-12	26	18	0.35	7.62	9.85	0.093	
0978	14	31	31.0	-12	43	02	0.31	7.76	9.99	0.091	
0979	14	31	40.2	-12	50	23	0.74	6.56	8.39	0.089	
0980	14	32	25.6	-12	30	20	>0.85	7.20	9.07	0.084	
0981	14	32	54.5	-12	55	25	0.37	7.61	9.57	0.083	
0982	14	33	14.4	-12	43	57	0.42	7.61	9.46	0.079	
0983	14	34	45.5	-12	59	09	0.33	6.33	8.02	0.085	
0984	14	35	23.0	-12	08	07	0.67	6.99	8.77	0.082	
0985	14	36	15.0	-12	35	19	0.72	6.30	7.77	0.076	
0986	14	36	58.8	-12	40	44	0.57	6.30	7.87	0.080	
0987	14	37	29.2	-12	20	21	0.74	6.56	8.16	0.079	

TABLE 1—*Continued*

ID	α (J2000)			δ (J2000)			z_{est}	Σ_{obs}	Σ_{cor}	E(B-V)	Notes
	h	m	s	°	'	''					
0988	14	37	42.7	-12	38	37	0.45	8.05	10.00	0.080	
0989	14	38	42.7	-12	20	60	0.58	6.62	8.17	0.076	
0990	14	38	46.0	-12	27	58	0.65	6.42	7.93	0.077	
0991	14	39	29.8	-12	19	39	0.41	7.51	9.14	0.071	
0992	14	39	49.9	-12	39	17	0.45	6.62	8.02	0.069	
0993	14	40	18.1	-12	45	58	0.37	6.94	8.31	0.065	
0994	14	40	31.1	-12	01	24	0.49	6.36	7.68	0.068	
0995	14	40	35.3	-12	27	54	0.41	7.78	9.51	0.073	
0996	14	40	45.0	-12	22	07	0.49	14.60	17.80	0.072	Possible LSB
0997	14	41	02.0	-11	52	23	0.38	6.27	7.61	0.070	
0998	14	41	32.6	-11	50	59	0.35	7.66	9.36	0.073	
0999	14	42	17.4	-12	23	03	0.33	7.22	8.73	0.069	
1000	14	42	53.9	-11	46	35	0.75	6.57	8.05	0.074	
1001	14	43	40.1	-11	58	01	0.70	6.77	8.43	0.079	
1002	14	43	44.4	-11	31	51	0.38	6.67	8.06	0.068	
1003	14	43	52.8	-11	59	29	0.40	7.29	9.04	0.078	
1004	14	43	59.4	-11	32	29	0.38	7.60	9.23	0.070	
1005	14	44	54.3	-11	36	51	0.81	6.84	8.37	0.073	
1006	14	44	57.9	-12	17	58	0.35	8.07	9.90	0.074	
1007	14	46	08.4	-12	32	08	0.53	10.20	13.10	0.089	
1008	14	46	14.4	-11	47	46	0.57	6.66	8.18	0.074	
1009	14	46	27.8	-12	38	37	0.75	7.11	9.26	0.096	
1010	14	46	47.5	-12	15	59	0.52	6.62	8.45	0.088	
1011	14	49	11.1	-12	38	14	0.60	6.55	8.18	0.080	
1012	14	49	21.6	-12	28	19	0.31	12.30	15.40	0.081	
1013	14	51	14.2	-12	39	56	0.42	8.57	10.70	0.082	
1014	14	51	38.3	-12	08	58	0.36	8.40	10.70	0.086	
1015	14	51	46.4	-11	37	21	0.57	9.24	11.80	0.089	
1016	14	51	50.8	-11	47	17	0.74	6.55	8.20	0.081	
1017	14	51	59.8	-11	51	10	0.58	6.56	8.21	0.082	
1018	14	52	01.7	-11	59	15	0.62	6.88	8.70	0.085	
1019	14	52	18.4	-11	57	56	0.35	6.88	8.68	0.084	
1020	14	52	29.6	-12	36	30	0.40	13.30	16.60	0.080	
1021	14	52	38.7	-12	34	41	0.73	6.88	8.58	0.080	
1022	14	53	25.6	-12	01	33	>0.85	6.81	8.78	0.092	
1023	14	53	35.5	-12	48	28	0.42	7.25	8.97	0.077	
1024	14	53	45.0	-11	36	23	0.42	8.17	10.20	0.079	
1025	14	53	47.0	-12	34	46	0.42	6.80	8.52	0.081	
1026	14	54	22.8	-12	33	50	0.54	7.16	8.94	0.080	
1027	14	54	31.3	-11	34	24	0.77	7.81	9.95	0.087	
1028	14	54	48.8	-11	31	57	0.39	7.98	10.20	0.088	
1029	14	54	57.7	-12	50	10	0.83	6.81	8.45	0.078	
1030	14	55	02.1	-12	58	36	0.81	7.19	8.92	0.078	
1031	14	55	09.4	-11	31	11	0.52	7.72	9.92	0.091	
1032	14	55	22.0	-12	54	22	0.75	7.14	8.80	0.076	
1033	14	56	04.2	-12	46	57	0.32	11.30	13.70	0.071	
1034	14	56	38.8	-12	38	50	0.62	7.31	8.87	0.070	
1035	14	56	44.4	-12	35	13	0.35	7.19	8.76	0.072	
1036	14	57	06.2	-12	46	33	0.46	6.44	7.79	0.069	
1037	14	58	01.3	-11	39	14	0.36	6.55	8.54	0.096	
1038	14	59	03.0	-12	51	08	0.63	7.87	9.71	0.076	
1039	15	00	18.1	-12	15	37	0.42	7.01	8.55	0.072	

TABLE 1—*Continued*

ID	$\alpha(\text{J2000})$			$\delta(\text{J2000})$			z_{est}	Σ_{obs}	Σ_{cor}	$E(B-V)$	Notes
	h	m	s	°	'	''					
1040	15	00	22.7	-11	39	39	0.80	6.37	8.37	0.099	
1041	15	00	30.1	-12	20	48	0.38	11.40	14.00	0.072	
1042	15	00	31.5	-12	21	18	0.36	10.40	12.70	0.072	
1043	15	00	44.1	-12	44	12	0.35	7.29	9.09	0.080	
1044	15	00	53.8	-12	29	44	0.31	7.14	8.80	0.076	
1045	15	00	57.6	-11	44	24	0.32	8.24	10.50	0.086	
1046	15	00	58.1	-12	16	19	0.41	8.24	10.10	0.073	
1047	15	00	59.6	-12	53	05	0.45	6.67	8.32	0.080	
1048	15	01	13.5	-11	57	60	0.35	6.26	7.74	0.077	
1049	15	01	32.3	-11	52	15	0.57	7.99	9.96	0.080	
1050	15	01	43.4	-11	51	54	0.68	7.49	9.34	0.080	
1051	15	01	51.2	-12	57	38	0.32	6.73	8.52	0.085	
1052	15	02	02.5	-11	36	23	0.32	7.29	9.50	0.096	
1053	15	03	29.2	-12	57	27	0.45	8.11	10.30	0.087	
1054	15	03	33.5	-11	59	35	0.32	10.40	13.20	0.086	
1055	15	03	34.9	-11	56	09	0.35	12.40	15.70	0.086	
1056	15	03	40.4	-12	56	17	0.83	6.26	7.94	0.086	
1057	15	04	07.4	-11	55	09	0.59	6.98	9.00	0.092	
1058	15	04	17.8	-12	14	25	0.51	6.28	8.08	0.091	
1059	15	05	27.4	-11	44	59	0.82	7.25	9.42	0.095	
1060	15	05	38.0	-12	11	56	0.41	6.32	8.33	0.100	
1061	15	05	46.4	-11	48	22	0.77	7.26	9.45	0.096	
1062	15	05	51.1	-12	29	13	0.50	6.82	8.89	0.096	
1063	15	06	11.4	-12	40	52	0.67	7.41	9.71	0.098	
1064	15	06	16.4	-12	02	33	0.38	9.01	11.80	0.098	
1065	15	06	23.2	-12	04	13	0.77	7.08	9.28	0.098	
1066	15	07	39.3	-11	58	55	0.40	11.10	14.60	0.099	
1067	15	08	39.7	-12	51	52	0.84	7.58	9.86	0.095	
1068	15	09	47.9	-12	04	35	0.40	6.52	8.55	0.098	
1069	15	10	40.6	-11	59	37	0.36	7.32	9.61	0.099	
1070	15	10	43.2	-12	22	52	0.59	6.52	8.60	0.100	
1071	15	11	19.3	-11	50	07	0.78	6.97	9.15	0.098	
1072	15	11	46.9	-12	38	30	0.40	8.92	11.60	0.097	
1073	15	11	53.3	-12	38	25	0.35	6.58	8.57	0.096	

Note. — Units for Σ_{obs} and Σ_{cor} are 10^{-3} counts s^{-1} arcsec^{-2} .
 (1) RX J1347.5 at $z=0.451$ (Schindler et al. 1995)

TABLE 2
SUPPLEMENTAL CATALOG

ID	$\alpha(J2000)$			$\delta(J2000)$			z_{est}	Σ_{obs}	Σ_{cor}	$E(B-V)$	Failed Criteria ^a	Notes
	h	m	s	°	'	''						
S001	10	06	18.8	-12	58	13	0.47	9.85	11.80	0.066	S	
S002	10	06	25.8	-12	40	48	0.60	7.77	9.05	0.055	S	
S003	10	15	38.4	-12	43	52	0.39	11.40	14.00	0.075	M	
S004	10	23	11.1	-12	33	47	0.29	13.40	16.60	0.079	z,G	
S005	10	24	09.8	-11	48	08	0.29	21.10	24.30	0.051	z,M	
S006	10	27	21.4	-11	47	48	0.50	9.75	11.20	0.051	M	
S007	10	28	33.7	-11	59	29	0.35	12.50	14.60	0.057	G	
S008	10	31	27.9	-12	35	20	0.56	7.63	9.17	0.067	S	
S009	10	36	52.7	-12	49	51	0.33	14.50	16.80	0.052	G	
S010	10	40	40.8	-12	14	00	0.52	9.84	11.20	0.048	M	
S011	10	41	40.3	-12	50	31	0.28	11.80	13.50	0.048	z	
S012	10	44	59.6	-12	43	22	0.66	7.36	8.57	0.055	M	
S013	10	46	04.6	-12	47	50	0.50	12.10	14.20	0.058	M	
S014	10	51	09.3	-12	42	55	0.63	13.30	15.30	0.050	M	
S015	10	51	13.7	-12	01	14	0.37	19.60	22.20	0.045	G	
S016	10	51	31.1	-11	38	35	0.49	9.82	11.10	0.045	M,G	
S017	10	51	31.7	-12	04	12	0.26	11.40	12.90	0.045	z,M	
S018	10	51	35.7	-11	37	45	0.50	9.74	11.00	0.045	M	
S019	10	56	55.0	-12	44	02	0.39	8.95	9.96	0.038	M	
S020	11	02	29.0	-12	47	50	0.32	11.90	13.30	0.042	G	
S021	11	16	54.4	-12	22	22	0.27	7.64	9.22	0.068	z	
S022	11	20	24.5	-12	03	16	0.28	7.83	9.29	0.062	z,LSB,M	
S023	11	23	03.9	-12	36	35	0.36	8.82	9.78	0.038	M	
S024	11	28	34.6	-12	52	29	0.37	20.20	22.30	0.034	M	
S025	11	36	32.0	-11	36	08	0.26	11.40	12.30	0.029	z,G	
S026	11	37	55.2	-12	58	49	0.35	8.52	9.35	0.033	M	
S027	11	38	26.3	-12	38	21	0.35	15.50	17.00	0.032	G	
S028	11	39	44.0	-11	46	59	0.24	11.70	12.70	0.030	z,M	
S029	11	45	16.0	-11	46	03	0.26	30.10	32.20	0.024	z,M,G	
S030	11	47	15.7	-12	51	46	0.69	6.70	7.36	0.034	S	
S031	11	47	17.0	-12	52	05	0.62	6.23	6.85	0.034	S	$z_{Kcck}=0.58$
S032	11	48	01.8	-11	31	14	0.20	13.10	14.00	0.026	z,G	
S033	11	49	06.2	-12	46	06	0.48	10.80	11.80	0.035	M	
S034	11	50	34.4	-11	49	48	0.23	11.60	13.30	0.048	z,M	
S035	11	55	28.5	-12	25	41	0.51	15.00	17.00	0.045	M	
S036	12	06	05.6	-11	33	06	0.27	11.10	13.80	0.080	z,LSB	
S037	12	06	49.6	-12	03	44	0.60	6.56	8.01	0.072	S	
S038	12	07	42.0	-11	59	08	0.26	27.60	34.30	0.079	z,LSB	
S039	12	12	39.4	-12	02	50	0.26	6.80	8.37	0.075	z	
S040	12	12	55.2	-12	37	33	0.28	21.90	25.30	0.053	z,M	
S041	12	17	06.3	-12	51	51	0.39	17.00	20.10	0.062	M	
S042	12	17	47.3	-12	01	56	0.33	10.60	12.00	0.045	M	
S043	12	39	17.9	-11	54	45	0.45	8.70	9.90	0.047	M	
S044	12	40	54.1	-12	02	00	0.43	7.62	8.71	0.048	M S	
S045	12	46	02.2	-12	48	05	0.76	9.18	10.60	0.051	M	
S046	12	46	23.4	-12	30	07	0.75	6.81	7.77	0.048	S	
S047	12	48	16.9	-12	08	28	0.34	9.20	10.30	0.042	M	
S048	12	58	59.8	-12	19	39	0.26	7.00	7.82	0.040	z,G	
S049	13	03	11.9	-12	31	56	0.76	6.55	7.36	0.042	M	
S050	13	13	07.0	-12	22	37	0.54	12.00	13.80	0.052	M	
S051	13	14	09.6	-11	34	12	0.43	7.58	8.64	0.047	M	
S052	13	14	44.6	-12	40	53	0.42	9.85	11.20	0.046	M	

TABLE 2—*Continued*

ID	$\alpha(\text{J2000})$			$\delta(\text{J2000})$			z_{est}	Σ_{obs}	Σ_{cor}	$E(B-V)$	Failed Criteria ^a	Notes
	h	m	s	°	'	"						
S053	13	15	29.7	-12	12	51	0.37	23.10	26.50	0.049	M	
S054	13	22	50.8	-12	24	10	0.54	7.57	8.58	0.045	M	
S055	13	24	03.2	-12	07	43	0.45	10.30	11.50	0.039	M	
S056	13	24	09.4	-12	26	02	0.34	14.70	16.70	0.046	G	
S057	13	26	01.9	-12	51	59	0.36	7.33	8.56	0.056	M	
S058	13	27	39.1	-12	01	04	0.29	34.90	39.20	0.042	z, G	
S059	13	29	11.4	-12	56	22	0.37	18.90	22.30	0.061	LSB	
S060	13	38	38.5	-11	59	16	0.42	12.40	15.80	0.089	M	
S061	13	48	03.3	-12	53	16	0.65	8.36	10.40	0.080	M	
S062	13	48	04.5	-12	21	04	0.35	9.07	12.10	0.103	E	
S063	13	48	59.7	-11	34	24	0.38	10.00	11.90	0.063	M	
S064	13	53	26.9	-12	02	57	0.81	8.69	10.60	0.070	M	
S065	14	03	22.4	-12	51	02	0.41	12.90	16.20	0.081	M	
S066	14	04	45.2	-11	34	37	0.53	7.27	8.97	0.076	M	
S067	14	04	46.2	-12	16	26	0.42	9.61	11.40	0.062	M	$z_{K_{eck}}=0.38$
S068	14	05	49.5	-11	49	26	0.35	21.40	24.90	0.056	G	
S069	14	06	09.1	-12	07	18	0.35	26.50	31.80	0.066	G	
S070	14	08	50.3	-12	18	12	0.55	14.70	17.60	0.065	M	
S071	14	09	57.9	-11	47	33	0.60	7.72	9.19	0.063	M	
S072	14	11	02.1	-12	37	17	0.32	18.70	22.60	0.069	LSB, G	
S073	14	11	34.8	-12	19	18	>0.85	9.17	10.90	0.064	M	
S074	14	11	48.8	-12	01	07	0.38	13.40	15.80	0.060	M	
S075	14	11	50.4	-12	02	26	0.29	16.30	19.30	0.061	z	
S076	14	13	28.7	-12	36	06	0.43	17.00	20.60	0.068	M	
S077	14	16	21.7	-11	56	06	0.48	7.76	9.29	0.065	M	
S078	14	31	49.4	-11	48	55	0.37	9.48	12.90	0.111	E	
S079	14	31	54.4	-11	51	21	0.32	12.20	16.60	0.111	E, M	
S080	14	37	11.2	-12	25	30	0.59	7.85	9.74	0.078	M	
S081	14	40	11.1	-12	23	41	0.28	29.80	36.60	0.073	G	
S082	14	40	22.3	-11	45	15	0.30	23.40	28.60	0.072	G	
S083	14	47	07.0	-11	36	54	0.43	14.00	17.50	0.080	M	
S084	14	47	38.0	-11	48	56	0.52	9.68	12.20	0.084	M	
S085	14	49	45.8	-12	13	56	0.73	7.66	9.54	0.080	M	
S086	14	49	46.9	-12	33	27	0.35	17.10	21.30	0.081	M	
S087	14	50	01.3	-12	38	55	0.29	16.80	21.10	0.083	z, M	
S088	14	51	13.9	-12	39	19	0.28	7.33	9.20	0.082	z	
S089	14	51	46.0	-12	20	39	0.26	6.61	8.40	0.087	z, S	
S090	14	52	45.5	-11	40	30	0.70	7.93	9.87	0.079	M	
S091	14	54	36.9	-11	37	19	0.67	7.14	9.19	0.091	M	
S092	14	56	40.9	-12	47	10	0.40	12.20	14.80	0.069	M	
S093	14	56	42.5	-12	48	14	0.25	7.02	8.49	0.069	z	
S094	14	59	37.1	-12	48	01	0.36	13.60	17.10	0.083	M	
S095	14	59	50.8	-12	45	26	0.32	9.11	11.30	0.079	M	
S096	15	00	13.0	-12	45	46	0.42	15.80	19.70	0.078	M	
S097	15	03	15.1	-12	37	05	0.43	13.00	16.90	0.095	M	
S098	15	08	47.7	-12	54	26	0.57	17.10	22.30	0.097	M	
S099	15	09	41.5	-12	25	19	0.29	8.08	10.60	0.097	z	
S100	15	10	49.1	-12	53	42	0.32	15.50	20.60	0.102	E	
S101	15	11	12.3	-11	55	29	0.73	8.42	11.00	0.097	M	
S102	15	11	48.6	-12	53	00	0.41	15.50	20.80	0.106	E, M	
S103	15	13	52.6	-11	47	32	0.41	11.00	15.00	0.112	E	
S104	15	14	49.4	-11	52	54	0.31	9.07	12.50	0.117	E	

TABLE 2—*Continued*

ID	$\alpha(\text{J2000})$			$\delta(\text{J2000})$			z_{est}	Σ_{obs}	Σ_{cor}	$E(B-V)$	Failed Criteria ^a	Notes
	h	m	s	°	'	''						
S105	15	14	54.0	-12	14	25	0.34	9.04	12.50	0.117	E	
S106	15	15	39.6	-12	54	27	0.43	13.80	19.90	0.133	E	
S107	15	27	12.0	-12	20	40	0.78	9.52	15.00	0.164	E,M	
S108	15	29	35.1	-12	31	44	0.25	41.00	62.10	0.150	z,E	
S109	15	33	18.9	-12	53	09	0.32	13.60	19.60	0.131	E	
S110	15	34	17.8	-12	31	56	0.41	9.02	13.10	0.135	E	
S111	15	37	20.9	-12	29	43	0.34	17.70	26.10	0.142	E	
S112	15	38	17.3	-12	25	58	0.53	8.94	12.80	0.131	E	

Note. — (a) Automated criteria that the detection failed to satisfy. The following designations are used: E - extinction $E(B-V) \geq 0.10$; z - $z < 0.30$; LSB - identified as a low surface brightness galaxy; S - flagged as likely spurious; M - partially masked; G - identified as a galaxy because $m_T < 18.75$.

TABLE 3
DETECTION AND CLASSIFICATION RESULTS

Σ_{obs} (10^{-3} csa)	z_{est}	Fraction Detected	Statistical Cluster Fraction
6.08	0.52	0.82	0.26
6.08	0.52	0.73	0.27
6.19	0.66	0.77	0.23
6.35	0.66	0.81	0.33
6.67	0.39	0.78	0.43
7.36	0.52	0.93	0.55
7.62	0.76	0.92	0.56
8.16	0.80	0.93	0.56
8.79	0.47	0.98	0.72
9.61	0.43	0.99	0.76
10.67	0.41	1.00	0.71
13.57	0.67	1.00	0.77